THE RELATIVE INFLUENCE OF QUARTZ AND MICA ON CRUSTAL SEISMIC ANISOTROPY

by

DUSTIN EVANS WARD

B.S., University of Texas, 2008

A thesis submitted to the

faculty of the Graduate School of the

University of Colorado in partial fulfillment

of the requirement for the degree

Master of Science

Department of Geological Sciences

2010

This thesis entitled:
The Relative Influence of Quartz and Mica on Crustal Seismic Anisotropy
written by Dustin Evans Ward
has been approved for the Department of Geological Sciences

Kevin Mahan

Anne Sheehan

Roy Geiss

December 1, 2010

The final copy of this thesis has been examined by the signatories, and we find that both the content and the form meet acceptable presentation standards of scholarly work in the above mentioned discipline.

The Relative Influence of Quartz and Mica on Crustal Seismic Anisotropy

Thesis directed by Assistant Professor Kevin H. Mahan

Seismic anisotropy is becoming an important observation when characterizing deformation in the middle and lower continental crust. Key contributors to this phenomenon (under mid-crustal conditions) include mineralogy and the degree of alignment among anisotropic phases. Micas are the most anisotropic phases in continental crust, and until recently, little consideration was given to the contribution of other crustal minerals. As quartz is one of the most common crustal minerals and its contribution to seismic anisotropy is poorly constrained, two mylonitic, micaceous quartzites were examined to investigate the influence of quartz microstructure on seismic anisotropy.

Electron backscatter diffraction (EBSD) was the primary method used for identifying sample mineralogy and textural characteristics. These data coupled with mineral elastic constants were used to calculate sample seismic attributes. Both quartzite samples exhibit calculated P-wave anisotropies between 6 and 8 percent. Additional calculations were performed varying the modal proportions of quartz and mica. These calculations suggest that the presence of aligned quartz decreases the overall anisotropy produced by aligned mica up to a threshold modal proportion (~70-80% quartz), and that quartz alters the symmetry of anisotropy, which may have important implications when interpreting crustal deformation.

One of the challenges to this study was acquiring quality EBSD data from phyllosilicates. These phases are historically difficult to characterize with EBSD. The underlying cause of this problem is under debate, however, prior studies suggest poor sample surface preparation and problems inherent to the phyllosilicate structure are to blame. Ion milling is a technique ideally suited for EBSD sample preparation as it offers the ability to smooth sample surface topography and remove damage induced by mechanical polishing. The viability of this method was tested for preparing polyphase, mica-bearing geological materials for EBSD analysis. Results show minimal improvement in phyllosilicate EBSD data from samples prepared with an ion mill. This appears to be due primarily to preferential etching along grain boundaries and weak Van der Waals bonds in the phyllosilicate structure.

ACKNOWLEDGEMENTS

This project was supported in part by a National Science Foundation grant to Kevin Mahan (EAR-0750035), a student research grant from the Geological Society of America, a student research grant from Hartmut Spetzler, and support from the Alliance for Graduate Education and the Professoriate (AGEP).

Without the support of my faculty advisor, Kevin Mahan, this project would not have been possible. I would like to express special thanks to him for his patience and continued support. I would also like to thank the faculty and staff of the University of Colorado's Geological Sciences department and Nanomaterial Characterization Facility.

Throughout this project I received technical assistance from several individuals and entities and would like to take this opportunity to acknowledge the following: My graduate student mentor Alexis Ault, Susan Swapp and the University of Wyoming's Microscopy Core Facility, David Mainprice for use of, and assistance with anisotropy careware, Scott Walck and South Bay Technologies, Inc. for generous use of the Ion Beam Sputter Deposition and Etching system (IBS/e), EDAX-TSL, Paul Boni for assistance with sample preparation, and Rick Almendinger for use of Stereonet for Macintosh.

This thesis was greatly improved by the helpful reviews of my committee members, Kevin Mahan, Anne Sheehan and Roy Giess.

Finally, I would like to thank my wife, April Moreno, and my parents, Michael and Grace Sauce, for their support and encouragement throughout the duration of this project.

CONTENTS

TABLES

Table

FIGURES

Figure

CHAPTER I - The Relative Influence of Quartz and Mica on Crustal Seismic Anisotropy

INTRODUCTION

Seismic anisotropy refers to the directional dependence of seismic wave velocities in certain materials. In crustal materials, seismic anisotropy is primarily a function of mineralogy, alignment of micro-cracks (Crampin, 1991), alignment of macroscopic fractures associated with regional tectonics (Mueller, 1991), and the degree of alignment among anisotropic phases (Mainprice and Nicolas, 1989 , Sayers, 1994). Under mid-crustal conditions micro-cracks and fractures are closed, and thus the primary contributors to seismic anisotropy are mineralogy and mineral alignment. Early anisotropy studies focus primarily on the mantle. These studies commonly interpret mantle dynamics beneath geologic areas of interest, e.g. subduction zones and other tectonically active regions (Behn et al., 2007, Becker et al., 2006). Typically, mantle studies assume deformationally aligned olivine is primarily responsible for observed anisotropy. Recently, it has become popular to utilize this phenomenon to interpret crustal deformation (Zandt et al., 2004, Moschetti et al., 2010). These studies use anisotropy to examine crustal heterogeneities (Mizuno et al., 2001), crustal stress fields (Boness and Zoback, 2006), and to interpret crustal deformation structures and kinematics (Zandt et al., 2004, Schulte-Pelkum et al., 2005). Studies investigating crustal deformation typically assume that deformationally aligned micas are responsible for crustal seismic anisotropy, however, relatively few studies explore the link between rock fabric, mineralogy and crustal seismic anisotropy (e.g. Lloyd et al., 2009, Tatham et al., 2007, Lloyd and Kendall, 2005, Rey et al., 1994, McDonough and Fountain, 1993, Ji et al., 1993, Burlini and Fountain, 1993, Kern and Wenk, 1990, Mainprice and Nicolas, 1989).

Micas exhibit the highest degree of seismic anisotropy among crustal minerals. Although many crustal anisotropy studies suggest these phases are the dominant contributor (Schulte-Pelkum et al., 2005, Meissner et al., 2006, Mahan, 2006), most crustal minerals exhibit some degree of seismic anisotropy and the influence of other anisotropic phases must be considered. Quartz, among the most common crustal minerals, displays a substantial anisotropic character

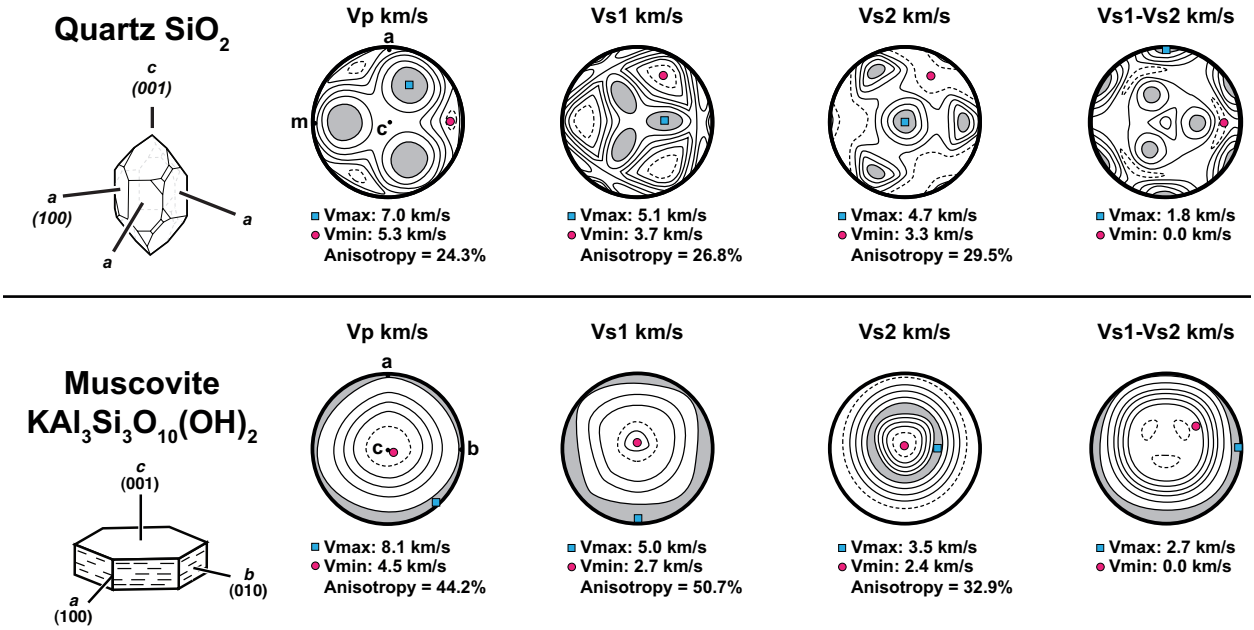

Figure 1.1. Pole figures showing single crystal anisotropy of quartz and muscovite. Modified after Ji et al., 2002.

(Figure 1.1). The interpreted role of this phase ranges from having no influence on bulk seismic anisotropy despite a strong alignment of quartz grains (Rey et al., 1994) to having an anisotropy that cancels with other phases (i.e. feldspars, Ji et al., 1993), to having a significant influence on seismic anisotropy (McDonough and Fountain, 1993). To better understand the influence of this phase relative to aligned mica, lithologies rich in both quartz and mica exhibiting deformation fabrics and metamorphic conditions expected under mid-crustal conditions were examined. Both the Mullen Creek-Nash Fork shear zone (the Cheyenne belt) in southeastern Wyoming, and the Idaho Springs-Ralston shear zone in central Colorado, offer exposures of mylonitic, micaceous, quartzites deformed under greenschist and amphibolite facies conditions, respectively. These rocks possess a strong shear-related foliation defined by aligned mica, and a stretching/mineral lineation defined by elongate quartz grains; a combination that allows for examination of the relative roles of quartz and mica in producing or retarding seismic anisotropy. Samples from both locations are examined in this study.

The Cheyenne belt (Figure 1.2) is interpreted as the primary suture between the Archean

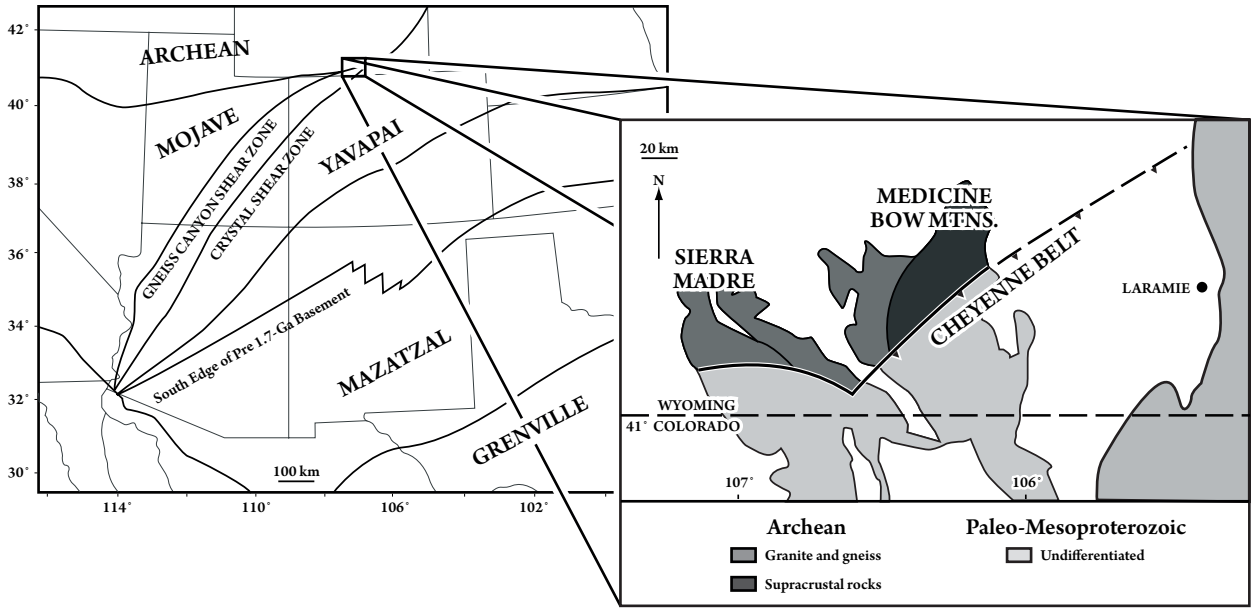

Figure 1.2. Cheyenne Belt regional setting, after Karlstrom and Humphreys, 1998 and Duebendorfer et al., 2006.

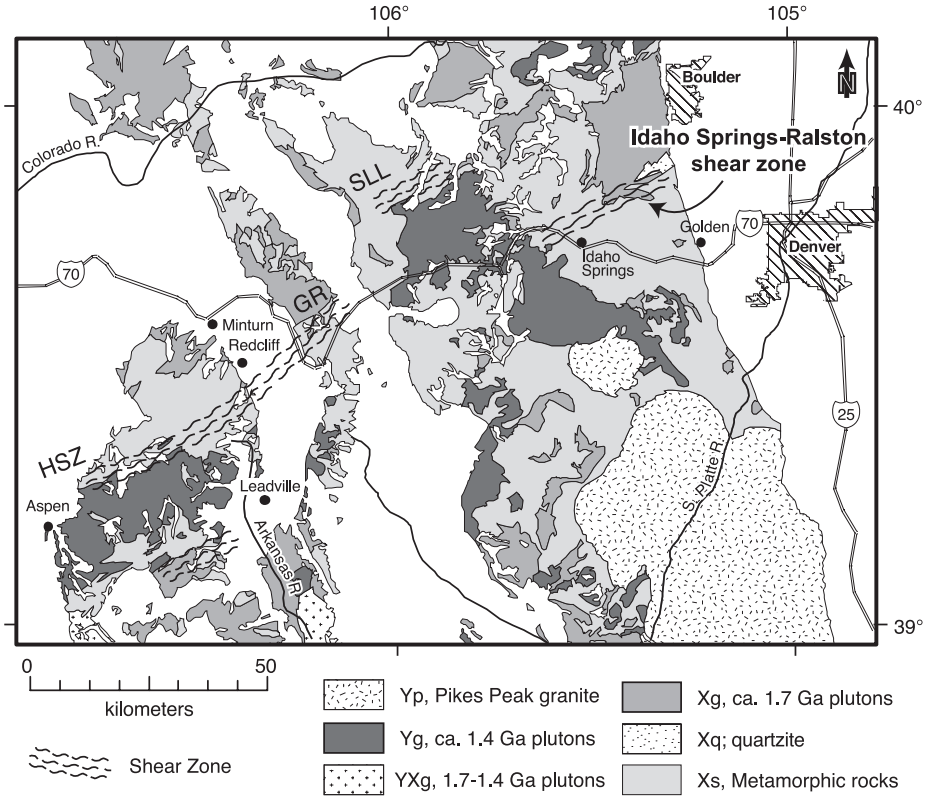

Figure 1.3. Simplified Precambrian geologic map of central Colorado showing Proterozoic shear zones. (adapted from Tweto and Sims,1963).

Wyoming craton and Proterozoic arc terranes of the southwestern U.S. (e.g. Karlstrom and Houston, 1984, Chamberlain et al., 2003). Metamorphic conditions in the area are consistent with upper greenschist to lower amphibolite facies (Duebendorfer, 1988). Quartzite mylonites from the Cheyenne belt exhibit a variety of quartz deformation mechanisms and a strong foliation defined by aligned micas.

Similarly, the Idaho Springs-Ralston shear zone (Figure 1.3) offers excellent exposures of variably mylonitized lithologies. This shear zone exhibits a rich and complex history of activation and reactivation associated with continental assembly and intracontinental deformation of the southwestern United States (Wessel and Ridley, 2009). The most recent ductile fabric appears to be a narrow band of upper greenschist to amphibolite facies ultramylonite, which cross-cuts the Coal Creek quartzite northwest of Golden, Colorado (Shaw et al., 2002).

Quartzite mylonites from both locations were examined to investigate the influence of deformed quartz, in the presence of aligned mica, on crustal seismic anisotropy. Standard optical petrologic characterization, automated modal mineralogical analysis (QEMScan®), and textural analysis via electron backscatter diffraction (EBSD) were employed to fully characterize metamorphic conditions and deformation mechanisms in each sample. EBSD data, combined with quartz and muscovite elastic constants, were then used to calculate seismic properties over a range of quartz to muscovite ratios.

GEOLOGIC SETTING

Cheyenne Belt.

The Cheyenne belt is interpreted as the Proterozoic suture between the Archean Wyoming craton and Proterozoic arc terranes of the southwestern United States (Figure 1.2). Exposed in the Medicine Bow and Sierra Madre Mountains of southeastern Wyoming, the Cheyenne belt consists of a series of northeast-striking, steeply dipping shear zones separated by discrete, tectonized blocks of Archean and Paleoproterozoic age.

North of the Cheyenne belt, Archean basement rocks (dominantly granite and gneiss) are overlain by Late Archean/ Early Proterozoic quartzite, phyllite, metadolomite and metavolcanics collectively known as the Archean Phantom Lake metamorphic suite (Karlstrom and Heizler, 1979) and the Proterozoic Snowy Pass Supergroup (Figures 1.4 and 1.5). Within the Snowy Pass Supergroup, and listed in stratigraphic succession, are the Deep Lake Group, Lower Libby Creek Group and the Upper Libby Creek Group. These rocks record transgressive deposition thru time from primarily fluvial deposits in the Deep Lake Group, to shallow marine in the Lower Libby Creek Group, to deep marine in the Upper Libby Creek Group (Karlstrom et al., 1983). This evidence coupled with paleocurrent observations led to the interpretation of a paleo-continental margin oriented approximately northeast and dipping to the southwest (Karlstrom et al., 1983, 1984). Today these rocks dip steeply (from ~57˚ to near vertical, Houston and Parker, 1963) to the south and are cross-cut by a series of steeply dipping (from ~60˚ to near vertical, Houston, 1993), northeast trending shear zones which are collectively the Cheyenne belt. South of the Cheyenne belt are Proterozoic, eugeoclinal rocks, which include metavolcanics, metagraywacke, metapelite, amphibolite, hornblende gneiss, calc-schist, and marble (Houston et al., 1989)

Within the dominantly siliciclastic Lower Libby Creek Group lies the Medicine Peak quartzite (Figure 1.5). This ~1700 meter unit is folded within the French Creek syncline with its southern limb terminating against the northern mylonite zone of the Cheyenne belt. This relationship along with mineralogical similarities suggests the Medicine Peak quartzite is the protolith of the

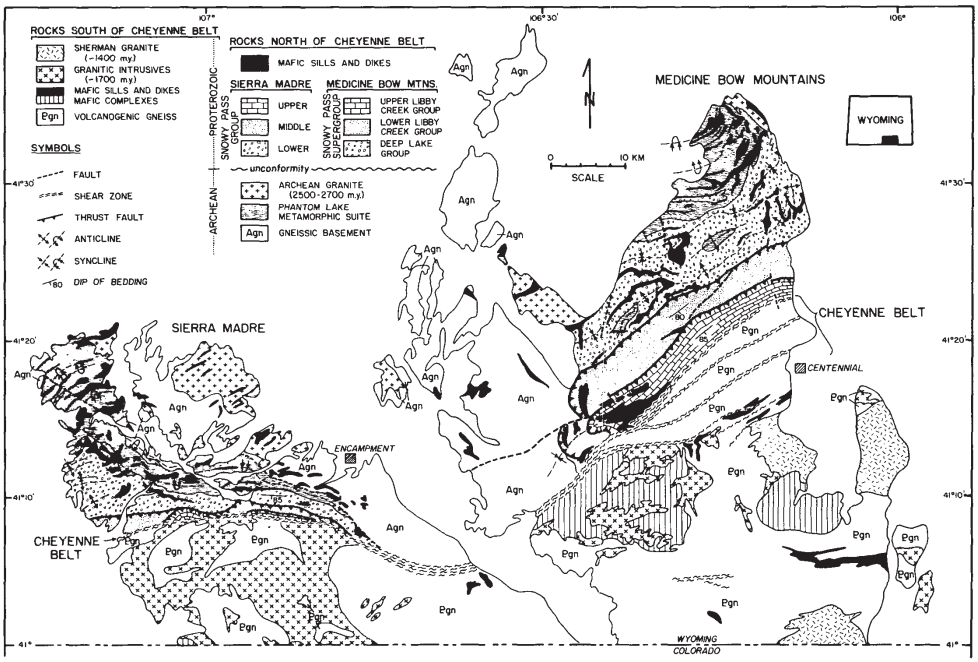

Figure 1.4. Simplified Precambrian geologic map of the Medicine Bow Mountains and Sierra Madre, Southeastern Wyoming. Karlstrom et al., 1983.

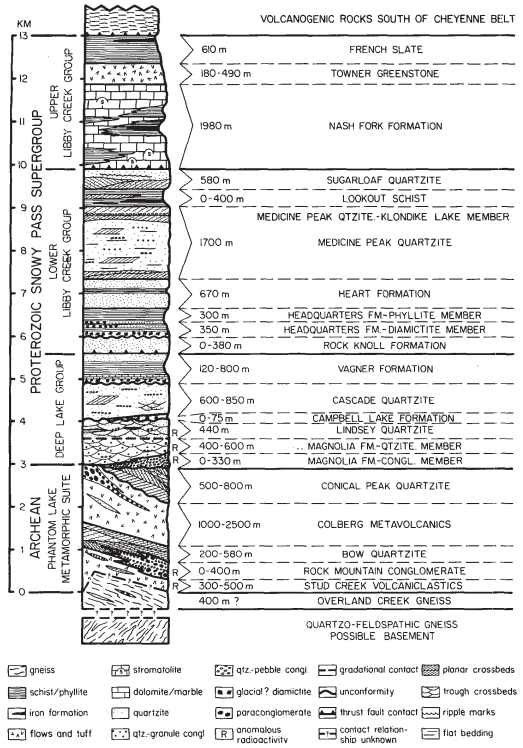

Figure 1.5. Stratigraphic column of Metasedimentary rocks of the Medicine Bow Mountains. Karlstrom et al., 1983.

mylonitic quartzite unit (Xmq), the primary lithology in this study.

Seismic reflection data from the southern margin of the Wyoming craton reveal a 30-50 km wide zone of intersecting north- and south-dipping reflectors (Morozova et al., 2002). Two prominent south-dipping reflectors have been associated with the Cheyenne belt. These features are intersected at depth by north-dipping reflectors that can be traced to the Farwell-Lester Mountain zone within the Colorado Province. The resulting interpretation is that the Cheyenne belt consists of a steep zigzagging, inter-wedging contact between the Archean Wyoming craton and the Proterozoic Green Mountain block.

Ball and Farmer (1991) report that Proterozoic miogeoclinal sedimentary rocks exposed north of the Cheyenne belt have Nd model ages ranging from 2.6 to 3.0 Ga and εNd values ranging from -7.3 to -11.9. The Archean Nd model ages and low εNd values require that metasedimentary rocks north of the Cheyenne belt (the upper and lower Libby Creek Groups) be derived solely from Archean sources. This study also confirms the lack of Archean sources in Proterozoic crust exposed south of the Cheyenne belt as evidenced by εNd values ranging from -1.5 to 4.0 and Nd model ages of 1.8 to 2.1 Ga.

Premo and Van Schmus (1989) constrain initial rifting and development of a passive margin to ca. 2.1-2.0 Ga from U-Pb zircon ages of metagabbro dikes in the Sierra Madre. Deformation along the Cheyenne belt began approximately 1.78 Ga and continued through 1.76 Ga based on U-Pb zircon ages of pre- and syn-deformational plutonic emplacement in both the Sierra Madre and Medicine Bow Mountains (Premo and Van Schmus, 1989, Loucks et al., 1988). Several authors report evidence of reactivation in the Cheyenne belt, specifically at ~1.65-1.63 Ga (Jones et al., 2010), and ~1.60-1.59 Ga (Strickland, 2004, Duebendorfer et al., 2006).

Sample 092108A1, of this study, was collected along the northern mylonite zone (the Mullen Creek-Nash Fork shear zone) of the Cheyenne belt. This sample is of the mylonitic quartzite (Xmq) as described by Houston and Karlstrom (1992), located just south of, and juxtaposed against the Mullen Creek-Nash Fork shear zone (Figure 1.6). The average orientation of the shear foliation

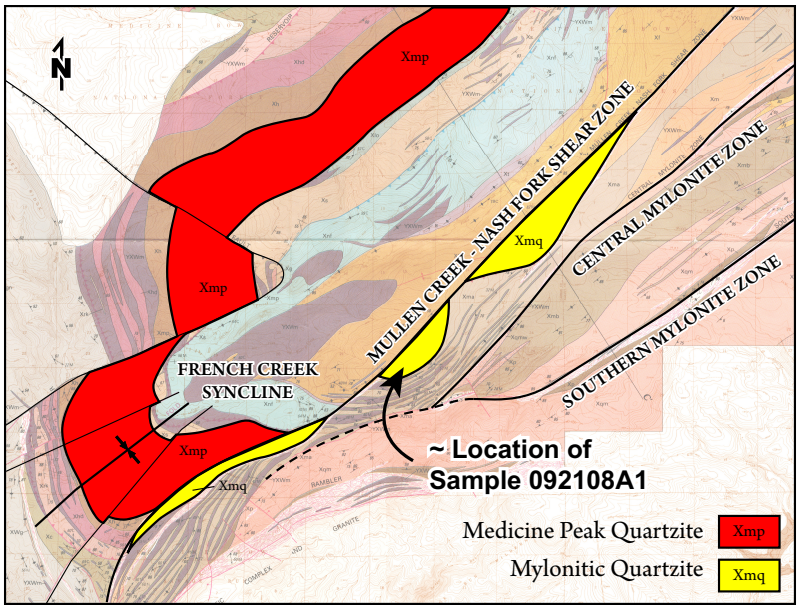

Figure 1.6. Simplified geologic map of the Cheyenne belt as exposed in the Medicine Bow Mountains, showing ~ location of sample 092108A1. Modified after Houston and Karlstrom, 1992.

plane at this location, as reported by Houston and Karlstrom (1992), is ~222, 86. However, due to poor outcrop exposure at this location, several mylonitic to ultramylonitic quartzite samples were collected here that do not match this orientation. These samples are similar in description to those originally described by Houston and Karlstrom (1992) and they share general orientational agreement (111, 29), suggesting collected samples are of a portion of the Xmq, mylonitic quartzite unit that has slumped or rotated after the development of ductile fabrics.

Idaho Springs-Ralston shear zone.

The Idaho Springs-Ralston shear zone (IR-SZ) (Figure 1.2) is a northeast-southwest trending shear zone located in central Colorado. The shear zone cuts the Boulder creek batholith (1721 ± 15 Ma, Premo and Fanning, 2000) to the northeast and terminates to the southwest within the Mt. Evans batholith (1442 ± 2 Ma, Aleinikoff et al., 1993) where shear zone fabrics dissipate into magmatic and solid state fabrics. This relationship suggests that at least some component of shearing within the IR-SZ was active during emplacement of the batholith. The complex history

of this shear zone is further evidenced by preserved tectonic fabrics that record an early high temperature, low-angle fabric (S1) overprinted by folding (S2, F2), and subsequent greenschist facies mylonitization (S3 southeast side down) and ultramylonitization (S4 southeast side up) (Shaw e al., 2002, McCoy et al., 2005).

The Coal Creek Quartzite is cut by the IR-SZ in its northeastern reaches. This unit marks the folded structure that surrounds the IR-SZ and in addition to showing preserved sedimentary structures, records multiple phases of deformation in the area.

M08-23A is a mylonitized Coal Creek Quartzite sample collected in the core of the IR-SZ, northwest of Golden, CO. Primary lithologies in this area include orthogneiss, quartzite and schist. Both the orthogneiss and the quartzite are locally mylonitized and folded. Complex, isoclinal fold structures as well as evidence of multiple fabric generations are best preserved within the schist. The average orientation of the main shear fabric is ~065, 85 (Figure 1.8A) and shear sense indicators record both a strike-slip and dip-slip component of primarily sinistral, southeast side up sense of shear. A pi-diagram (Figure 1.8B) generated from orientational data in the schists reveals a fold axis orientation of 20 > 067, suggesting a genetic relationship to the main shear foliation.

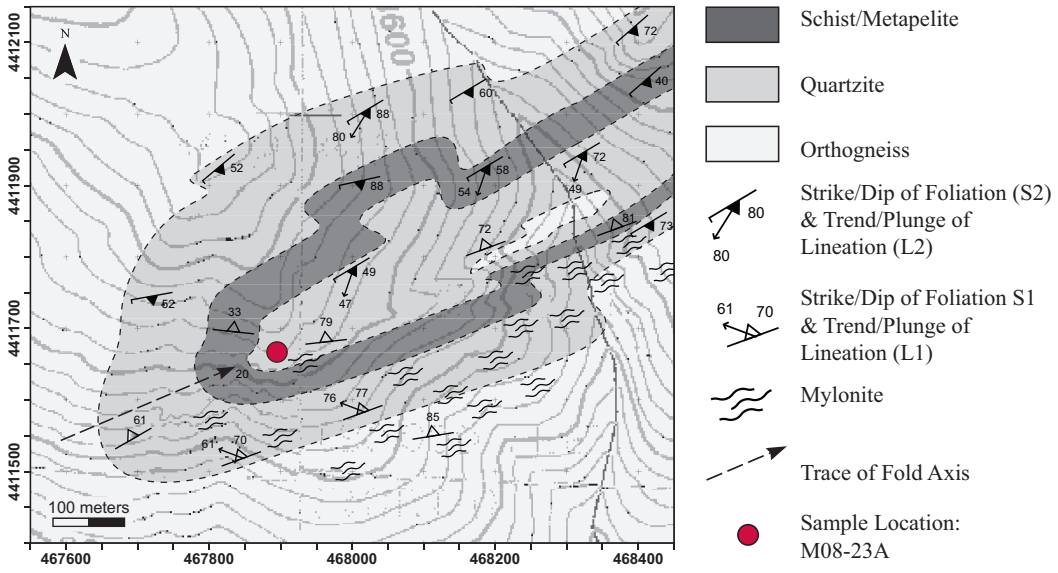

Figure 1.7. Simplified geologic map of the Coal Creek Quartzite sample location within the Idaho Springs-Ralston Shear Zone.

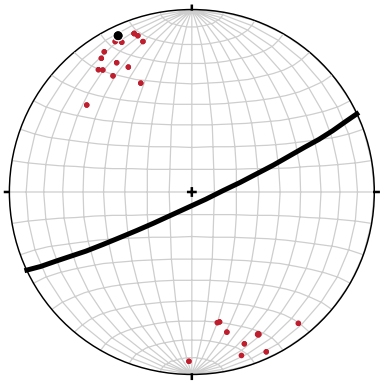

A) Poles to mylonite foliation plane (gray circles) with mean pole (black circle), and corresponding mean great circle (black line).

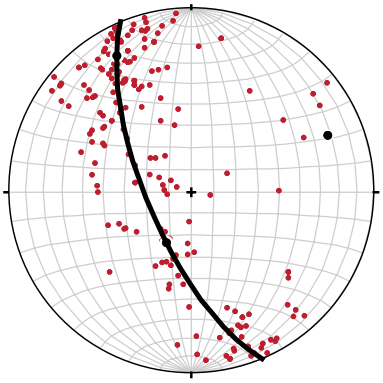

B) Pi diagram of S0, S1 and S2 foliations measured in schist/metapelite.

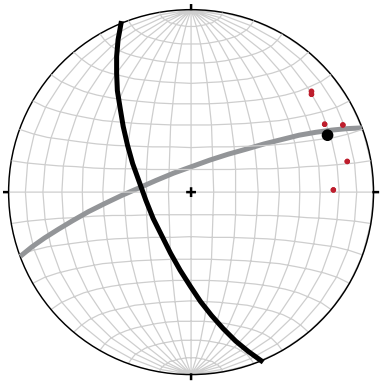

C) F3 fold profile plane (black line) with corresponding map scale fold axis (black circle), individual F3 hinge measurements (gray circles) and mean S3 plane (gray line).

Figure 1.8. Stereographic projection of structural data from the Idaho Springs-Ralston Shear Zone.

SAMPLE DESCRIPTION

All samples were collected and oriented in the field. Standard geological thin sections were prepared via traditional protocol. Each section was cut strategically to view a kinematic (x-z) plane, i.e., a plane containing both the maximum extension (x) and maximum shortening (z) directions as determined by foliation and lineation orientations. Petrographic examination of each sample was performed to characterize mineralogy, microfabrics, and active deformation mechanisms, and to approximate metamorphic conditions based on mineralogy and texture. In addition to petrographic analysis, each sample underwent quantitative automated mineralogical analysis, a scanning electron microscopy based energy dispersive analytical technique proprietary to FEI as QEMSCAN®.

Sample 092108A1 (Figure 1.9) is a mylonitic quartzite (Xmq) from the Cheyenne Belt, southeastern Wyoming. Grain size is very fine (~10-100μm) and hand samples appear gray to bluish-gray. Mineralogy consists of quartz, muscovite and kyanite as well as minor accessories (opaque oxides, zircon, monazite). A strong foliation defined by aligned muscovite is visible at hand sample scale and oriented approximately 111, 29. A mineral lineation, defined by alignment of quartz grains, is also visible at hand sample scale and is oriented approximately 11 > 144. Primary sedimentary structures are absent. A thin section of this sample reveals a composite s-c fabric (Figure 1.10) defined by aligned muscovite and a shape preferred orientation of quartz grains. This fabric suggests dextral shear sense and is consistent with a south side up interpretation of the northern shear zone of the Cheyenne belt. Quartz grains exhibit grain boundaries consistent with sub-grain rotation recrystallization and grain boundary migration (Figure 1.11) and are consistent with regime 3 deformation after Hirth and Tullis (1992). All quartz grains show undulatory extinction and many fully encapsulate muscovite grains (Figure 1.11) indicating high grain boundary mobility during recrystallization perhaps enhanced by the presence of fluids.

Sample M08-23A (Figure 1.12) is a mylonitized sample of the Coal Creek quartzite from the IR-SZ, central Colorado. Grain size is very fine (~30-100μm) and samples appear white to

light gray. Mineralogy consists of quartz, muscovite, sillimanite and minor accessories. Samples exhibit a strong foliation, defined by aligned muscovite, and oriented approximately 263, 67. A mineral lineation is observable at hand sample scale and is defined by alignment of quartz and mica grains. Mineral lineation is oriented approximately 63 > 290. Primary sedimentary structures are absent in this sample although they are well preserved in lower strain domains. A thin section of this sample reveals a composite s-c fabric (Figure 1.13) defined by aligned muscovite and a shape preferred orientation of quartz grains. This fabric suggests dextral shear sense and is consistent with a south-east side up interpretation of the IR-SZ. Quartz grains exhibit undulatory extinction and grain boundaries consistent with grain boundary migration and sub-grain rotation recrystallization. Many grains fully encapsulate muscovite and sillimanite grains (Figure 1.14) indicating high grain boundary mobility during recrystallization. Quartz microstructures present in this sample are similar to regime 2 microstructures described by Hirth and Tullis (1992).

Automated modal mineralogical analysis (QEMSCAN®) was performed at the Colorado School of Mines Advanced Mineralogy Research Center. The QEMSCAN® system consists of a Zeiss EV050 scanning electron microscope with four Bruker silicon-drift energy dispersive X-ray detectors, a four-quadrant solid-state backscatter electron detector, and a secondary electron detector. Standard operating conditions include an accelerating voltage of 25 kV, a specimen current of 5 nA, and a working distance of ~ 24 mm (Hoal et al., 2009). The primary purpose of this analysis is to provide an independent measure of sample modal mineralogy to compare our electron backscatter diffraction data against.

Data were collected using this method from representative areas of both quartzite samples. Results can be seen in figures 1.15 and 1.16 and are as follows: 092108A1 (Figure 1.15) consists of 95% quartz, 2.4% muscovite, 2.1% kyanite, and 0.5% accessories. M08-23A (Figure 1.16) consists of 94.5% quartz, 2.8% muscovite, 2.3% sillimanite, and 0.5% accessories.

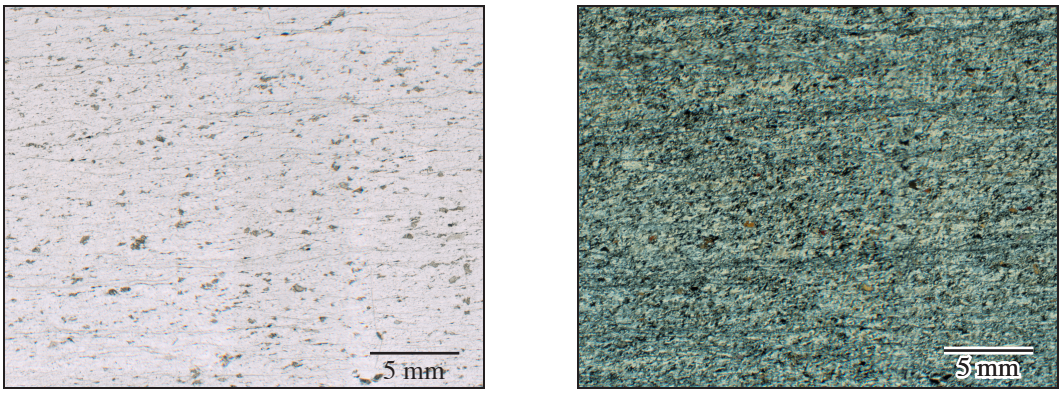

Figure 1.9. Plane polarized light (A) and cross-polarized light (B) photomicrographs of mylonitic quartzite sample 092108A1, XZ section.

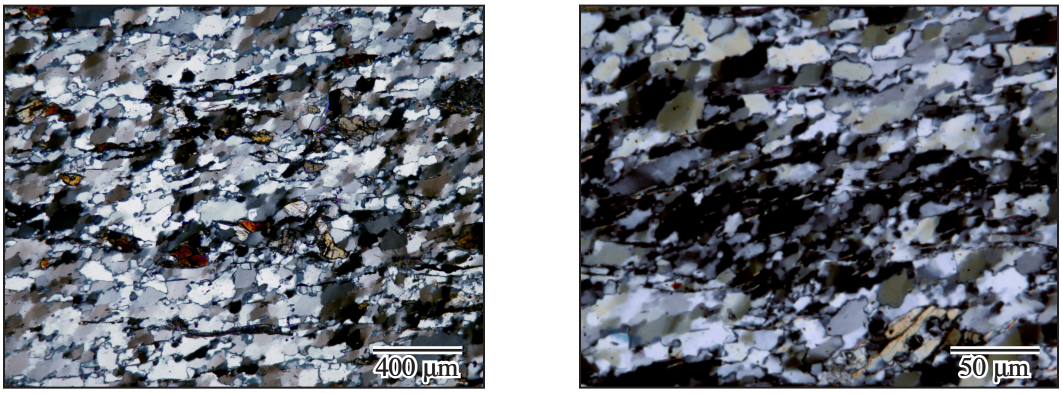

Figure 1.10. Cross polarized light photomicrographs of sample 092108A1 showing (A) composite, "C-S" fabric and (B) sigma clast-like structures, suggesting a dextral shear sense.

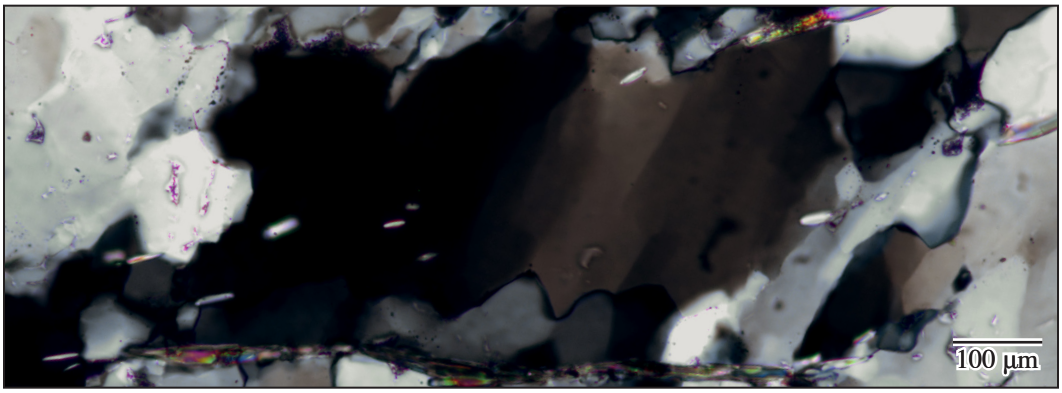

Figure 1.11. Cross polarized light photomicrograph of sample 092108A1 showing bulging quartz grain boundaries with undulatory extinction and fully encapsulated muscovite grains.

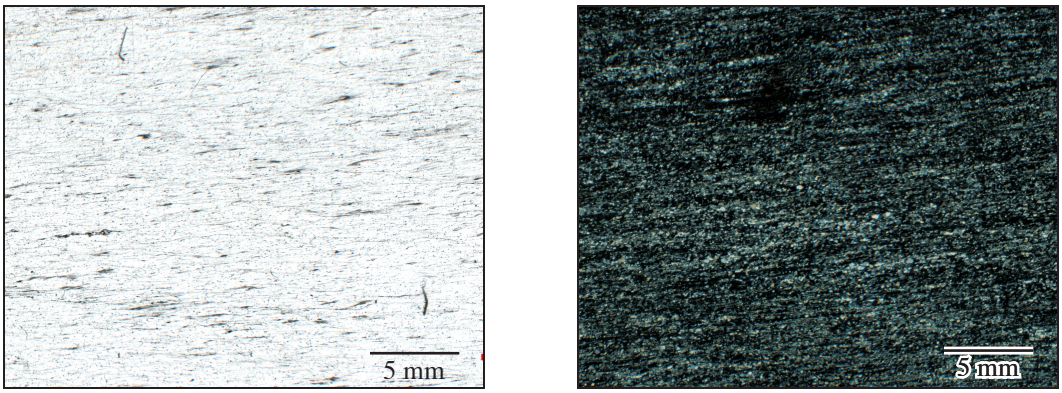

Figure 1.12. Plane polarized light (A) and cross-polarized light (B) photomicrographs of mylonitic quartzite sample M08-23A, XZ section.

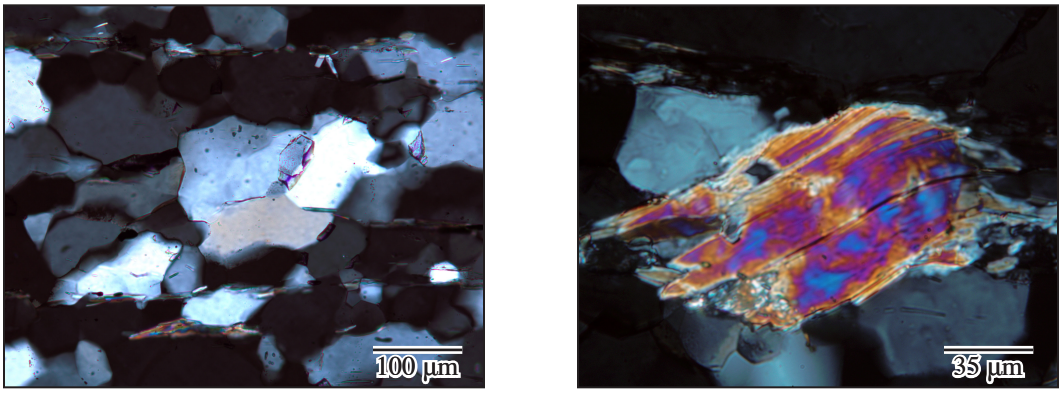

Figure 1.13. Cross polarized light photomicrographs of sample M08-23A showing (A) composite "C-S" fabric and (B) a muscovite sigma clast, suggesting dextral shear sense.

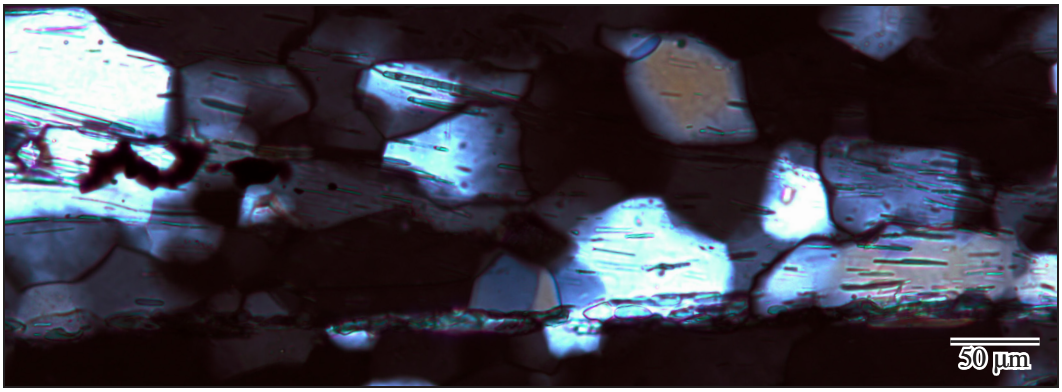

Figure 1.14. Cross polarized light photomicrograph of sample M08-23A quartz grains with fully encapsulated muscovite and sillimanite grains.

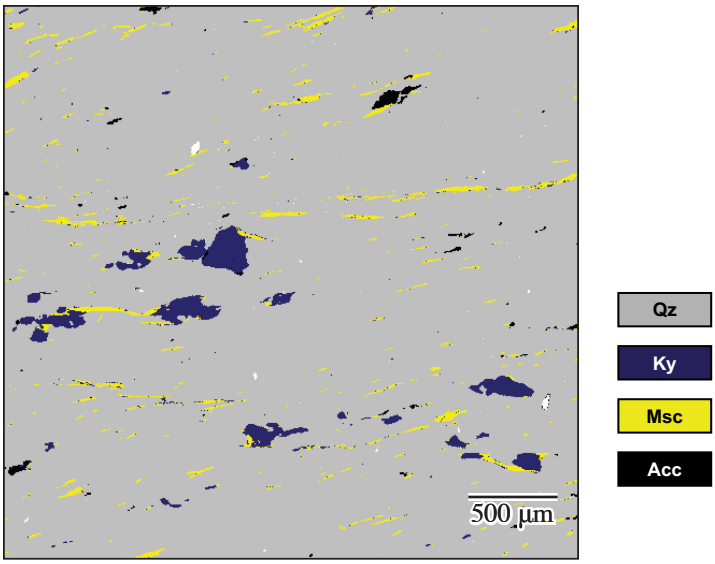

Figure 1.15. QEMSCAN map of a representative section of sample 092108A1. Phases present in modal proportion are: 95% quartz (gray), 2.4% muscovite (yellow), 2.1% kyanite (blue), 0.5% accessories (black).

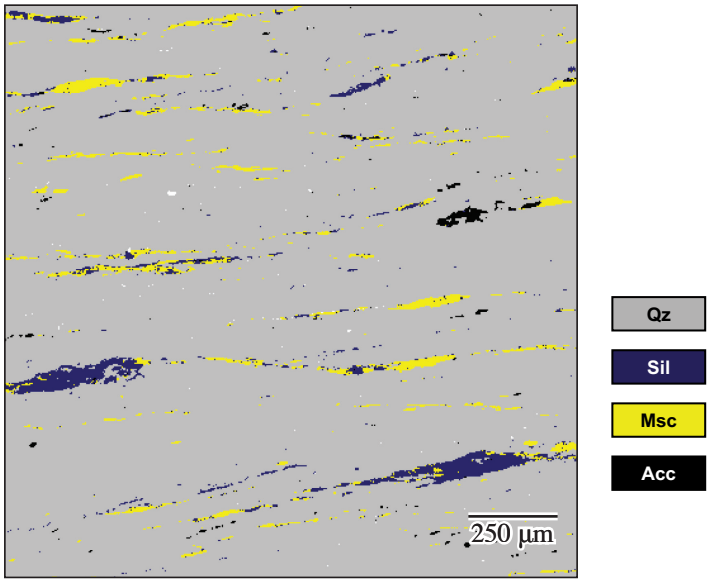

Figure 1.16. QEMSCAN map of sample M08-23A. Phases present in modal proportion are: 94.4% quartz (gray), 2.8% muscovite (yellow), 2.3% sillimanite (blue), 0.5% accessories (black).

QUANTITATIVE ANALYSIS

The primary methods for determining sample seismic anisotropy include direct measurement and calculation from mineral modal proportions, elastic constants and CPO data. The former is a bulk measurement and does not allow one to isolate the influence of individual phases. The latter requires that the user accurately interpret sample texture to properly characterize velocity anisotropy. Earlier studies commonly employ this technique using CPO data acquired manually with a Universal-stage (e.g. Mainprice and Nicolas, 1989, Burlini and Fountain, 1993, McDonough and Fountain, 1993), although this method cannot provide complete orientation data for all phases. Electron backscatter diffraction is an automated technique that allows the user to identify phases and their complete 3 dimensional orientation. Data collected via this method were used to calculate seismic velocity anisotropy over a range of quartz to muscovite ratios in samples deformed under upper greenschist to lower amphibolite facies.

Electron backscatter diffraction (EBSD) has become a popular tool in materials and geological laboratories. The increasing availability of scanning electron microscopes (SEM) coupled with the ability to quickly identify phases and phase orientations have no doubt attributed to the increasing use of this method. The application of EBSD to geological sciences is a developing technique that has lead to advances in microstructural analysis over roughly the past two decades.

The basic principle behind EBSD is the generation and characterization of Kikuchi bands, also known as electron backscatter diffraction patterns (EBSPs - figure 1.17). EBSPs are generated by backscatter diffraction of high-energy electrons, and are imaged on a phosphor screen (Figure 1.18). Each pattern is then indexed against a database of known and theoretical values of interplanar angles and interplanar spacings (a look up table) used to identify phases within a sample. This requires that the user has some prior knowledge of the sample or that EBSD is used in conjunction with a chemical identifier such as energy dispersive spectroscopy (EDS) or wavelength dispersive spectroscopy (WDS).

The spatial resolution of electron microscopy is primarily a function of the excitation

volume within a sample and less a function of spot size/beam diameter. Excitation volume refers to the fraction of a sample within which primary electrons are interacting and are back diffracted without additional scatter, and is a function of beam voltage and sample density. Typical spatial resolution for most materials is of the submicron scale (e.g. 0.05 μm for copper at 20 kV, 3-5 nA beam current, tungsten filament) and can be improved by reducing beam current, however this will reduce beam brightness and thus pattern intensity.

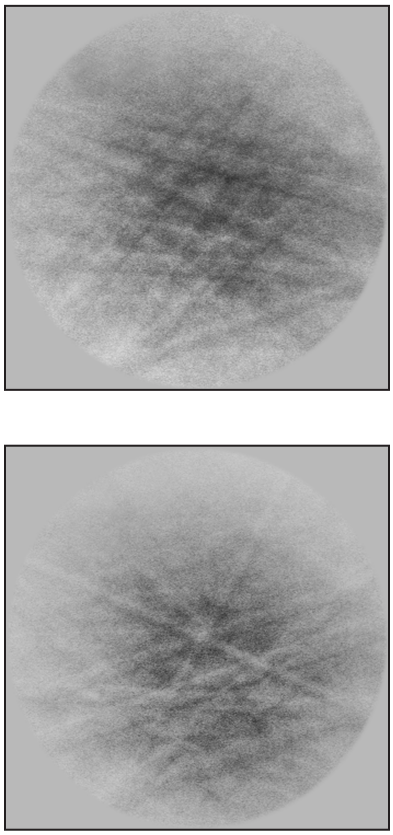

Figure 1.17. Electron backscatter diffraction patterns from quartz. Generated from the mylonitic quartzite (Xmq), Cheyenne belt.

Although EBSD data can be collected from most naturally occurring minerals, certain limitations exist when applying this method to Earth sciences. For instance, specimens examined using EBSD should be conductive, stable under vacuum, and should not break down under the electron beam. Due to spatial resolution issues, EBSD is limited to samples with grain sizes greater than several tens of nanometers in diameter. Sample surfaces should be relatively smooth and void of any topography. Misindexing and non-indexing are extremely prevalent in geological materials and occur predominantly as a result of low symmetry and poor signal in the EBSP. Many of the limitations of this method to geological materials can be addressed by careful sample surface preparation, adjustment of EBSD working conditions and the use of a thin (up to a few nanometers) layer of conductive material applied to the sample surface to dissipate charge (e.g. carbon, gold-palladium, etc…).

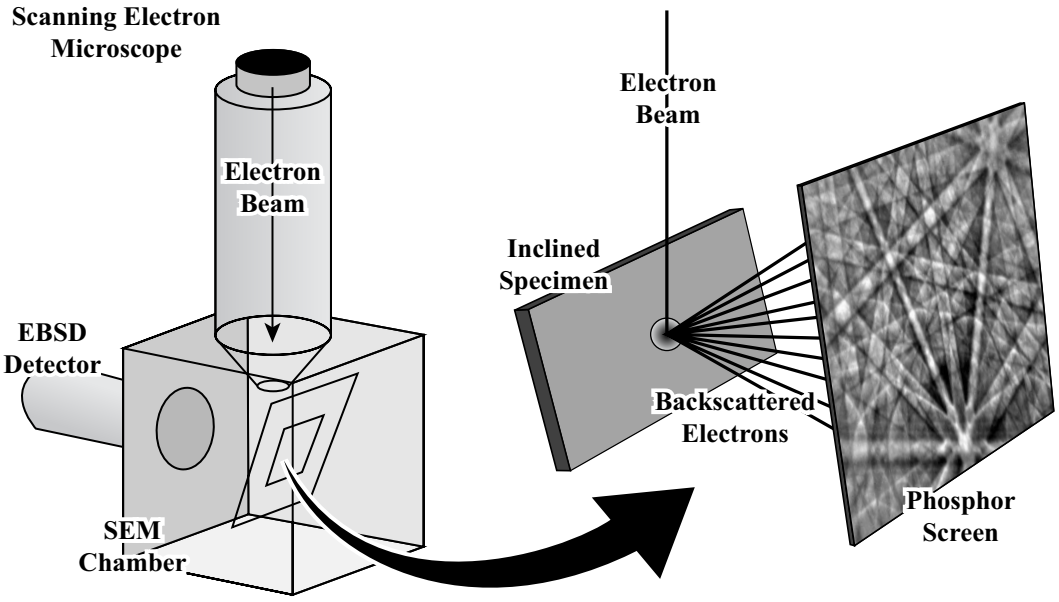

Figure 1.18. Highly simplified schematic of a typical SEM-EBSD system. For illustration purposes, the specimen and screen on the right are rotated 180˚.

Each sample underwent a minimum of 1 hour, maximum of 2 hours of chemical/mechanical polishing using Buehler's MasterMet 2 non-crystallizing colloidal silica polishing suspension and Chemomet I polishing cloth. Samples were mounted in a weighted brass sample holder during hand polishing to ensure as consistent a finish as possible. A thin (<10nm) layer of carbon was applied to each sample to dissipate charge buildup during data collection.

EBSD data were collected on sample 092108A1 using an FEI Nova 600i scanning electron microscope with an EDAX-TSL EBSD attachment and integrated EDS. This system is housed at the EDAX-TSL western office in Draper, Utah. Phase and orientation data were mapped over a 2.5mm^2 area with a 5μm step size, for a total of ~340,000 data points. Specific operating conditions include a 20 kV accelerating voltage, 4.5nA beam current, 14mm working distance, and the sample was tilted to 70˚. The index rate for this dataset is greater than 90%. This unusually high index rate is due in part to chemical data provided by simultaneous EDS analysis. Figure 1.19A is an image quality map, i.e. a map of grayscale pixels that correspond to the quality of the EBSP for each datapoint. This map is overlain by color coded mineralogy in the following proportions: 93.5%

quartz, 2.3% muscovite and 2% kyanite, which is in general agreement with QEMSCAN results.

Textural data are represented in stereographic projection in figure 1.20. The quartz c-axis pole figure reveals a type-I cross girdle (Figure 1.21) after Lister, 1977, and is consistent with plane strain and progressive simple shear (Lister, 1977, Schmid and Casey, 1986). This pattern can be used to estimate temperature conditions during deformation via a method described by Kruhl, 1996, that measures the angle between quartz c-axis girdles. Results from this method suggest deformation temperatures at ~415 ±50˚C (Figure 1.21) which is consistent with the presence of kyanite, and the combination of subgrain rotation and grain boundary migration deformation fabrics observed in the sample. This estimate is also in general agreement with upper greenschist facies temperature constraints in the Cheyenne belt from Duebendorfer, 1988. Muscovite data are also presented in Figure 1.20 and are consistent with a composite fabric, defined by foliated muscovite, as observed in this sample.

EBSD data were collected on sample M08-23A using a JEOL (JSM-5800LV) scanning electron microscope with HKL EBSD system. This system is housed at the University of Wyoming's

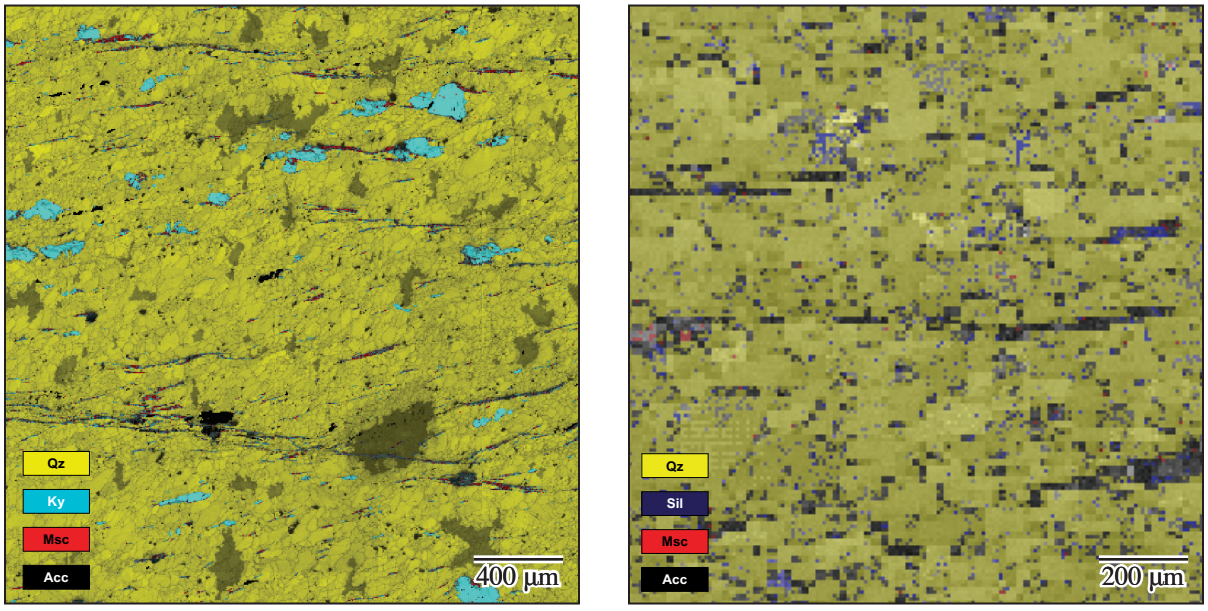

Figure 1.19. Grayscale image quality map, overlain by color-coded mineralogy of samples A) 092108A1 and B) M08-23A, generated via EBSD.

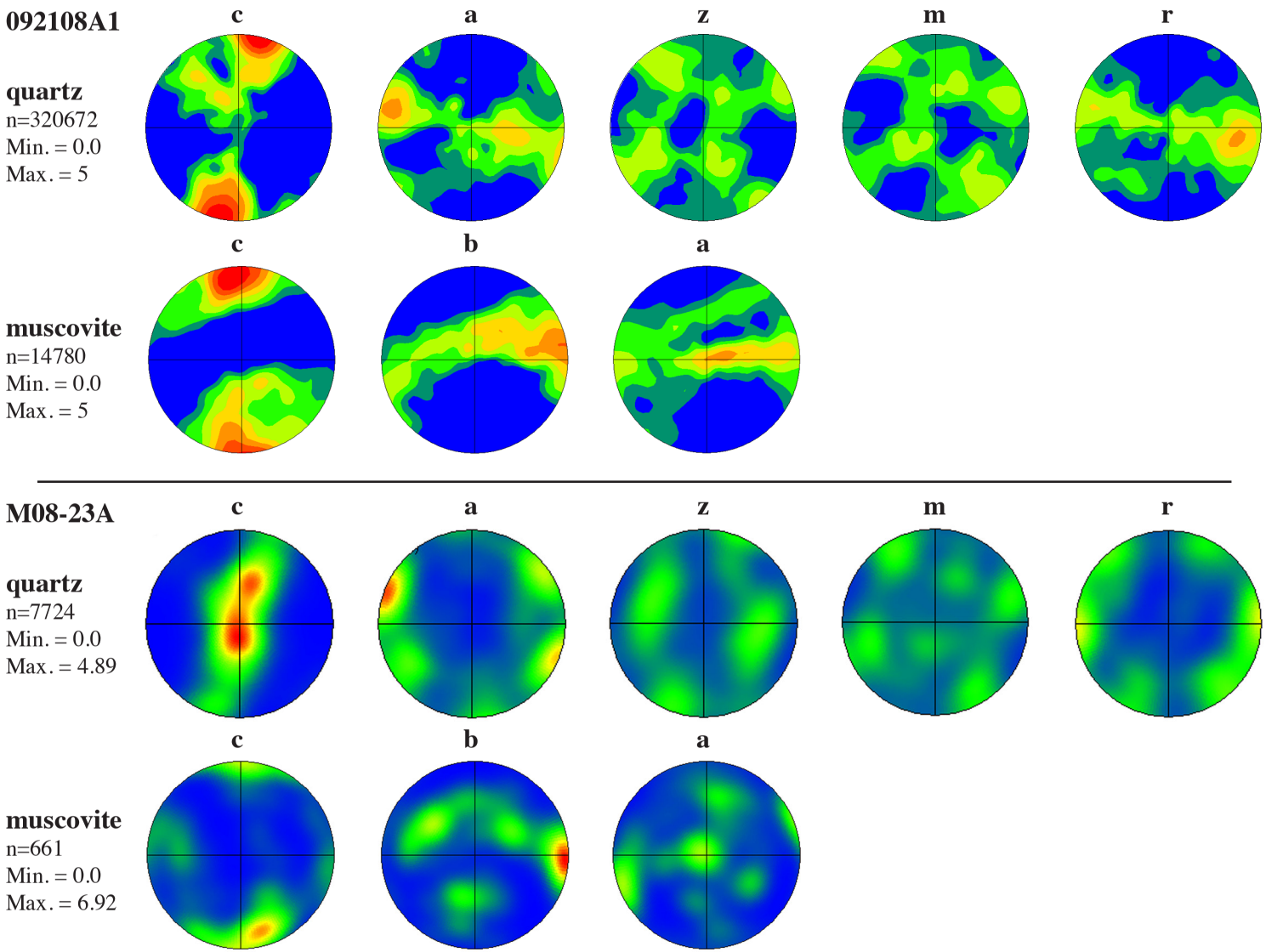

Figure 1.20. Pole figures of the c-axis (c), second order prisms (a), negative rhombs (z), first order prisms (m), and positive rhombs (r) for quartz data from samples 092108A1 and M08-23A. Muscovite data for both samples is plotted for c-axis (c), b-axis (b), and a-axis (a). The specimen reference frame is such that the foliation normal is N-S, and the lineation E-W.

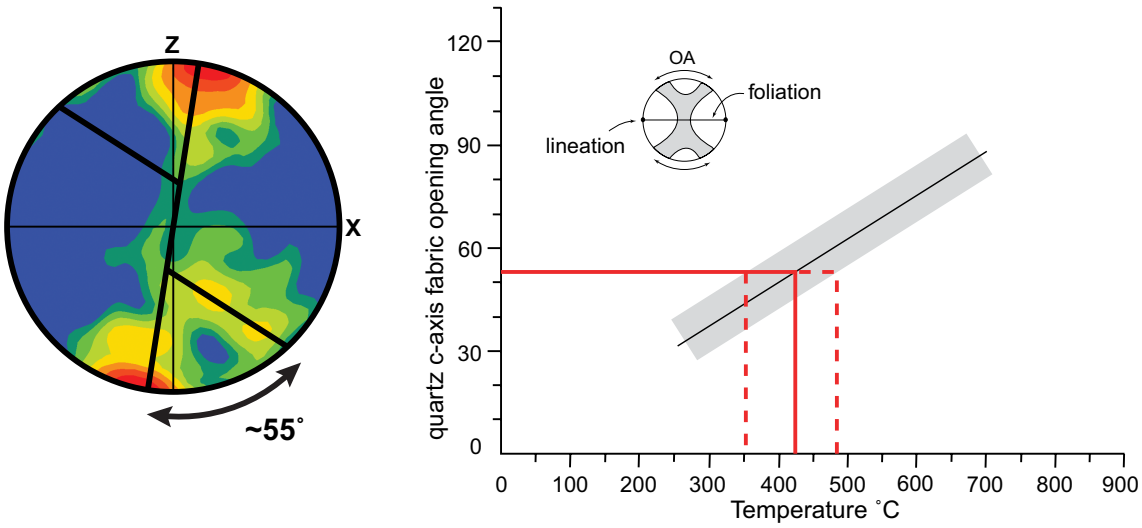

Figure 1.21. Quartz c-axis pole figure opening angle measurement for sample 092108A1 measuring ~55˚. This suggests a deformation temperature of ~415 ±50˚C.

Microscopy Core Facility in Laramie, Wyoming. Phase and orientation data were collected over a 1.5mm^2 area with an 8.7μm step size, for a total of ~30,000 data points. Specific operating conditions include a 20 kV accelerating voltage, 4.5nA beam current, 11mm working distance, and the sample was tilted to 70˚. Approximately 84% of all data points were indexed in the following modal proportions: 97% quartz, 2.6% muscovite and 0.3% sillimanite (Figure 1.19B). This is in general agreement with QEMSCAN analysis with the exception of a slight (3%) increase in quartz proportions.

Textural data are plotted in figure 1.20. The quartz c-axis pole figure reveals a slightly higher grade type-I girdle (Lister, 1977, Schmid and Casey, 1986). This pattern is consistent with quartzite samples deformed under amphibolite facies conditions (Schmid and Casey, 1986). The observations of Shaw (2002) and the presence of sillimanite in the sample are also consistent with amphibolite facies metamorphism, however, due to the lack of a distinct crossed girdle Kruhl's opening angle measurement is not applicable to this sample. Muscovite data are also presented in Figure 1.20 and are consistent with observed composite fabric.

DISCUSSION

Deformation of Earth materials occurs by a variety of processes, governed by both internal and external factors (e.g. mineralogy, grain size, porosity, permeability, presence (or absence) of fluids, temperature, pressure, stress and strain rate). A direct relationship exists between the active deformation mechanisms within a rock and the resulting rock fabric. This relationship allows researchers to examine rock fabric and make some assertions about the conditions during deformation. Determining active deformation mechanisms in a given sample can be done to some degree by optical examination, and by evaluation of the crystallographic orientation of constituent phases. Crystallographic preferred orientation (CPO) refers to the development of a common orientation of crystal lattices as a result of intra-crystalline deformation (e.g. the general alignment of a population of quartz grain c-axes within a host rock). Examining the CPO of phases within a deformed rock yields insight into which slip systems (i.e. a slip plane and a slip direction) were active during deformation, and in turn, the temperature and pressure conditions during deformation.

Figure 1.22 illustrates the relationship between temperature and active quartz slip systems as well as the resulting c- and a-axis pole figures . Under low-grade metamorphic conditions (300-400 ˚C), quartz deformation is achieved primarily by dislocation glide and dislocation creep on basal planes in the <a> direction. Under these conditions dynamic recrystallization is accomplished by grain bulging and results in a type-I cross girdle quartz c-axis pattern. With increasing temperature (400-500 ˚C), prism-slip {m}<a> becomes active and dislocation creep is dominant. Sub-grain rotation is the primary recrystallization mechanism and single girdle quartz c-axis patterns are typical. At greater temperatures (500-700 ˚C) grain boundary migration becomes the dominant recrystallization mechanism and single girdle to “bull’s eye” quartz c-axis patterns are common. At temperatures above 700 ˚C, prism-slip {m}<c> in the c direction is dominant and results in a unique quartz c-axis pattern illustrated in figure 1.22 (Paschier and Trouw, 1996).

As seismic anisotropy is dictated in part by the degree of alignment among anisotropic phases, it seems reasonable to assert that quartz rich lithologies subjected to even the weakest

deformation conditions will exhibit a higher magnitude of anisotropy than undeformed lithologies with randomly oriented constituent grains. However, it is still uncertain how aligned quartz grains will influence seismic anisotropy in the presence of aligned micas. Examination of single crystal anisotropies of these phases (figure 1.1) reveals strikingly different anisotropic behavior. Muscovite, a monoclinic phase, exhibits its highest P-wave velocities (and the highest degree of shear wave splitting) in the crystallographic *a-b* plane. This plane exhibits the strongest elemental bonding within this phase. The slowest P-wave velocities occur parallel to the crystallographic *c*-axis (as well as the lowest degree of shear wave splitting) and coincides with the weakest bonding in muscovite. Quartz, a hexagonal phase, does not exhibit this kind of bonding anisotropy and its seismic anisotropy pattern is much more complex than that of muscovite. In an effort to address the uncertainty of how quartz and muscovite will effect crustal anisotropy, the seismic response of two quartzite samples were calculated using existing modal proportions, and over a range of quartz to muscovite ratios.

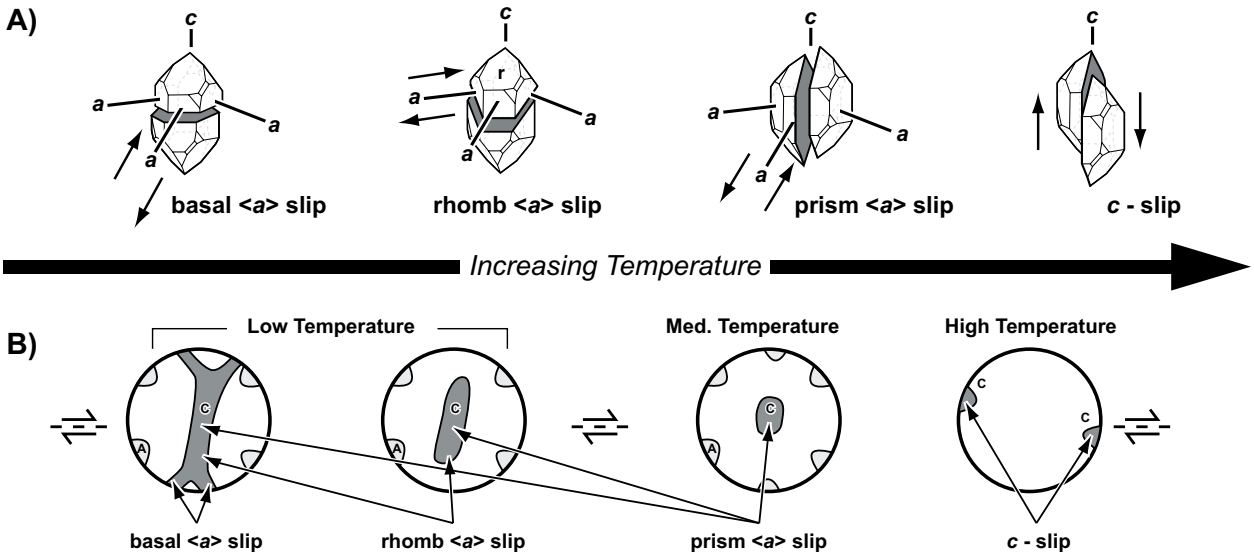

Figure 1.22 A) Activation of quartz slip systems as a function of temperature. B) Stereo projection of quartz c- and a-axis patterns resulting from activity on various slip systems. Modified after Klein, 2002 and Paschier and Trouw, 1996

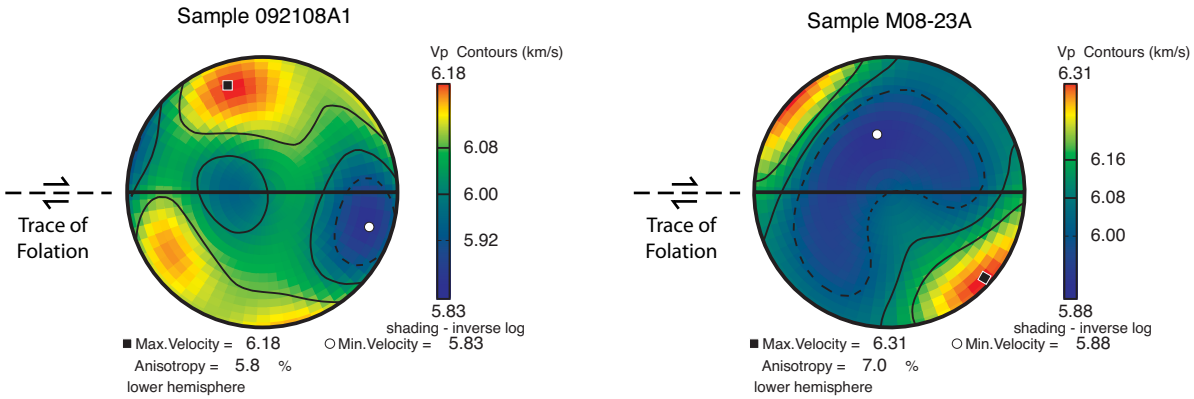

Figure 1.23 Stereographic projection of P-wave velocity anisotropy for samples 092108A1 (left) and M08-23A (right).

Figure 1.23 is a stereographic projection of the calculated P-wave anisotropies for quartzite samples 092108A1 and M08-23A using their existing modal proportions. Quartzite sample 092108A1 exhibits a maximum P-wave velocity of 6.18 km/s and a minimum velocity of 5.83 km/s, for an anisotropy of 5.8%. Quartzite sample M08-23A exhibits a maximum P-wave anisotropy of 6.31 km/s and a minimum velocity of 5.88 km/s, for an anisotropy of 7.0%. Both sample anisotropies approximate a hexagonal symmetry with a fast symmetry axis.

Velocity anisotropy was calculated for both quartzite samples over a range of quartz to muscovite ratios (Figures 1.24 and 1.25). Data from sample 092108A1 (Figure 1.24) were used to calculate a maximum anisotropy of approximately 37%, when calculated at 100% muscovite and 0% quartz. The minimum anisotropy calculated for this sample is approximately 4%, and occurs at around 88% quartz and 12% muscovite. It is at this composition that the addition of either phase, quartz or muscovite, results in an increase in seismic anisotropy. At a composition of 100% quartz, the resulting anisotropy is approximately 7%. Data from sample M08-23A (Figure 1.25) were used to calculate a maximum anisotropy of approximately 11%, at a composition of 100% muscovite. The minimum anisotropy calculated for this sample is approximately 5% and occurs at a composition of about 67% quartz and 23% muscovite. Similar to sample 092108A1, it is at this composition that the addition of either quartz or muscovite results in an increase in seismic

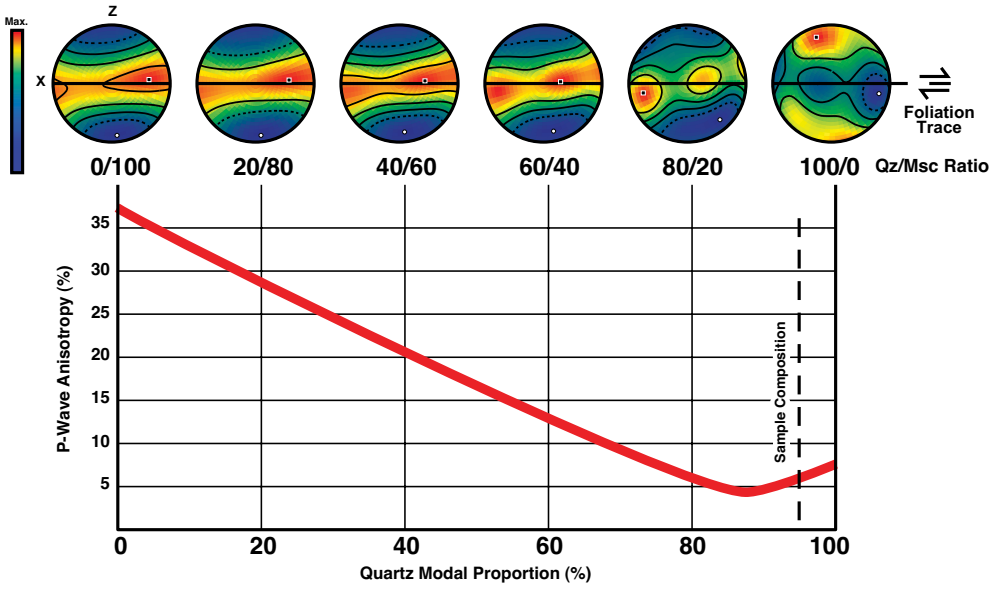

Figure 1.24. P-wave anisotropy calculations for varying modal proportions of quartz and muscovite from sample 092108A1 following Mainprice, 1990. Hemispheres represent equal area lower hemisphere stereographic projection of seismic data.

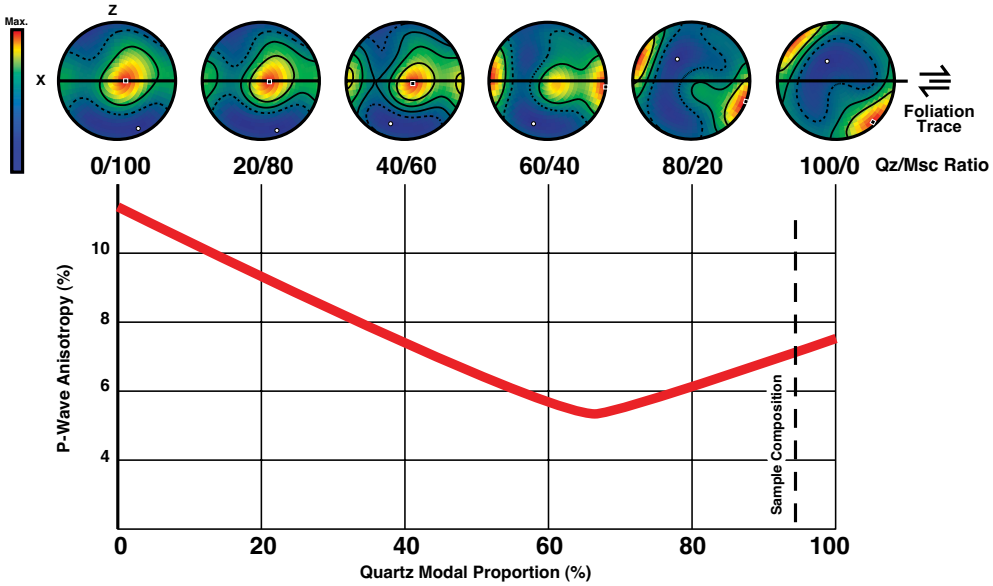

Figure 1.25. P-wave anisotropy calculations for varying modal proportions of quartz and muscovite from sample M08-23A following Mainprice, 1990. Hemispheres represent equal area lower hemisphere stereographic projection of seismic data.

anisotropy. At a composition of 100% quartz, anisotropy is approximately 7%.

It is important to note that calculating anisotropy from these data over varying quartz to muscovite ratios does not necessarily represent real lithologies. For example, it is unlikely that a lithology of 100% muscovite exists within the middle continental crust. In addition, lithologies with high mica content are more likely to partition strain into weaker phyllosilicate phases, and may alter the development of quartz deformation mechanisms and therefore the resulting quartz CPO and seismic response. Nonetheless, the results of these calculations do have some important implications. For instance, calculations from both samples reveal minimum anisotropy of about 5% that occurs between approximately 70% to 80% quartz. It is at this composition that the addition of either phase results in an increase in anisotropy. This coincides with a shift in the anisotropy symmetry axis from slow in more micaceous compositions, to fast in quartz rich compositions. These results suggest that although micas are the most anisotropic phase in continental crust, they may not dominate the magnitude or orientation of anisotropy in some rock types at modal proportions of less than 20 to 30%. Additional research on this issue should investigate the influence of quartz deformed over a wider range of metamorphic conditions and in rocks with varying modal prportions at similar metamorphic conditions. It would also be pertinent to compare calculated anisotropy to measured anisotropy in the lab, and anisotropic observations from field data.

A striking difference exists between the calculated maximum anisotropies of each sample. The maximum P-wave anisotropy for sample 092108A1 is approximately 37% at 100% muscovite. This is close to the muscovite single crystal P-wave anisotropy of 44.2% as reported by Ji and others (2002). The discrepancy between the calculated value for this sample and the single crystal value can be easily explained by differences in orientation of multiple muscovite grains in this sample (Figure 1.20) that diminish the magnitude of anisotropy. However, the maximum P-wave anisotropy for sample M08-23A is only 11%. This discrepancy is likely owed to differences in muscovite orientation data collection methods between the two samples. The addition of EDS to EBSD data from sample 092108A1 led to an unusually high index rate for geological materials.

Data from sample M08-23A do not include chemistry and therefore suffered a lower index rate, particularly in muscovite. Additional indexing difficulties exist with muscovite EBSD data in both samples due to low intensity diffraction patterns generated from this phase. Again, data from sample 092108A1 were able to skirt this issue to some degree due to the additional chemical data, but this problem was prevalent in both samples. This is not the first study to experience difficulty collecting EBSD data from phyllosilicates. Valcke and others (2006), and Prior and others (2009) report difficulty analyzing phyllosilicates in their microstructural context. This issue was the motivating factor for experimenting with new a new method of sample preparation based on ion milling as discussed in chapter 2 of this work.

CHAPTER II - Improving EBSD Data on Phyllosilicate Bearing Geological Samples

INTRODUCTION

Electron backscatter diffraction (EBSD) is a technique ideally suited for textural analysis (Prior et al., 1999), however, attaining high quality EBSD data on polyphase geological materials is challenging. It is not uncommon to find EBSD studies that report indexing rates as low as 55% (e.g. Valcke et al., 2006). Although misindexing and non-indexing occur for several reasons, the intensity of individual EBSPs is an important factor. This factor is dependent upon several variables that include the material examined and the surface from which data is collected as well as the SEM-EBSD system and particular operating conditions. The nature of each phase (e.g. internal order, symmetry, degree of lattice defects, etc…) and the smoothness of the sample surface are probably the two most important factors to successfully collecting EBSD data on geological materials.

Phyllosilicates are historically difficult phases to characterize using EBSD (Valcke et al., 2006, Schwartz et al., 2009). The cause of this problem is under debate, however, prior studies suggest that the softness and perfect cleavage common to these phases make it difficult to prepare sample surfaces for data collection, and low symmetry and high lattice defect densities make it difficult to index data from these phases. If the underlying cause of poor phyllosilicate EBSD data is due to problems inherent in the lattice structure, this will be a limiting factor to any EBSD study on these phases. However, if the cause is due to difficulties with sample surface preparation, this can be remedied with evolving sample preparation techniques. Traditional geological sample preparation for EBSD involves stepwise mechanical polishing followed by minutes to hours of chemical/ mechanical polishing. This method is known to induce subsurface damage to crystal lattices, and can preferentially polish softer phases resulting in increased sample surface topography. Although this strategy has enabled users to collect EBSD data on phyllosilicates, these phases continue to be problematic. New techniques from the materials science community have shown drastic gains in

EBSD data quality on metals using ion-milling to prepare sample surfaces (Figures 2.1 and 2.2). This method uses a low energy argon ion beam to sputter material away from the sample surface while inducing minimal subsurface damage (Walck, 2009).

To test the application of this method to geological samples, the quality of EBSD data before and after ion polishing was compared from a micaceous quartzite and a quartz bearing schist from the Cheyenne belt, southeastern Wyoming.

METHODS

The general plan for this experiment is as follows: a) prepare samples via traditional protocol for EBSD, b) collect EBSD data from specific, repeatable locations in each sample, c) ion mill each sample d) re-collect EBSD data under identical conditions and from identical locations in each sample and e) compare the image-quality factor of before and after EBSD data.

Two sample lithologies containing varying degrees of quartz and mica were chosen. The first, a micaceous mylonitic quartzite (Xmq, sample 090708B1) contains approximately 95% quartz and 3.5% muscovite. The second, a slate (Xf, sample MB07-08) contains 20% biotite, 30% muscovite, 25% quartz, 20% feldspar and 5% chlorite. These samples were strategically chosen to target lithologies that were a) dominantly hard phases (quartz) with a small percentage of softer phases (mica) and b) dominantly soft phases with a lesser percentage of hard phases. A total of six standard geological thin sections were prepared (three from each lithology), cut according to a kinematic reference frame and included x-z, x-y and oblique (i.e. 45˚ between y and z and containing x) sections from each lithology. This variation in sample orientation was selected to address the possibility of increasing the quality of EBSPs by simply collecting data from different crystallographic orientations as has been suggested by other authors (i.e. Reddy, personal communication). Each section underwent a minimum of 1 and a maximum of 2 hours of chemical-mechanical polishing with sub-micron colloidal silica, the same protocol as described in chapter 1.

EBSD data were collected at the University of Colorado's Nanomaterial Characterization

Facility using an FEI Nova 600i scanning electron microscope with an EDAX-TSL EBSD attachment. Collection and analysis of these data were done using EDAX-TSL's OIM software applications. Specific operating conditions for each sample are listed in tables 2.1 and 2.2.

Ion milling was conducted using the South Bay Technology, Inc. IBS/e ion beam sputter deposition and etching system and KRI kaufman ion source (Figures 2.3 and 2.4). The general approach to milling was 2-stage and included a short duration, high energy, high incident angle step (as measured from the sample normal) intended to reduce sample surface topography, followed by a longer duration, low energy, high incident angle step to remove the damage imparted by prior milling and to polish the sample. Samples were either continuously rotated or oscillated during milling to distribute incident ions over a greater sample area. The exact IBS/e operating conditions for each sample are listed in table 2.3.

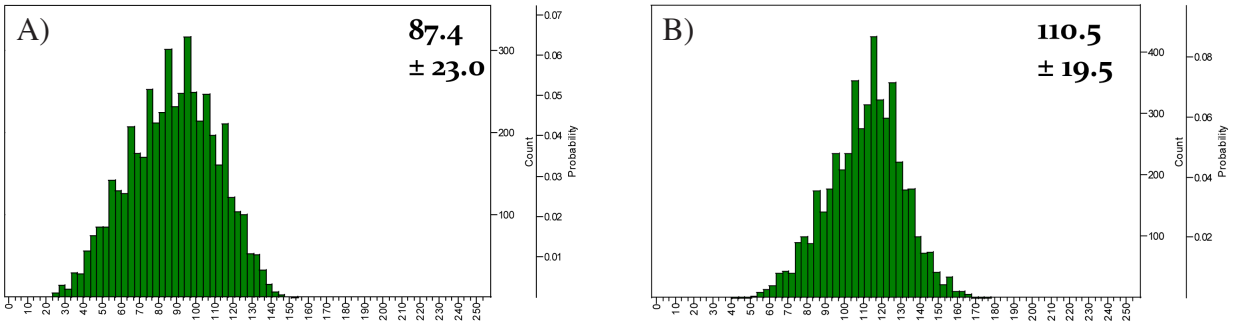

Figure 2.1. Band contrast histograms of EBSD data from Ti-6Al-4V Sample 1. A) Results from mechanically polished with 2 minutes of colloidal silica polish, B) Results from ion polishing the same sample in an overlapping area.

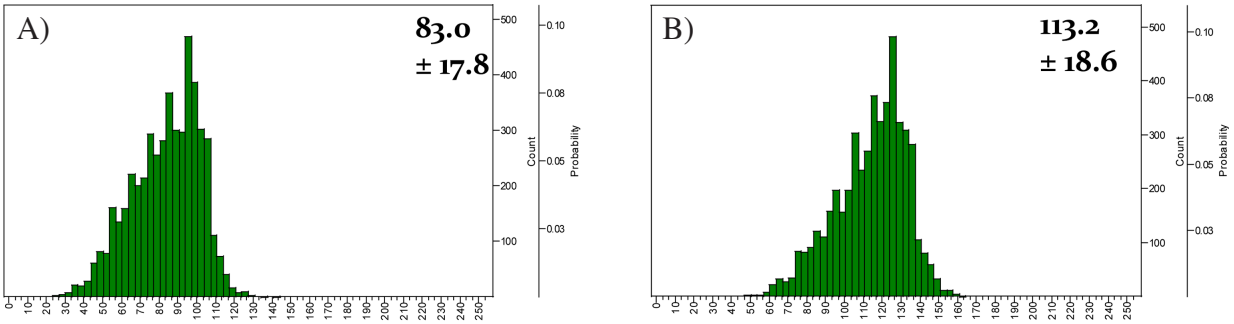

Figure 2.2. Band contrast histograms of EBSD data from Ti-6Al-4V Sample 2. A) Results from mechanically polished with 30 minutes of colloidal silica polish, B) Results from ion polishing the same sample in an overlapping area.

The image quality factor (IQ) is a measure of the overall intensity and sharpness of an individual diffraction pattern. Comparison of this factor between data sets was done by plotting the relative frequency of IQ values; i.e. how often a given IQ value occurs within an individual data set. These data can be plotted in map form such that each pixel is assigned a grayscale value that relates to the IQ value of that data point (black = low, white = high). This factor is preferable for comparing data over the index rate as indexing relies heavily on how well sample lattice parameters match those in a look up table. In mineral systems as complicated as muscovite and biotite, where lattice parameters change according to chemistry and conditions during growth, EBSD may not index well against a look up table without additional chemical data.

SAMPLE DESCRIPTION

Sample 090708B1 (Figure 2.5) is a mylonitic quartzite (Xmq) from the Cheyenne belt, southeastern Wyoming. Grain size is very fine (~10-100μm) and hand samples appear gray to white. Mineralogy consists of quartz, muscovite and minor accessories (opaque oxides). A strong foliation defined by aligned muscovite is visible at hand sample scale and oriented approximately 255, 70. A mineral lineation, defined by aligned quartz grains, is also visible in hand samples and is oriented approximately 66 > 025. Primary sedimentary structures are absent. A thin section of this sample reveals a composite s-c fabric (Figure 2.5) defined by aligned muscovite and a shape preferred orientation of quartz grains. This fabric suggests dextral shear sense and is consistent with a south side up interpretation of the northern shear zone of the Cheyenne belt.

MB07-08 (figures 2.6) is a sample of the French Slate (Xfs) from the Cheyenne belt, southeastern Wyoming. Grains are very fine (~10-100μm) and hand samples appear dark gray to black. Mineralogy consists of chlorite, biotite, muscovite, quartz, garnet and minor accessories. A strong foliation, defined by aligned mica, is oriented approximately 245, 82. A mineral lineation defined by elongate micas is oriented approximately 78 > 055 and is observable at the hand sample scale. An “s-c” fabric is present in thin section and suggests a dextral shear sense.

	Sample Identification	Accelerating Voltage (keV)	Specimen Current (nA)	Working Distance (mm)	Binning	Tilt Angle (°)	Map Length (µm)	Map Height (µm)	Step Size (µm)	Total Pixels
Pre-Ion Polish	MB07-08, XZ, Center	30	9.5	11.1	2x2	60	70	70	10	5711
	MB07-08, XZ, Edge	30	9.5	11.2	2x2	60	70	70	10	5711
	MB07-08, XY, Center	30	9.5	11.1	2x2	60	70	70	10	5711
	MB07-08, XY, Edge	30	9.5	11.1	2x2	60	70	70	10	5711
	MB07-08, 45, Center	30	9.5	11.6	2x2	60	70	70	10	5711
	MB07-08, 45, Edge	30	9.5	11.6	2x2	60	70	70	10	5711
	090708B1, XZ, Msc 1	30	9.5	11.4	2x2	60	55	55	0.775	5781
	090708B1, XZ, Msc 2	30	9.5	12	2x2	60	270	115	2.5	5859
	090708B1, XZ, Msc 3	30	9.5	11.5	2x2	60	90	40	0.9	5226
	090708B1, XZ, Qtz 1	30	9.5	11.4	2x2	60	55	55	0.775	5781
	090708B1, XZ, Qtz 2	30	9.5	12	2x2	60	270	115	2.5	5859
	090708B1, XZ, Qtz 3	30	9.5	11.5	2x2	60	90	40	0.9	5226
	090708B1, XY, Msc 1	30	9.5	11.1	2x2	60	200	150	2	5635
	090708B1, XY, Msc 2	30	9.5	11.1	2x2	60	140	140	2	5711
	090708B1, XY, Msc 3	30	9.5	11.1	2x2	60	135	145	2	5670
	090708B1, XY, Qtz 1	30	9.5	11.1	2x2	60	200	150	2.5	5635
	090708B1, XY, Qtz 2	30	9.5	11.1	2x2	60	140	140	2	5711
	090708B1, XY, Qtz 3	30	9.5	11.1	2x2	60	135	145	2	5670

Table 2.1. Pre-ion polish EBSD operating conditions by sample.

	Sample Identification	Accelerating Voltage (keV)	Specimen Current (nA)	Working Distance (mm)	Binning	Tilt Angle (°)	Map Length (μm)	Map Height (μm)	Step Size (μm)	Total Pixels
Post-Ion Polish	MB07-08, XZ, Center	30	9.5	11.1	2x2	60	70	70	10	5711
	MB07-08, XZ, Edge	30	9.5	11.2	2x2	60	70	70	10	5711
	MB07-08, XY, Center	30	9.5	11.6	2x2	60	70	70	10	5711
	MB07-08, XY, Edge	30	9.5	11.6	2x2	60	70	70	10	5711
	MB07-08, 45, Center	30	9.5	11.6	2x2	60	70	70	10	5711
	MB07-08, 45, Edge	30	9.5	11.6	2x2	60	70	70	10	5711
	090708B1, XZ, Msc 1	30	9.5	11.5	2x2	60	55	55	0.775	5781
	090708B1, XZ, Msc 2	30	9.5	11.5	2x2	60	270	115	2.5	5859
	090708B1, XZ, Msc 3	30	9.5	11.5	2x2	60	90	40	0.9	5226
	090708B1, XZ, Qtz 1	30	9.5	11.5	2x2	60	55	55	0.775	5781
	090708B1, XZ, Qtz 2	30	9.5	11.5	2x2	60	270	115	2.5	5859
	090708B1, XZ, Qtz 3	30	9.5	11.5	2x2	60	90	40	0.9	5226
	090708B1, XY, Msc 1	30	9.5	11.3	2x2	60	200	150	2	5635
	090708B1, XY, Msc 2	30	9.5	11.3	2x2	60	140	140	2	5711
	090708B1, XY, Msc 3	30	9.5	11.3	2x2	60	135	145	2	5670
	090708B1, XY, Qtz 1	30	9.5	11.3	2x2	60	200	150	2.5	5635
	090708B1, XY, Qtz 2	30	9.5	11.3	2x2	60	140	140	2	5711
	090708B1, XY, Qtz 3	30	9.5	11.3	2x2	60	135	145	2	5670

Table 2.2. Post-ion polish EBSD operating conditions by sample.

Sample Identification	Processing Step	Beam Voltage (V)	Beam Current (mA)	Accelerating Voltage (V)	Neutralizer Current (mA)	Optics	Rotation/ Oscillation	Time (min)	Incident Angle (˚)	Chamber Pressure (torr)	Purpose
MB07-08 XY	1	600	5	90	5	Collimated	Continuous Rotation	5	82	4.5x10-7	Remove Topography
MB07-08 XY	2	600	5	90	5	Collimated	Continuous Rotation	15	86	4.5x10-7	Smooth Surface Topography
MB07-08 XY	3	250	2.5	37	2.5	Collimated	Continuous Rotation	40	86	4.5x10-7	Polish Sample Surface
MB07-08 45	1	600	5	90	5	Collimated	Continuous Rotation	100	86	4.5x10-7	Smooth Surface Topography
MB07-08 45	2	250	2.5	37	2.5	Collimated	Continuous Rotation	100	86	4.5x10-7	Polish Sample Surface
MB07-08 XZ	1	600	5	90	5	Collimated	± 50˚ Oscillation	60	86	4.5x10-7	Smooth Surface Topography
MB07-08 XZ	2	250	2.5	37	2.5	Collimated	± 50˚ Oscillation	60	86	4.5x10-7	Polish Sample Surface
090708B1 XZ	1	600	5	90	5	Focusing	Continuous Rotation	20	85	4.5x10-7	Smooth Surface Topography
090708B1 XZ	2	250	2.5	37	2.5	Focusing	Continuous Rotation	40	85	4.5x10-7	Polish Sample Surface
090708B1 XY	1	600	5	90	NA	Focusing	Continuous Rotation	20	85	4.5x10-7	Smooth Surface Topography
090708B1 XY	2	250	2.5	37	NA	Focusing	Continuous Rotation	40	85	4.5x10-7	Polish Sample Surface

Table 2.3. IBS/e operating conditions by sample.

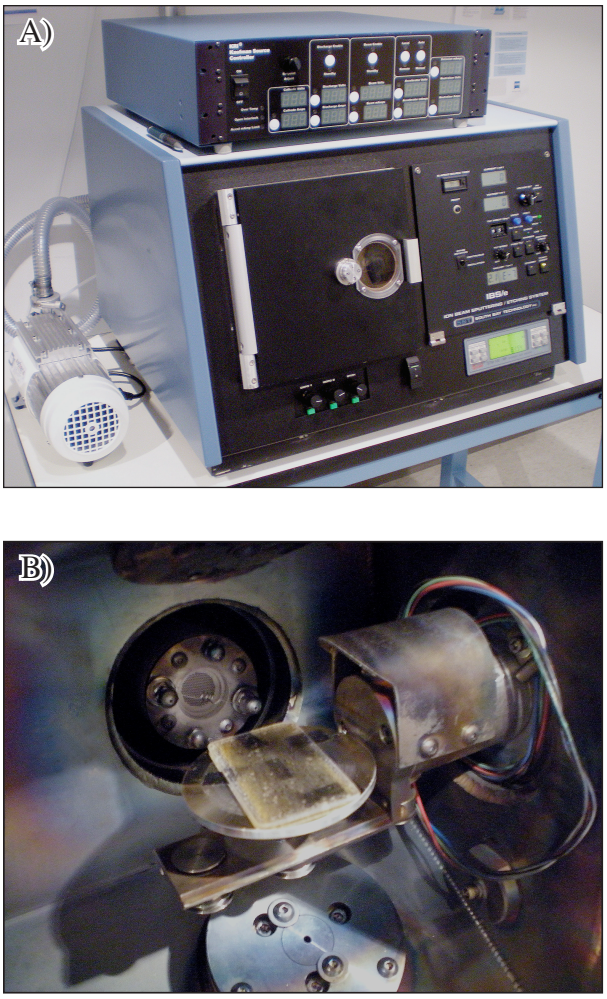

Figure 2.3. A) South Bay Technology, Inc. IBS/e ion bean sputter deposition and etching system. B) IBS/e sample chamber showing ion gun and stage configuration C) Geological thin section undergoing ion milling in the IBS/e.

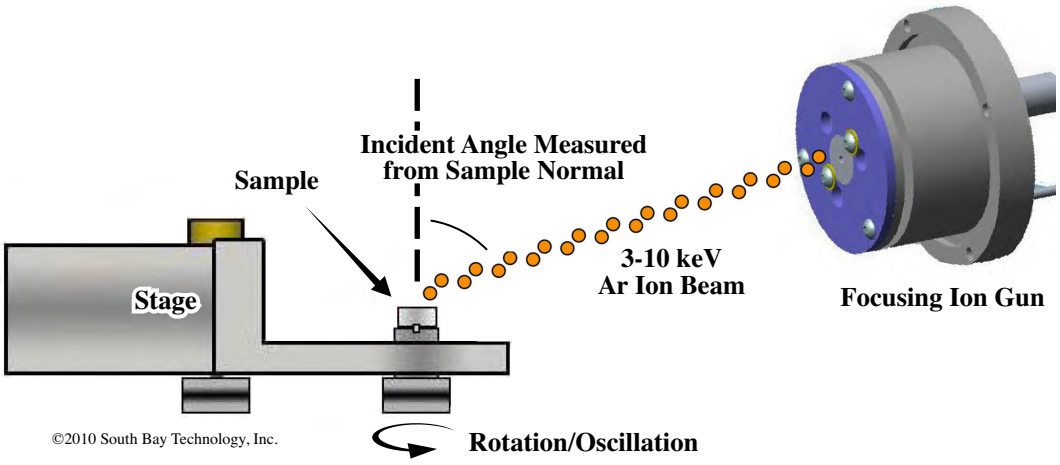

Figure 2.4. Schematic illustration of the South Bay Technology, Inc. IBS/e system stage and ion gun configuration.

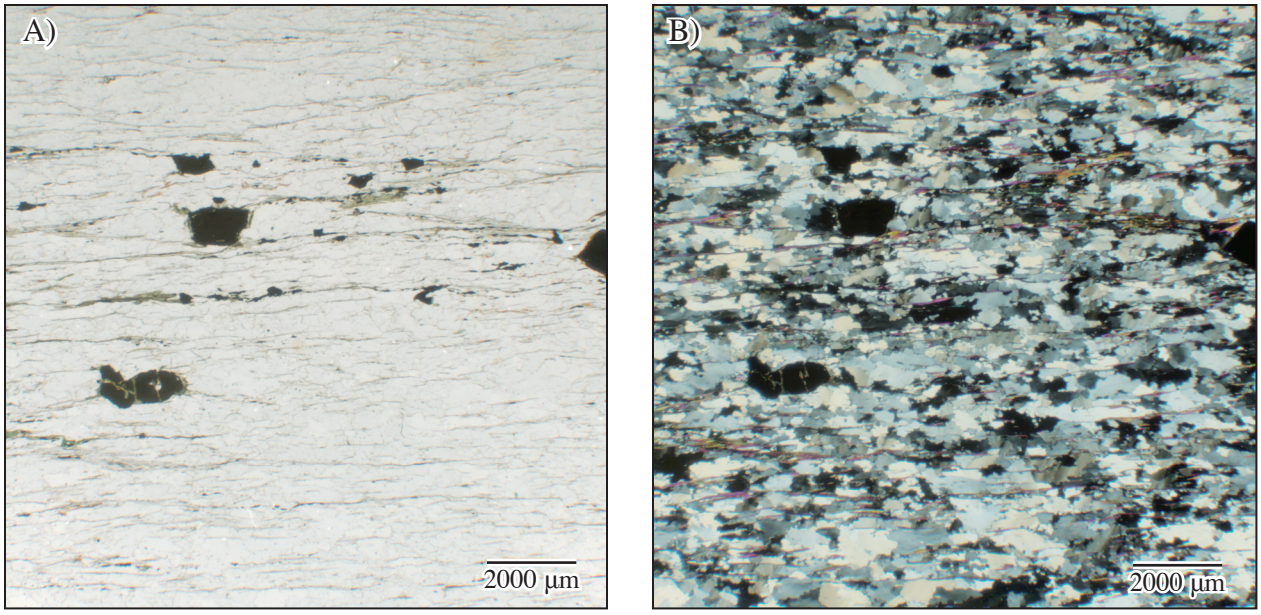

Figure 2.5. Plane polarized light (A) and cross-polarized light (B) photomicrographs of mylonitic quartzite sample 090708B1, XZ section.

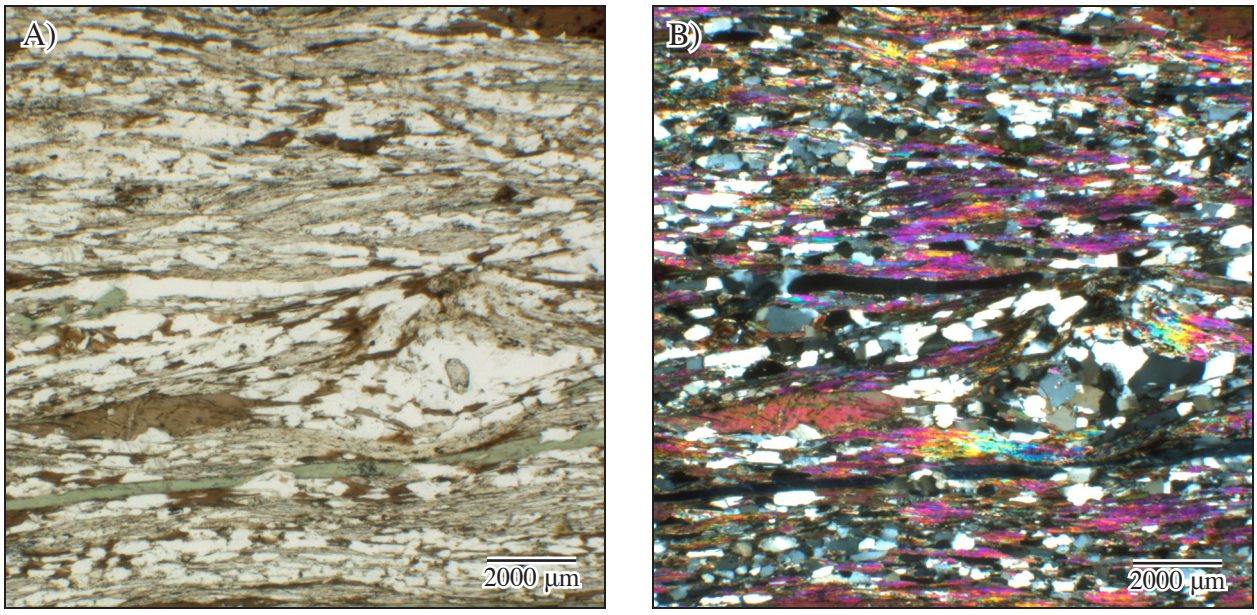

Figure 2.6. Plane polarized light (A) and cross-polarized light (B) photomicrographs of schist sample MB07-08, XZ section.

DISCUSSION

Figures 2.1 and 2.2 are histograms of EBSD data quality from two titanium alloy samples from a study performed by Walck et al., 2009. Sample 1 (Figure 2.1) initially underwent two minutes of colloidal silica polishing, followed by ion polishing. Sample 2 (Figure 2.2) underwent 30 minutes of colloidal silica polishing followed by ion polishing. A comparison of these two data sets does not reveal a statistical difference (at a 2σ standard deviation) between samples undergoing two minutes or 30 minutes of colloidal silica polishing and no ion polishing. The charts do reveal a statistical improvement in EBSD data on both samples after ion polishing. The primary conclusion from this study was that increasing the amount of colloidal silica polishing had little to no effect on EBSD data quality from a titanium alloy, and that ion polishing statistically improved the data quality to a consistent level regardless of the degree of colloidal silica polishing (Walck et al. 2009).

Although there is no standard practice for preparing geological samples for EBSD, most labs use minutes to hours of colloidal silica polishing as a final preparatory step. In chapter 1 of this study, polishing with colloidal silica for less than one hour was insufficient, and provided poor quality EBSD. This became the motivating factor for exploring ion polishing as a technique to cut down the amount of time spent polishing with colloidal silica, and to improve the overall quality of EBSD data on difficult phases, particularly micas.

Initial evaluation of ion polishing was done by comparison of pre- and post-ion polish data from a mica rich sample, M08-23A. EBSD data were collected over areas that contained multiple phases, focusing particularly on quartz and mica. A histogram of these data reveals no statistical difference in data collected before or after ion polishing (e.g. Figure 2.5 and 2.6) regardless of the orientation of the sample (i.e. x-z, x-y or oblique sections). Although the degree of improvement seen in homogeneous metal samples (Figures 2.1 and 2.2) was not expected in polyphase geologic materials, there was anticipation of some improvement in the overall quality of data after ion milling. Figure 2.7 is an image quality map that reveals an improvement in IQ values in the cores

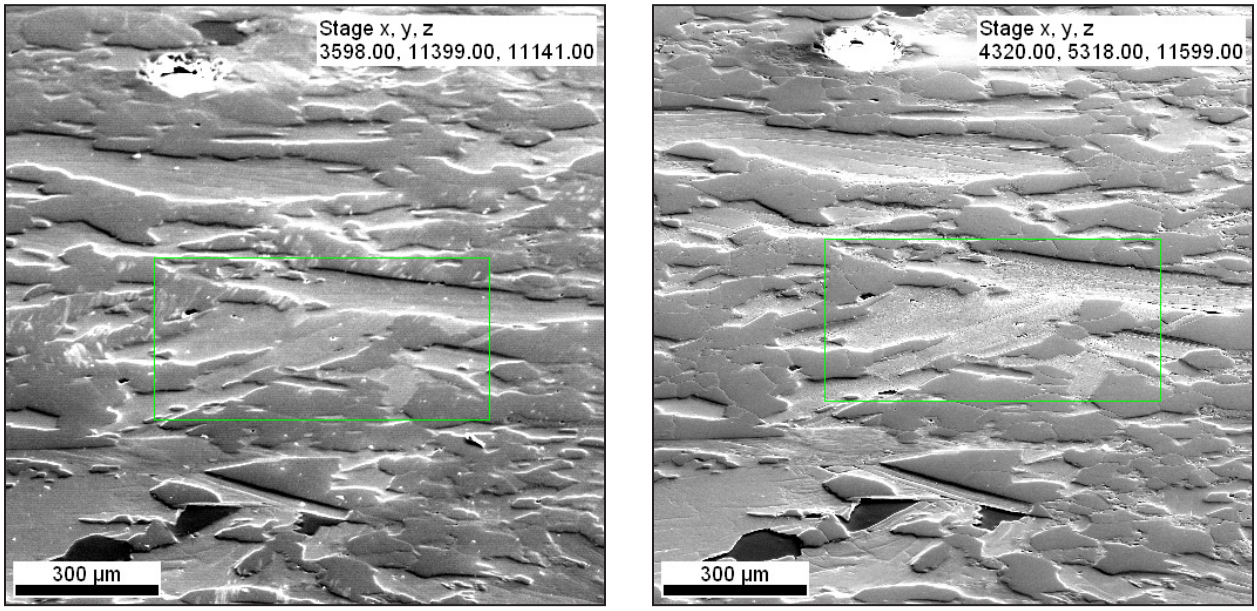

Figure 2.7. Pre- (left) and post-ion polish (right) secondary electron images of French Slate sample MB07-08, xy section, center map area. Green boxes denote mapped area.

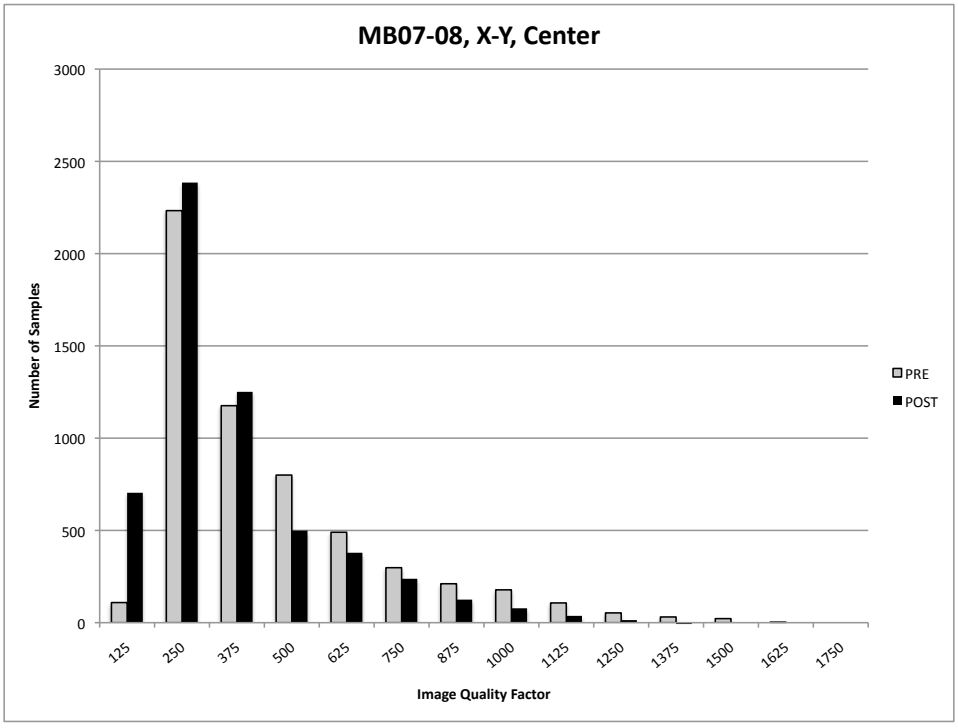

Figure 2.8. Histogram of pre- and post-ion polish image quality data for French Slate sample MB07-08, xy section, center map area.

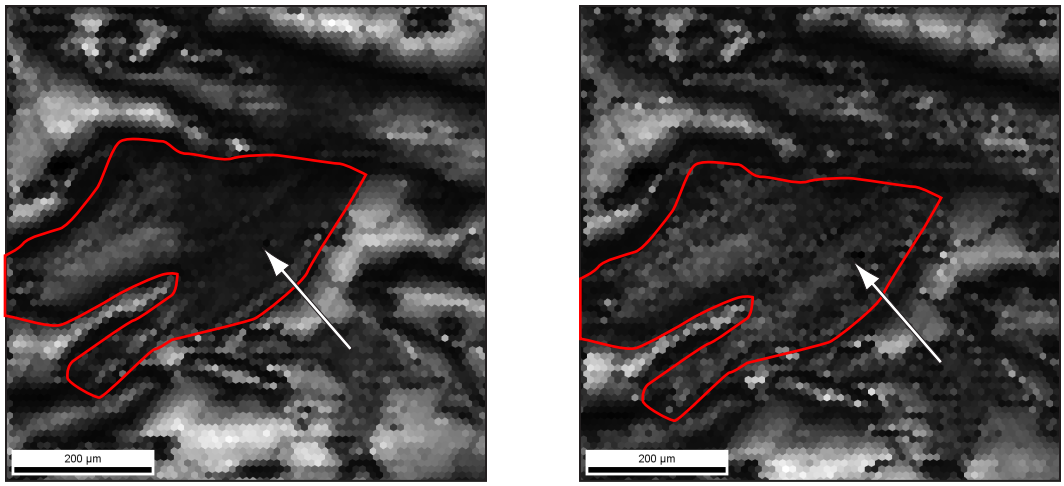

Figure 2.9. Image quality map for pre- (left) and post-ion polishing (right), sample MB07-08, xy section, center map area. Red line approximately outlines a muscovite grain, white arrow points to an area within a the grain where IQ values were improved due to ion milling

of most muscovite and quartz grains, but IQ values decrease along grain boundaries and at defects within grains. Similar results were seen in all schist samples (see appendix). Improvement in EBSD intensity from internal, defect free domains has been offset in these samples by a decrease in intensity, and therefore image quality, along grain boundaries and at grain defects.

When examining sample 092108A1, a quartz dominant lithology, the data collection approach was altered to compare pre- and post-ion polish IQ values from only quartz and only muscovite grains, as opposed to collecting data over larger, polyphase areas as in the previous example. This approach was adopted to explore the possibility of improving EBSD data quality in individual domains within a sample while avoiding phase boundaries (i.e. quartz and muscovite interfaces). Results from this analysis reveal an increase in EBSD IQ values in the defect free cores of both muscovite and quartz grains, and a decrease in IQ along grain boundaries and at grain defects, regardless of sample orientation (e.g. Figures 2.7, 2.8, and 2.9). These results are consistent with data from sample M08-23A, and all data from sample 090708B1 exhibit this behavior (see appendix).

A model proposed by Barna (1987) examines the effect of ion milling on topography in

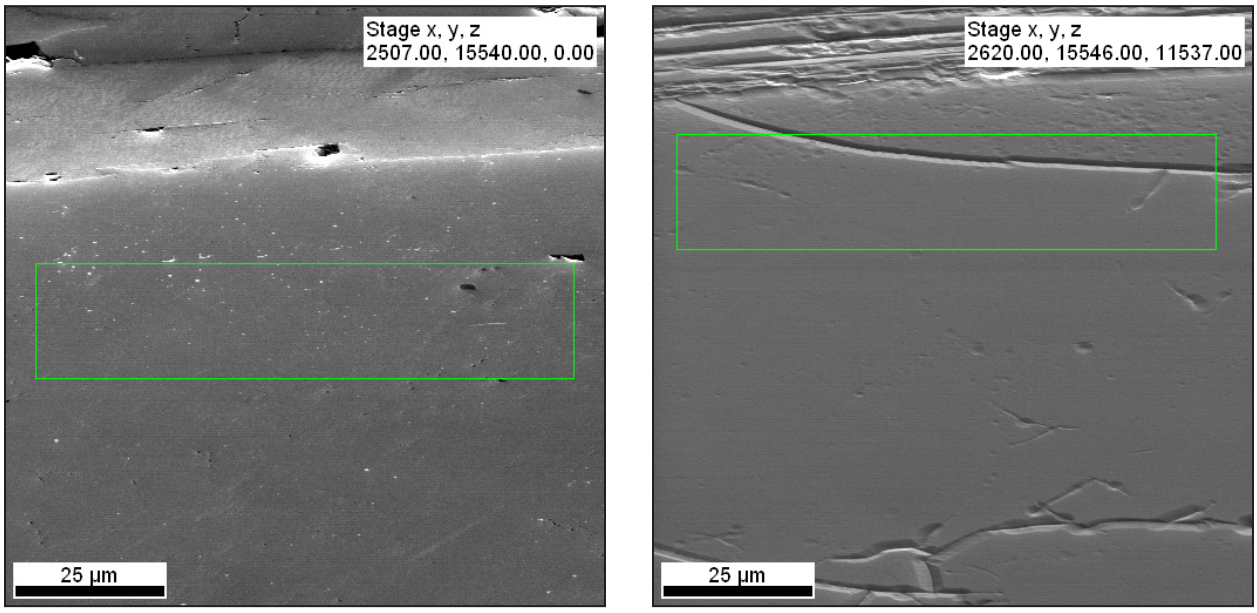

Figure 2.10. Pre- (left) and post-ion polish (right) secondary electron images of Quartzite sample 090708B1, X-Z section, quartz grain 3 map area. Green boxes denotes mapped area.

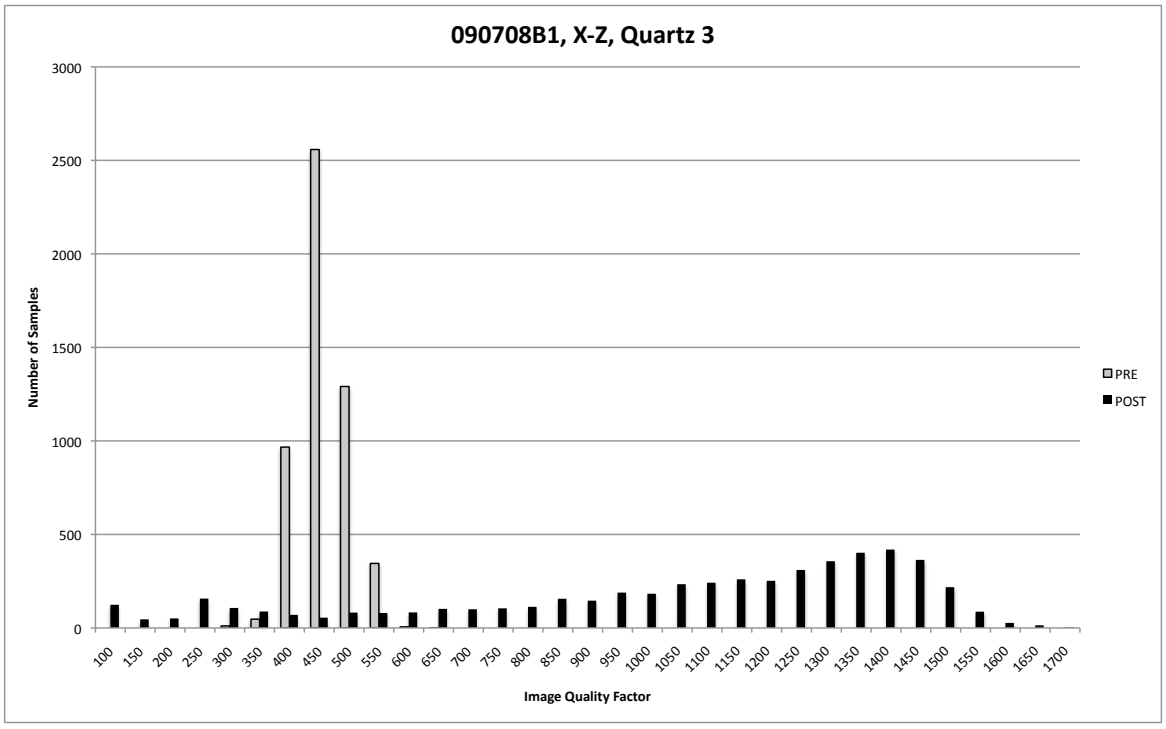

Figure 2.11. Histogram of pre- and post-ion polish image quality data for Quartzite sample 090708B1, X-Z section, quartz grain 3 map area.

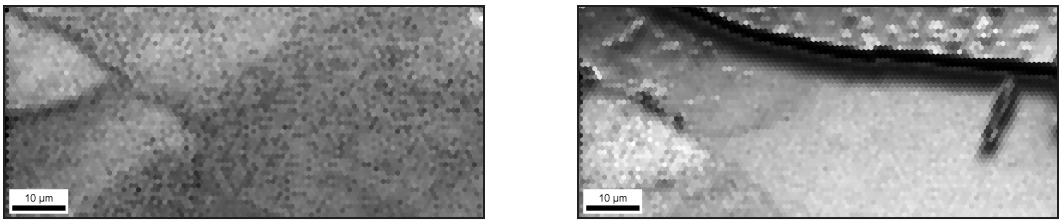

Figure 2.12. Image quality map of pre- and post-ion polish data for Quartzite sample 090708B1, X-Z section, quartz grain 3 map area.

homogeneous samples. This model suggests two scenarios are produced by ion milling a sample with existing topography (Figure 2.13). The resulting surface topography is dependent upon the incident angle of the ion beam, the material's sputter rate, and the initial shape of sample surface topography. Figure 2.13 illustrates the development of these scenarios through time. Figure 2.13A shows the resulting topography on a homogenous sample with a high sputter rate and high incident angle (as measured from the sample normal). The initial sample topography in this example (t1) is a sharp step that through time becomes concave (t2). Figure 2.13B shows modeled surface topography on a homogeneous sample with a high sputter rate, high incident angle, and low initial sample surface topography. Per Barna's model, this combination results in the development of convex topographic features. Secondary electron (SE) images of all EBSD map areas in this study show preferential etching along grain boundaries and at internal grain defects (e.g. Figure 2.10). The fact that IQ values are also lower in these areas can be explained using Barna's model. The development of sloped topography at grain boundaries and at grain defects has resulted in low intensity EBSD data in these regions, possibly because the EBSP center is shifted away from the

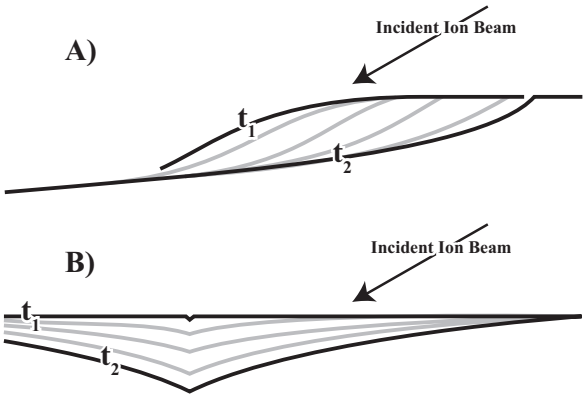

Figure 2.13. Cross-sectional model results of sample surface topography changes during ion polishing. A) Development of concave topographic features. B) Development of convex topographic features. (Adapted from Barna, 1987)

EBSD sensor in these regions, or due to some increased interference among exiting electrons along the slopes, or due to a shadowing of the electron beam during EBSD data collection. Whatever the cause may be, it is obvious that a decrease in image quality corresponds primarily with sample areas that are preferentially etched.

Barna's model only considers materials of homogenous composition, a feature not present in most phyllosilicate bearing geological materials. A more complex model that considers materials of differing sputter rates would likely show an increase in sample surface topography through time and may more adequately model the behavior of geological materials. However, this model can be used to understand the results of this study. Although there is an improvement within the low relief, inclusion free domains of both quartz and muscovite grains, preferential etching along grain boundaries is sufficient to keep post-ion polish EBSD data statistically equal to pre-ion polish data. These results are not conclusive enough to endorse, or negate ion milling as a means of improving EBSD data quality in all geological materials, however, if ones purpose is simply to acquire a statistical representation of orientation data, particularly for coarse grained materials,

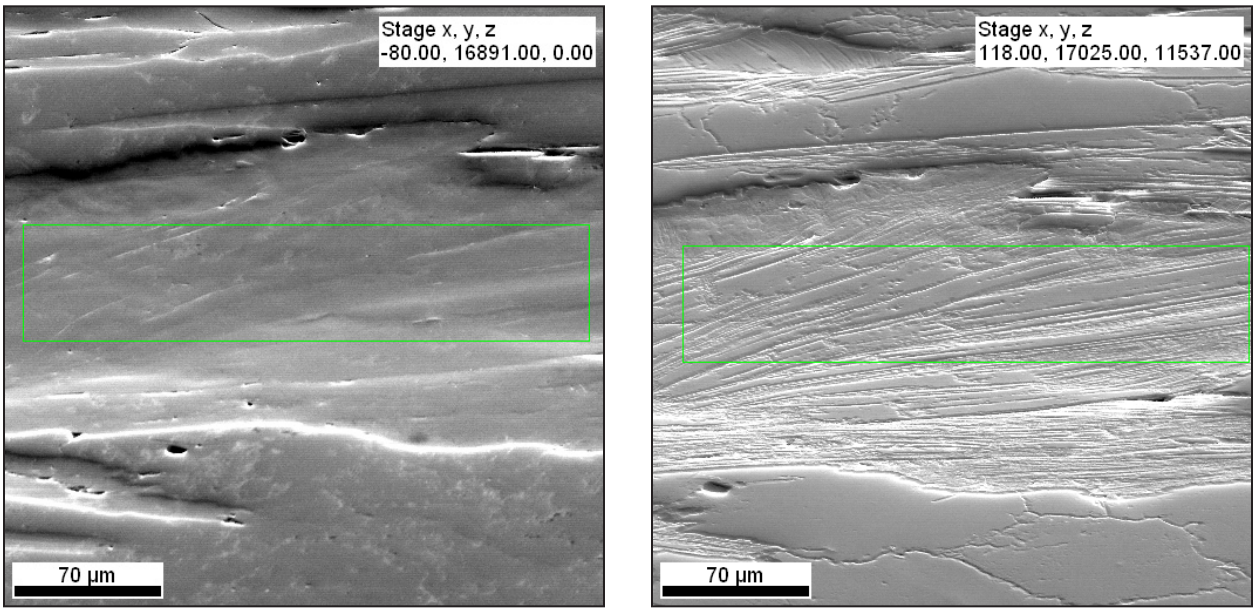

Figure 2.14. Pre- (left) and post-ion polish (right) secondary electron images of Quartzite sample 090708B1, X-Z section, muscovite grain 2 map area.

this method can serve to improve the quality of intragranular EBSD data on problematic phases. Phyllosilicates in this study tended to be fine grained (~10-100μm) and were often interspersed between harder phases, a scenario present in most phyllosilicate bearing geological materials. This combination resulted in a minimal improvement in the EBSD data from these phases. In addition, phyllosilicates commonly exhibit a tetrahedral-octahedral-tetrahedral (t-o-t) "sheet" that is bonded to other t-o-t sheets via weak van der Waals bonds. This type of structure has preferentially etched along the weak t-o-t interfaces resulting in increased topographic difference within muscovite grains in this study (Figure 2.14). Therefore, the conclusion is drawn that difficulty in collecting EBSD on phyllosilicates in this study is most likely due to the crystalline structure of such phases, and less a result of poor mechanical polishing. Ion milling does not appear to get around this issue any better than traditional chemical/mechanical means.

Further research on this issue will focus on reducing the initial topographic difference between phases induced by preferential mechanical polishing of the softer micas, and then exploring ion milling as a means to smooth sample surfaces. Additional work should also examine differential sputter rates between phases as this may cause increased sample surface topography by preferentially milling phases with higher sputter rates.

APPENDIX

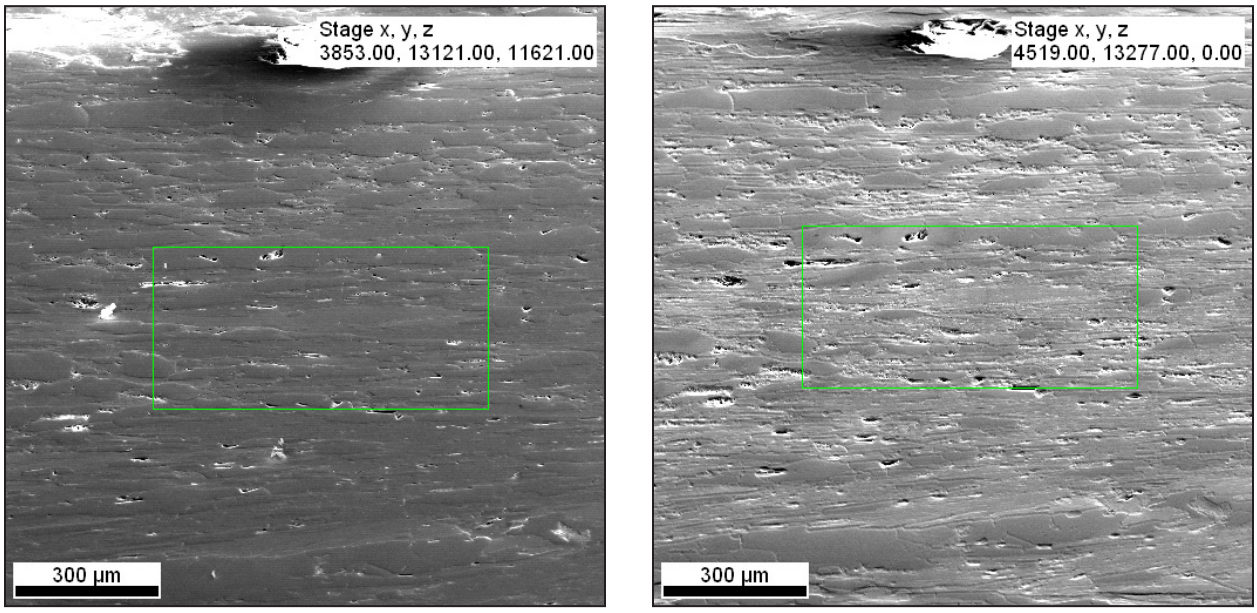

Figure A.1. Pre- (left) and post-ion polish (right) secondary electron images of French Slate sample MB07-08, X-Z section, center map area.

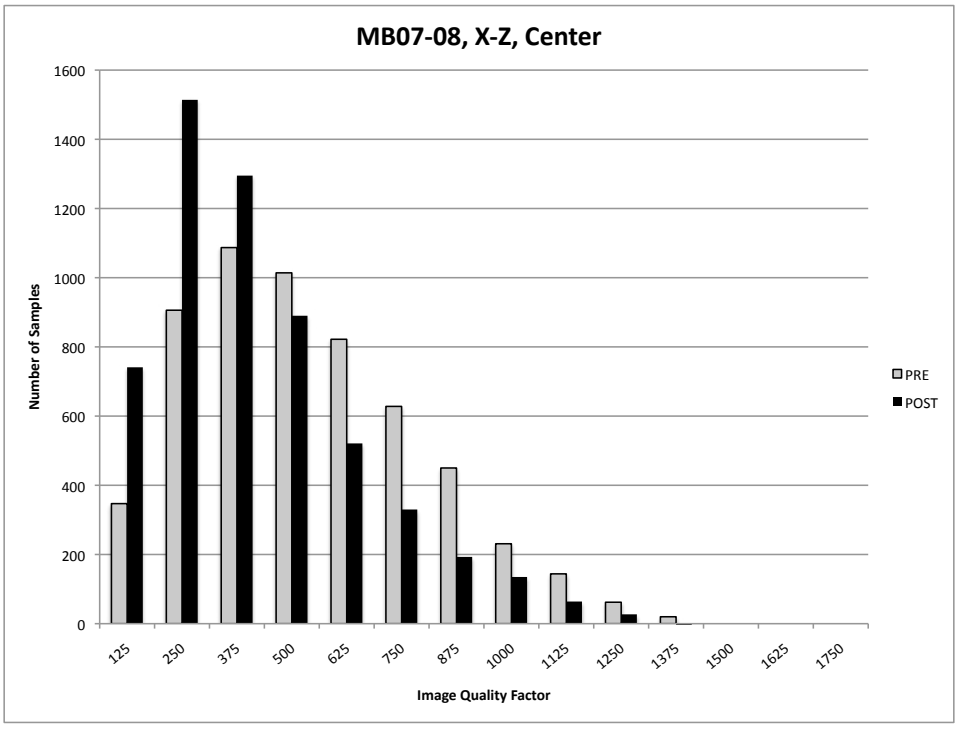

FigureA.2. Histogram of pre- and post-ion polish image quality data for French Slate sample MB07-08, X-Z section, center map area.

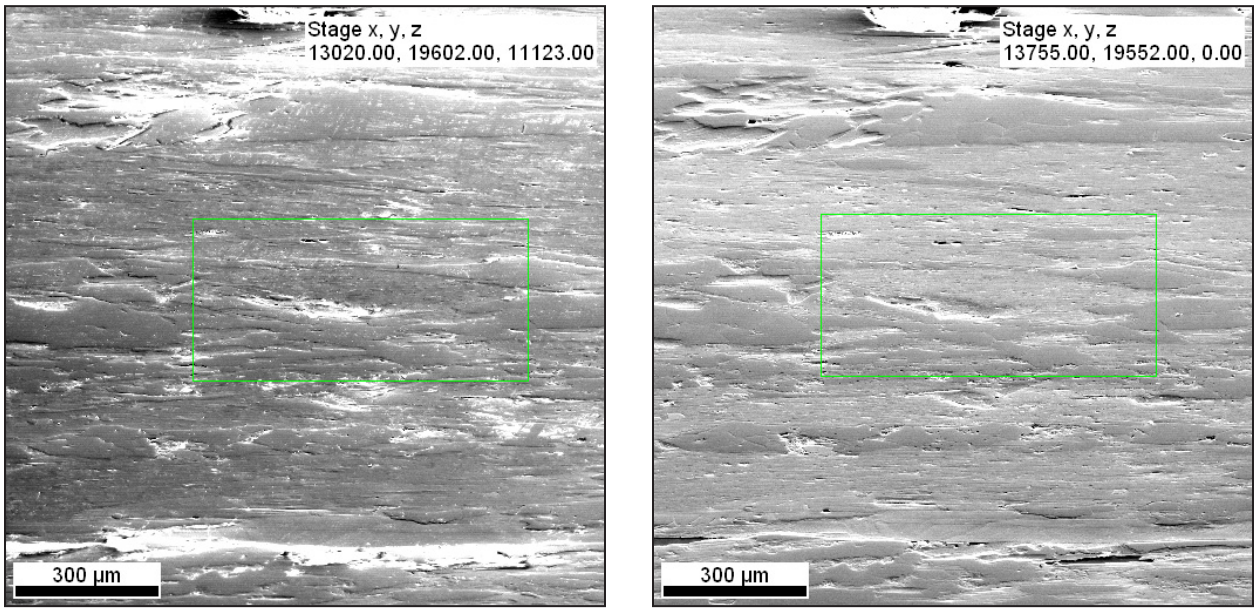

Figure A.3. Pre- (left) and post-ion polish (right) secondary electron images of French Slate sample MB07-08, X-Z section, edge map area.

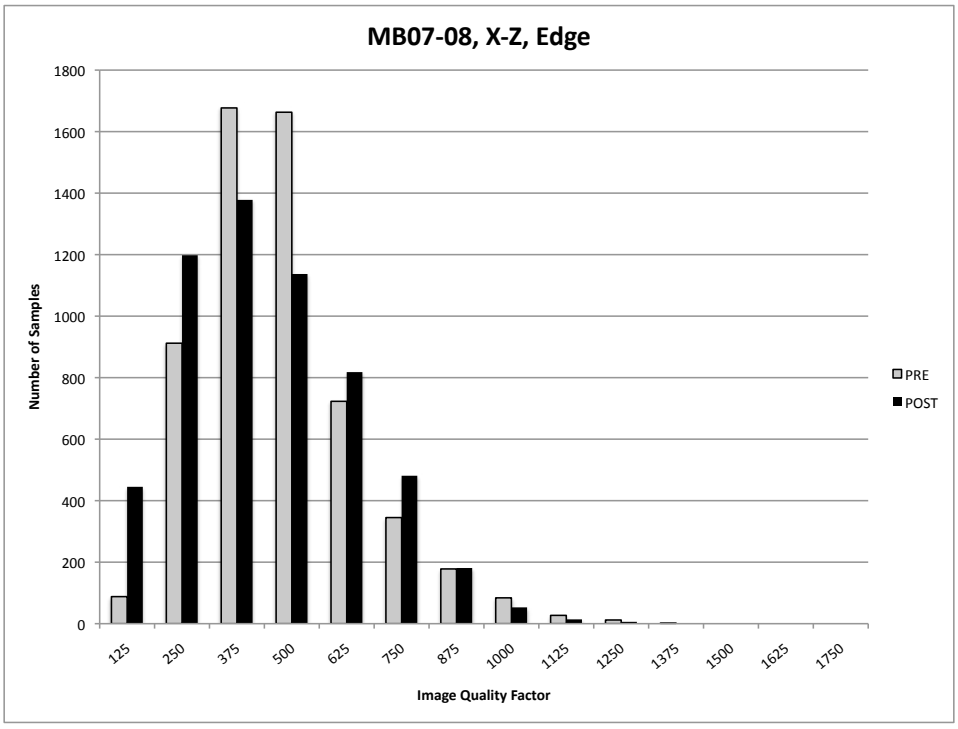

Figure A.4. Histogram of pre- and post-ion polish image quality data for French Slate sample MB07-08, X-Z section, edge map area.

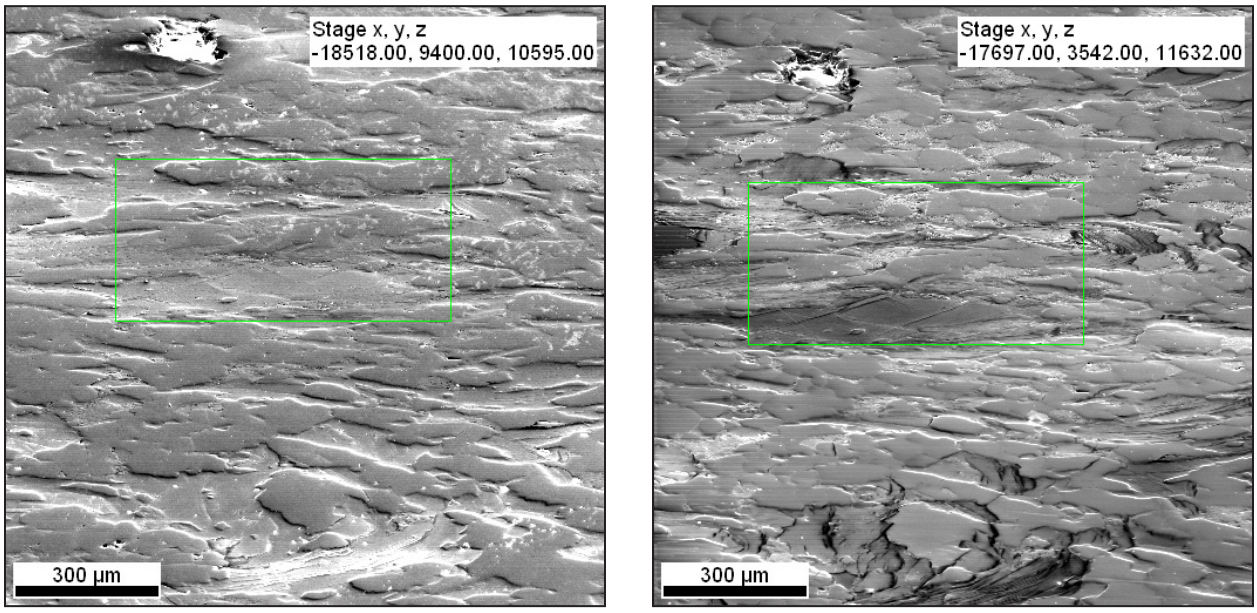

Figure A.5. Pre- (left) and post-ion polish (right) secondary electron images of French Slate sample MB07-08, X-Y section, edge map area.

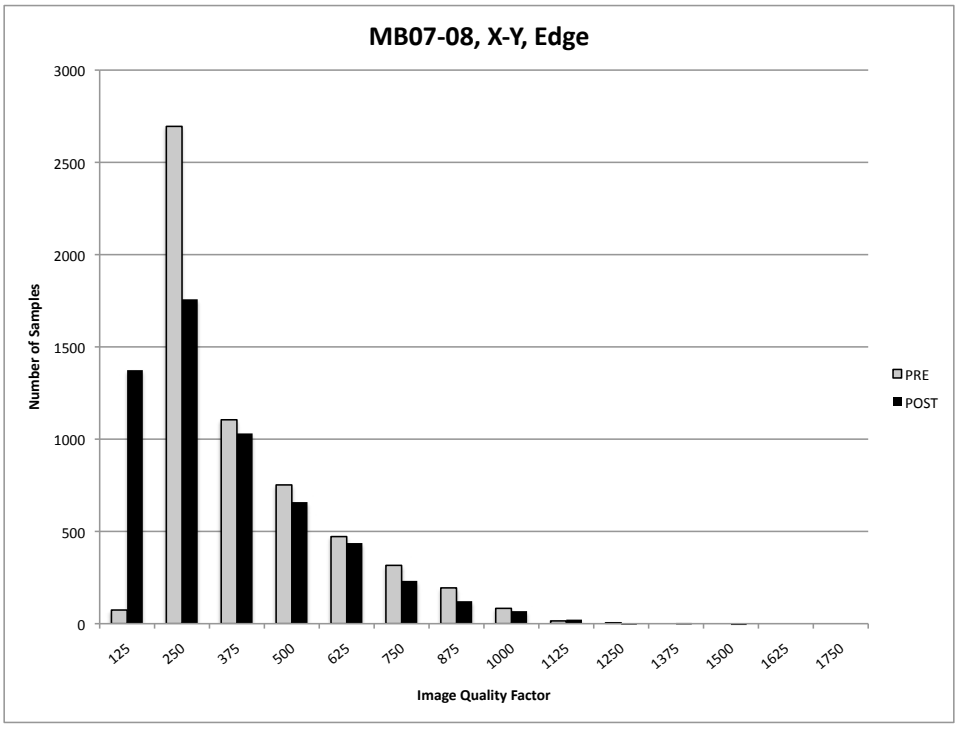

Figure A.6. Histogram of pre- and post-ion polish image quality data for French Slate sample MB07-08, X-Y section, edge map area.

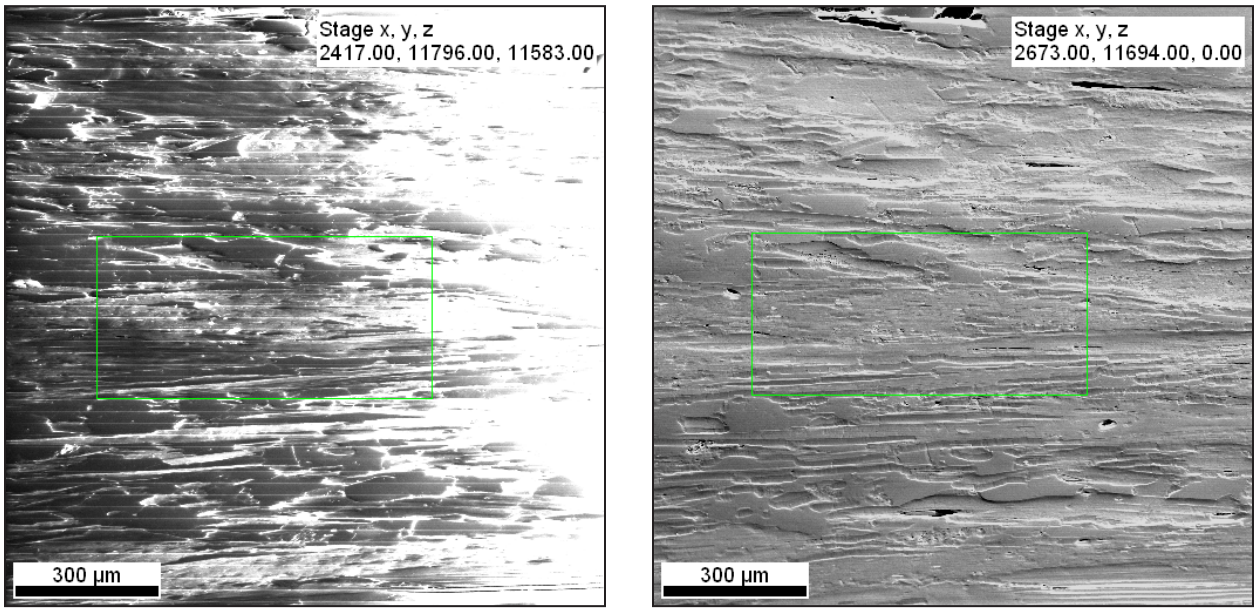

Figure A.7. Pre- (left) and post-ion polish (right) secondary electron images of French Slate sample MB07-08, 45˚ section, center map area.

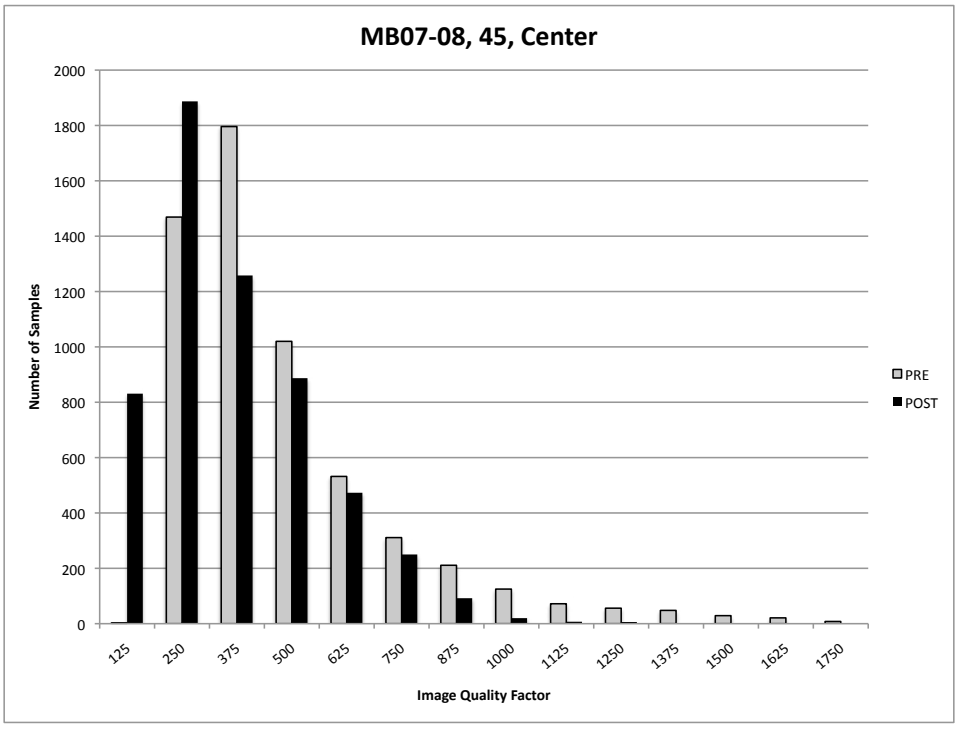

Figure A.8. Histogram of pre- and post-ion polish image quality data for French Slate sample MB07-08, 45˚ section, center map area.

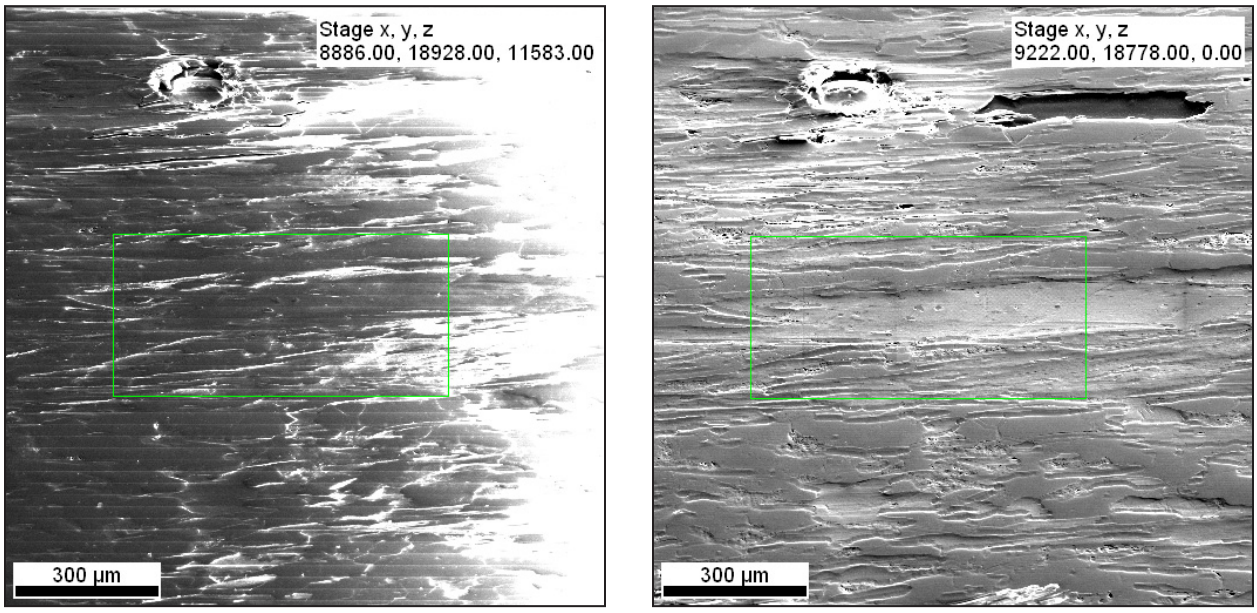

Figure A.9. Pre- (left) and post-ion polish (right) secondary electron images of French Slate sample MB07-08, 45˚ section, edge map area.

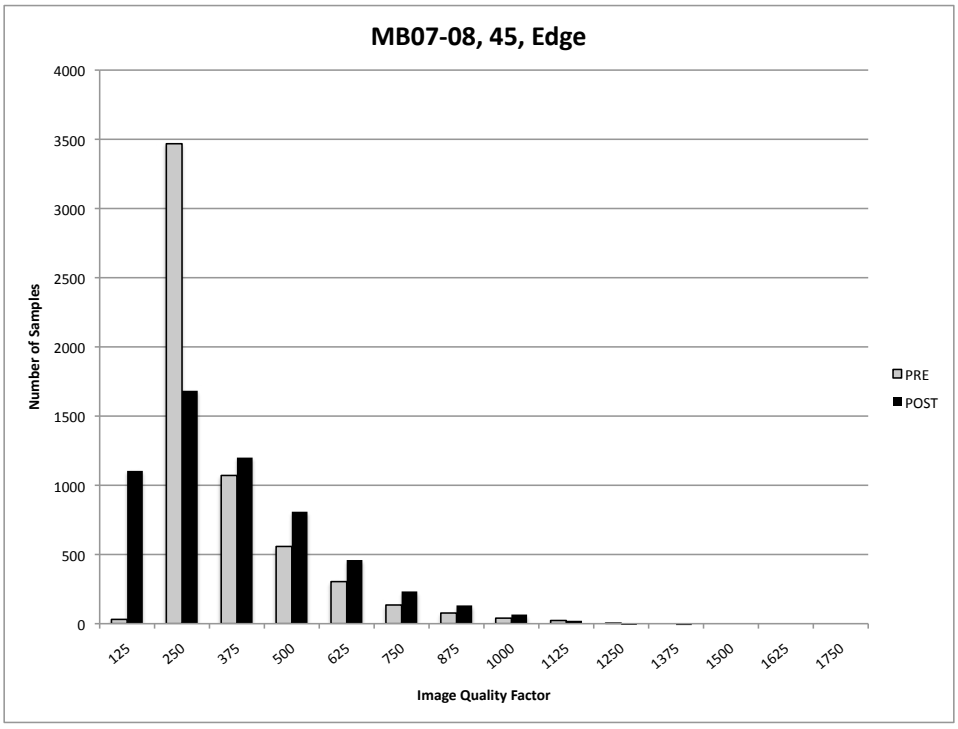

Figure A.10. Histogram of pre- and post-ion polish image quality data for French Slate sample MB07-08, 45˚ section, edge map area.

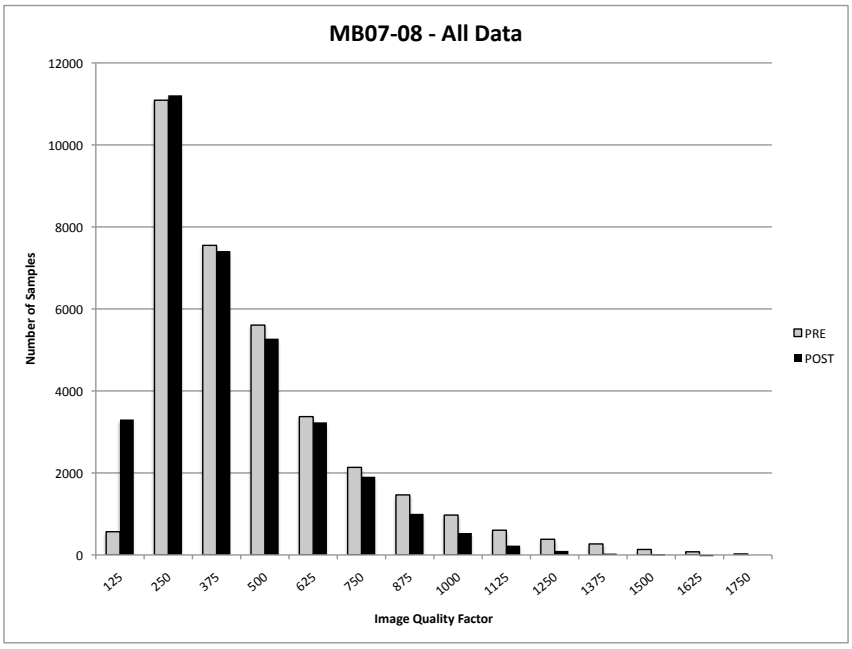

Figure A.11. Histogram of pre- and post-ion polish image quality data for all French Slate samples

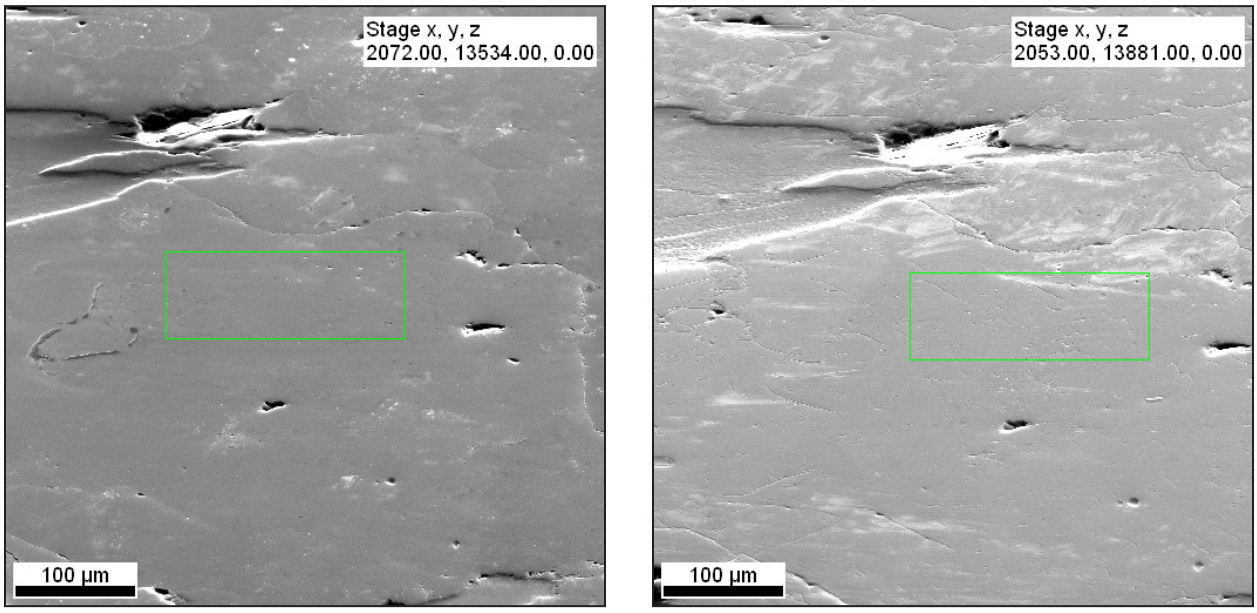

Figure A.12. Pre- (left) and post-ion polish (right) secondary electron images of Quartzite sample 090708B1, X-Y section, quartz grain 1 map area.

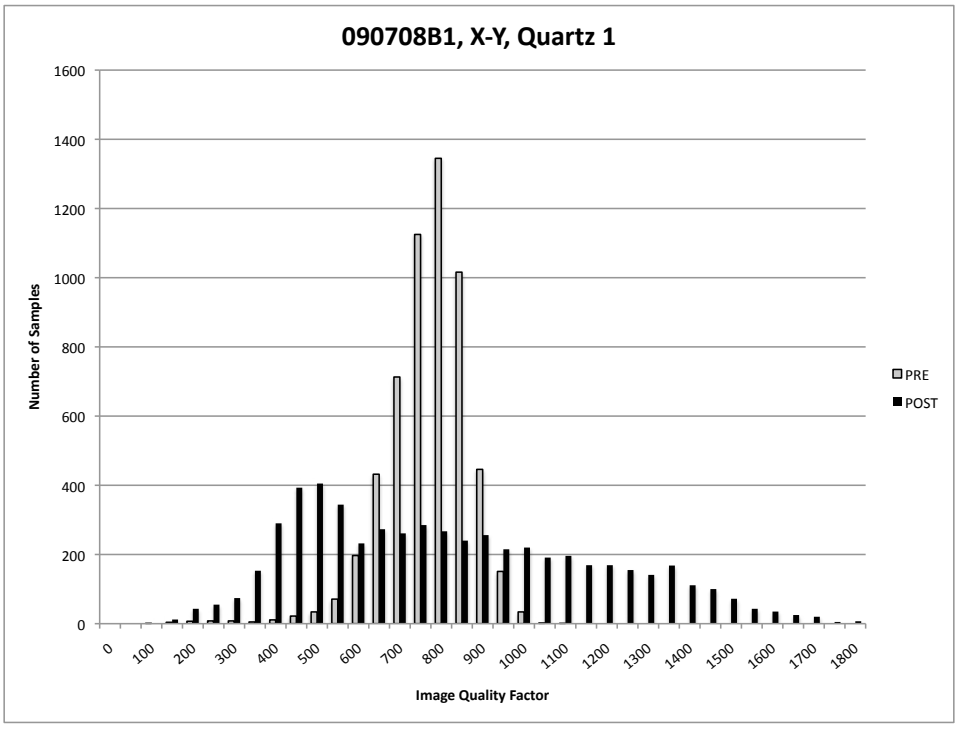

Figure A.13. Histogram of pre- and post-ion polish image quality data for Quartzite sample 090708B1, X-Y section, quartz grain 1 map area.

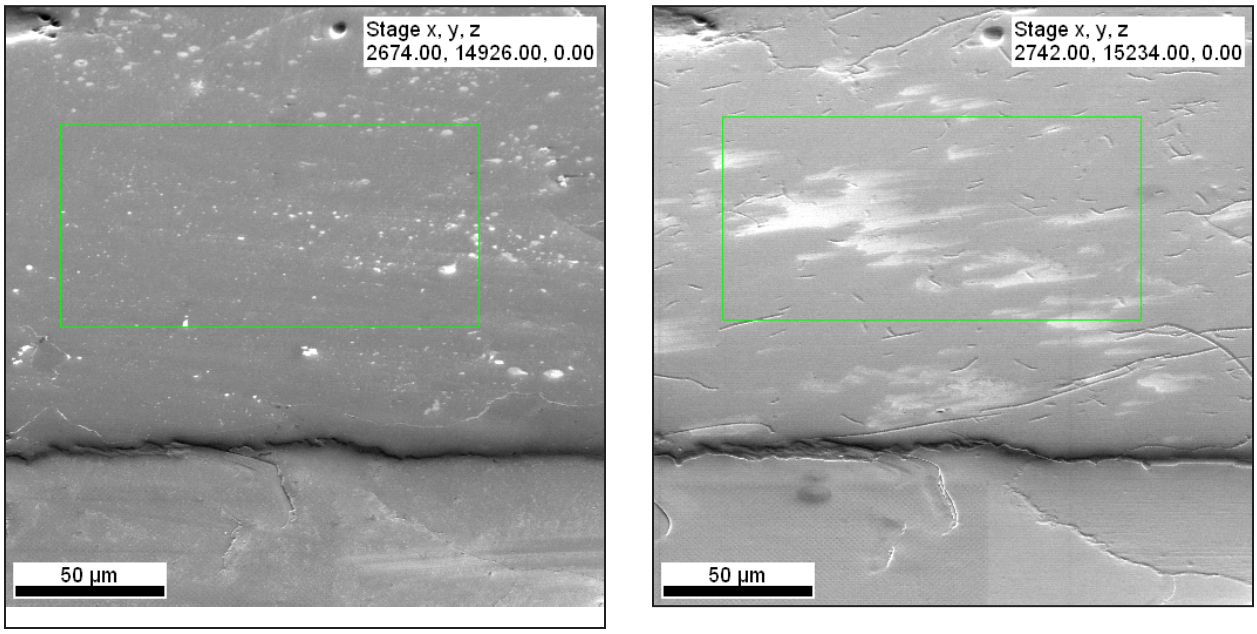

Figure A.14. Pre- (left) and post-ion polish (right) secondary electron images of Quartzite sample 090708B1, X-Y section, quartz grain 2 map area.

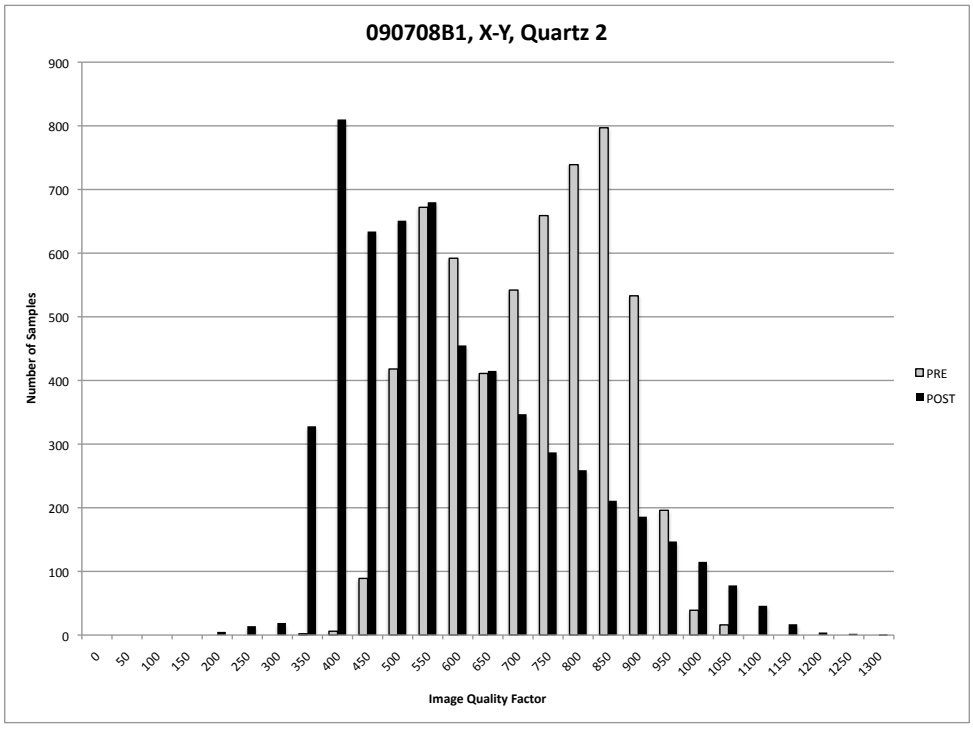

Figure A.15. Histogram of pre- and post-ion polish image quality data for Quartzite sample 090708B1, X-Y section, quartz grain 2 map area.

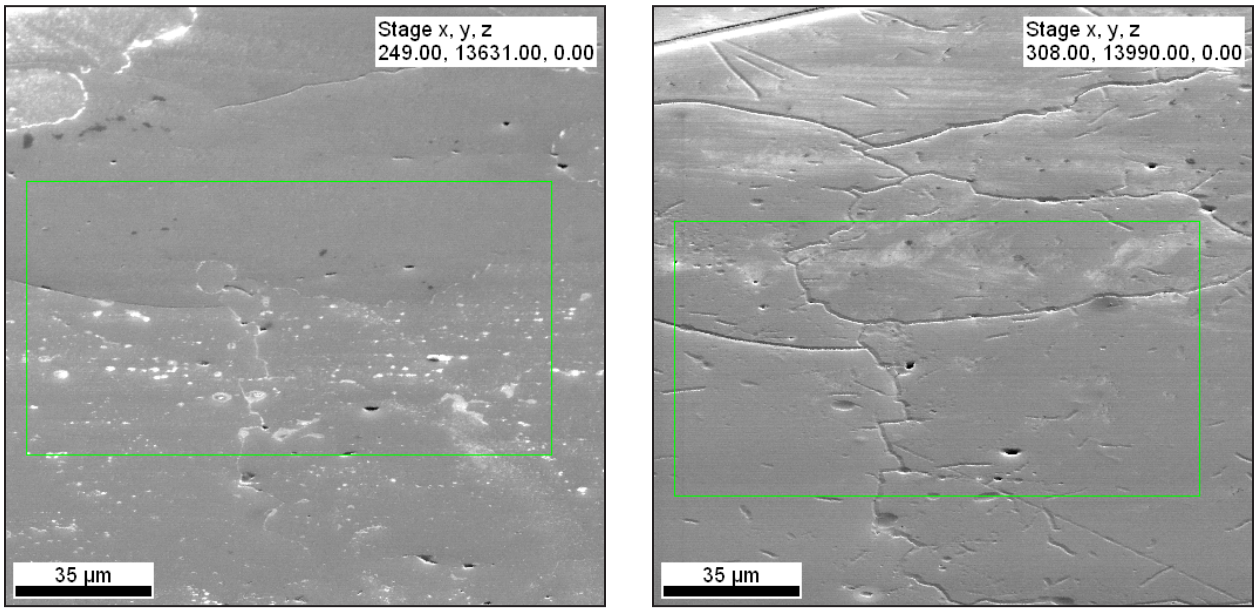

Figure A.16. Pre- (left) and post-ion polish (right) secondary electron images of Quartzite sample 090708B1, X-Y section, quartz grain 3 map area.

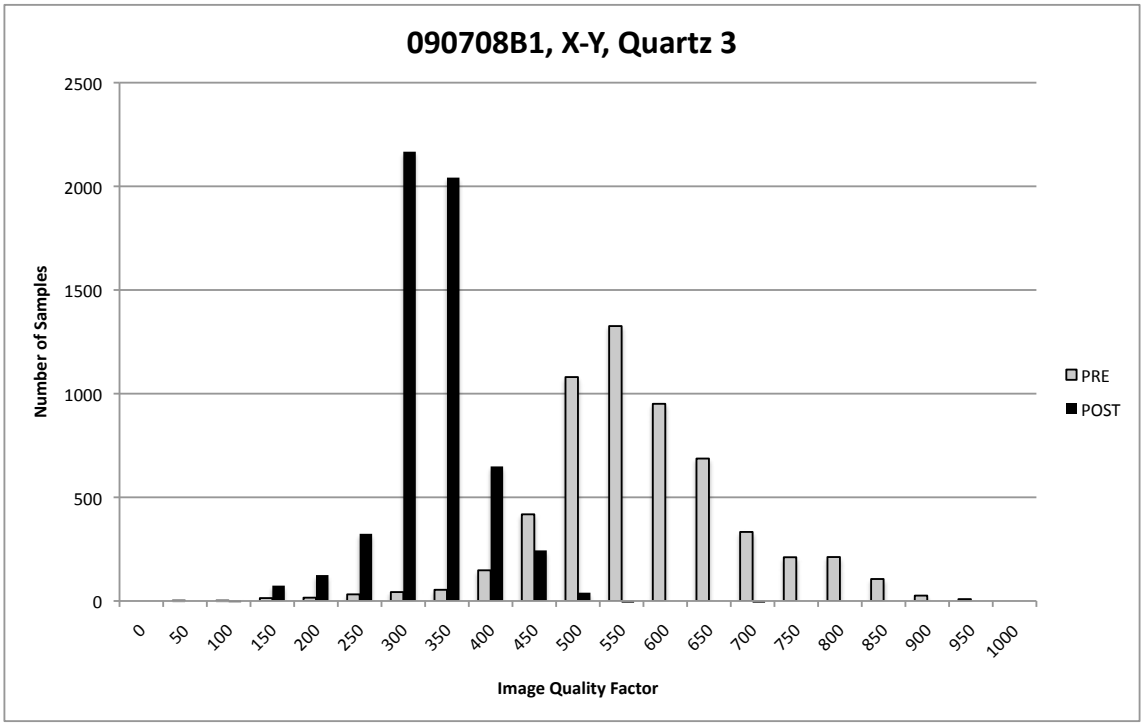

Figure A.17. Histogram of pre- and post-ion polish image quality data for Quartzite sample 090708B1, X-Y section, quartz grain 3 map area.

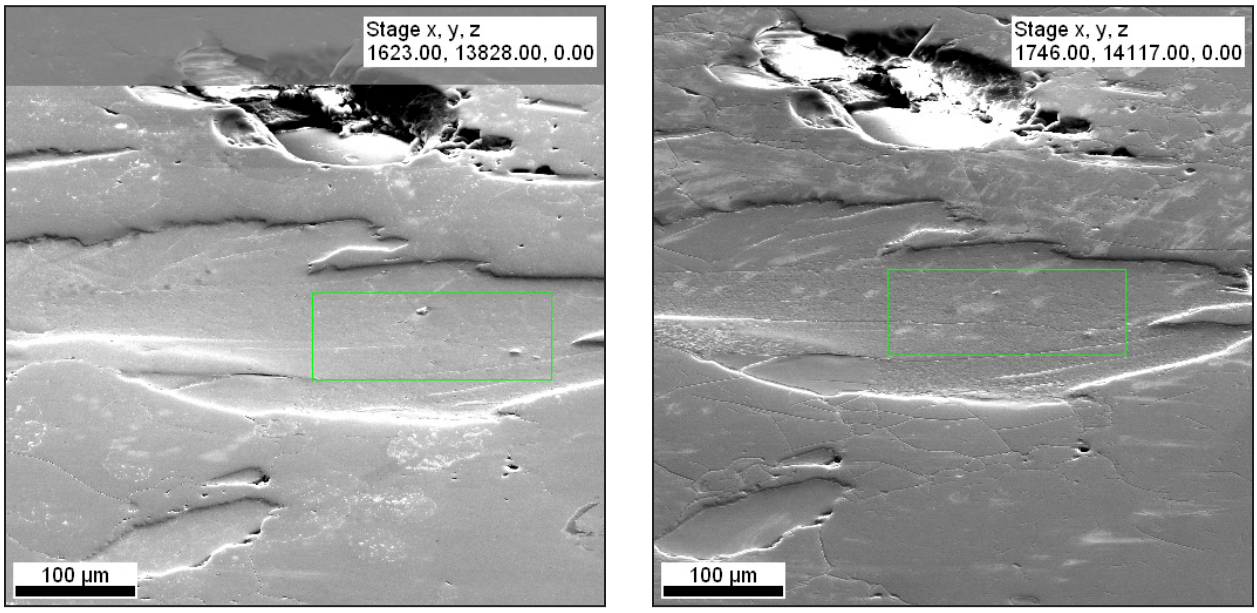

Figure A.18. Pre- (left) and post-ion polish (right) secondary electron images of Quartzite sample 090708B1, X-Y section, muscovite grain 1 map area.

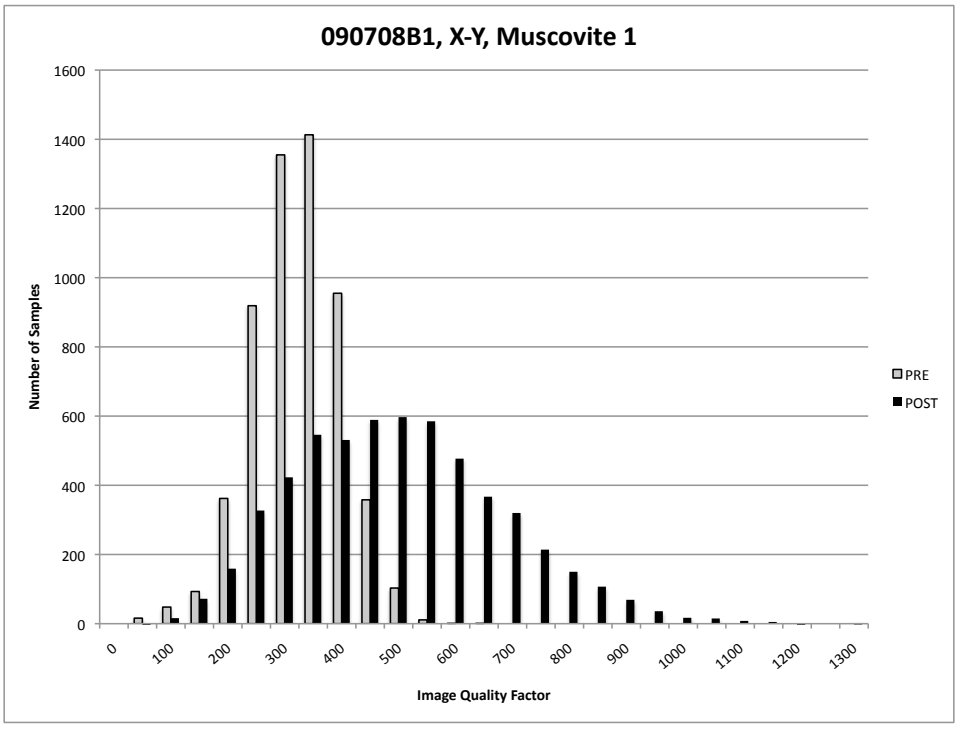

Figure A.19. Histogram of pre- and post-ion polish image quality data for Quartzite sample 090708B1, X-Y section, muscovite grain 1 map area.

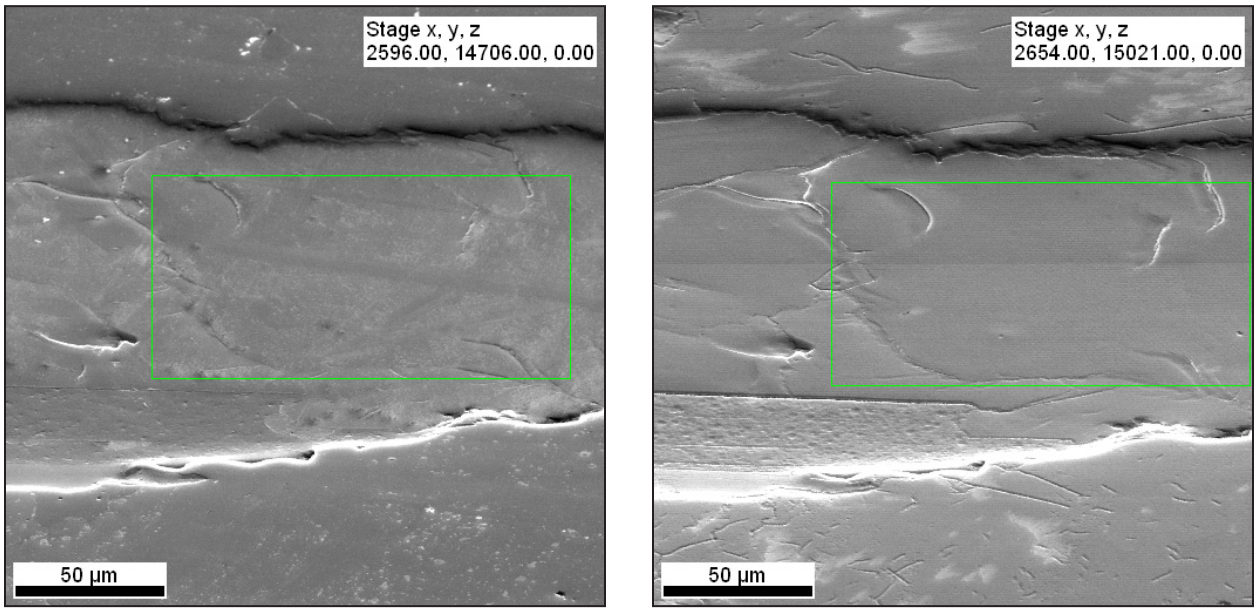

Figure A.20. Pre- (left) and post-ion polish (right) secondary electron images of Quartzite sample 090708B1, X-Y section, muscovite grain 2 map area.

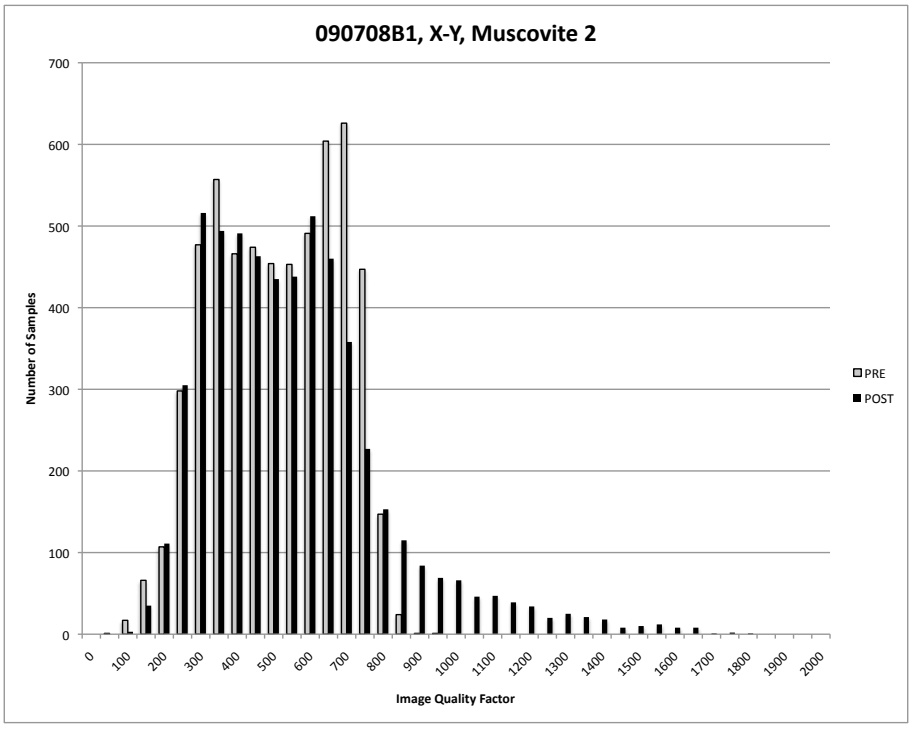

Figure A.21. Histogram of pre- and post-ion polish image quality data for Quartzite sample 090708B1, X-Y section, muscovite grain 2 map area.

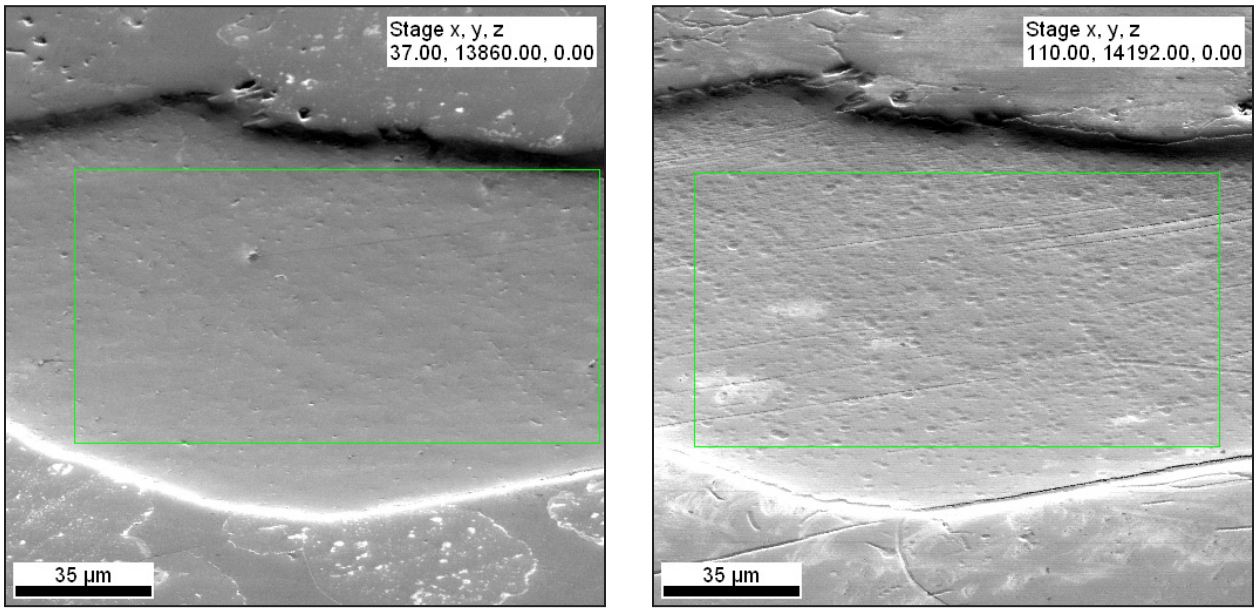

Figure A.22. Pre- (left) and post-ion polish (right) secondary electron images of Quartzite sample 090708B1, X-Y section, muscovite grain 3 map area.

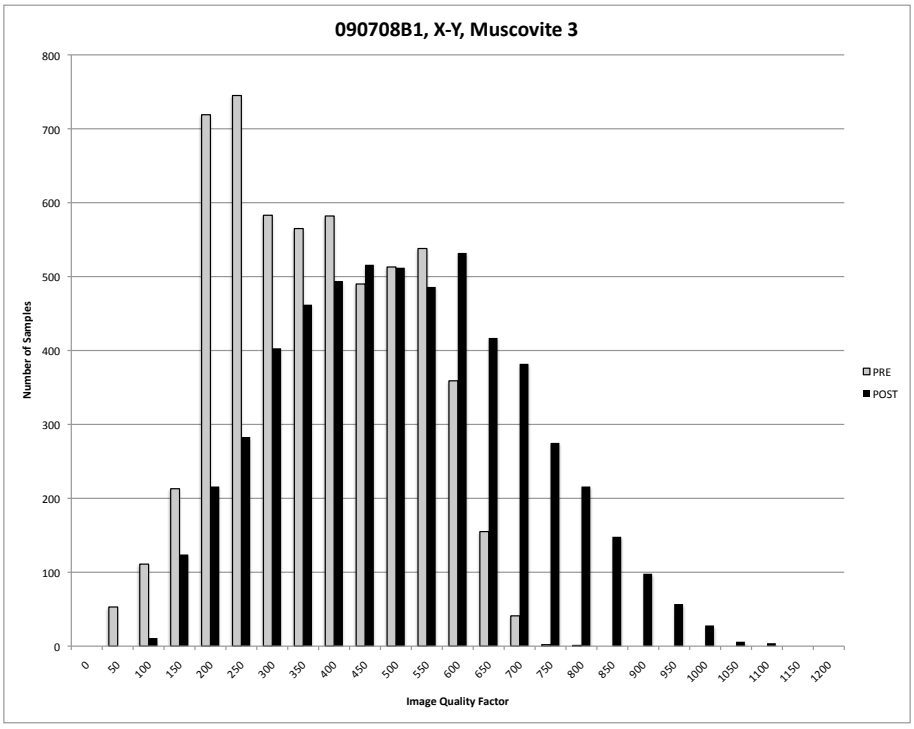

Figure A.23. Histogram of pre- and post-ion polish image quality data for Quartzite sample 090708B1, X-Y section, muscovite grain 3 map area.

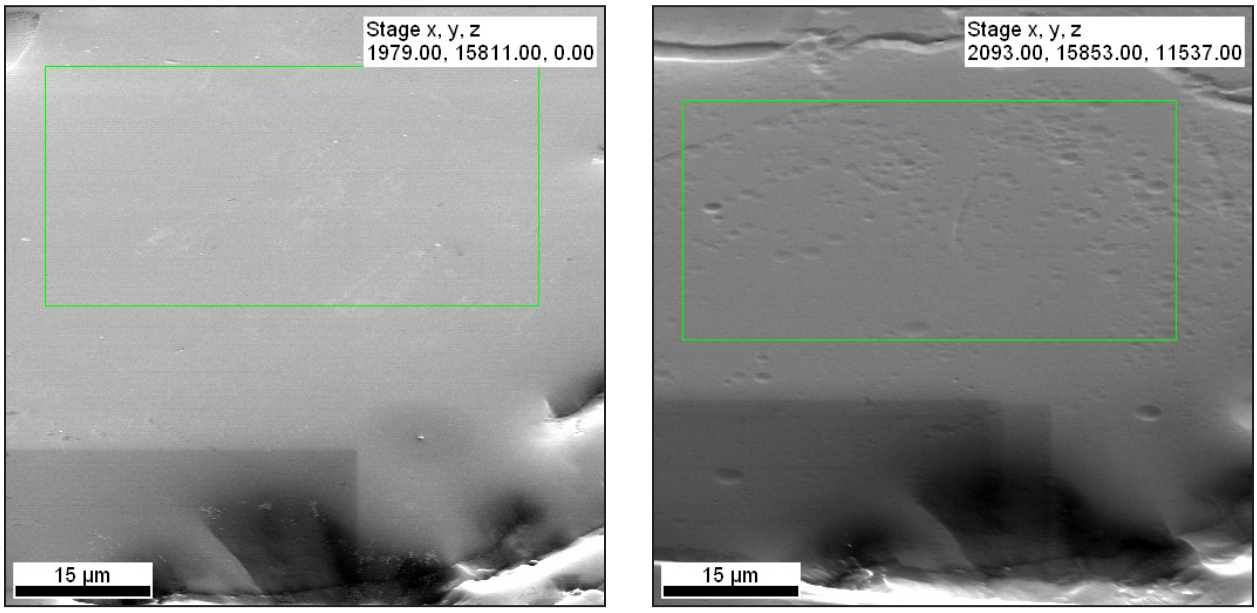

Figure A.24. Pre- (left) and post-ion polish (right) secondary electron images of Quartzite sample 090708B1, X-Z section, quartz grain 1 map area.

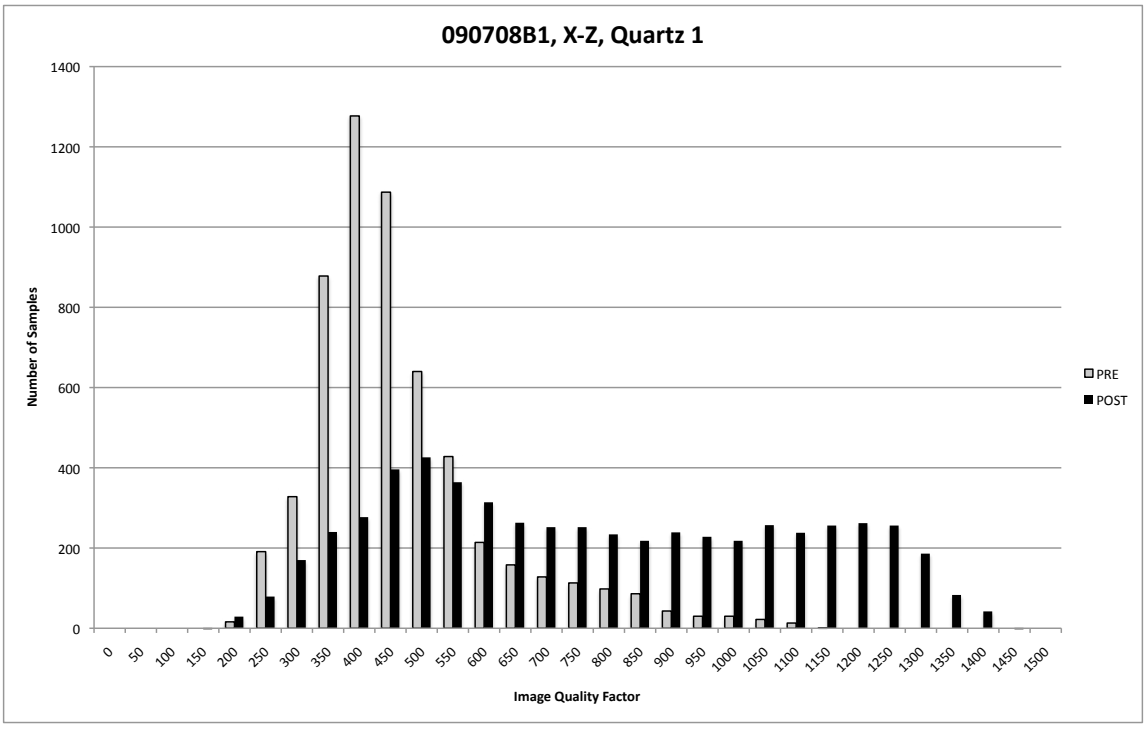

Figure A.25. Histogram of pre- and post-ion polish image quality data for Quartzite sample 090708B1, X-Z section, quartz grain 1 map area.

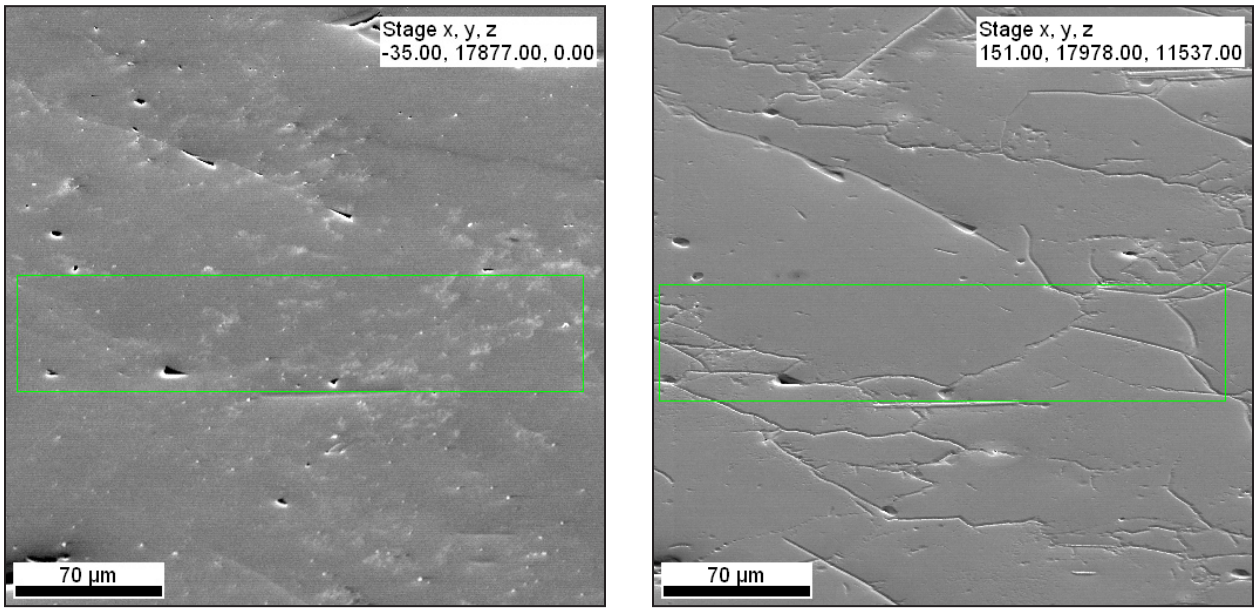

Figure A.26. Pre- (left) and post-ion polish (right) secondary electron images of Quartzite sample 090708B1, X-Z section, quartz grain 2 map area.

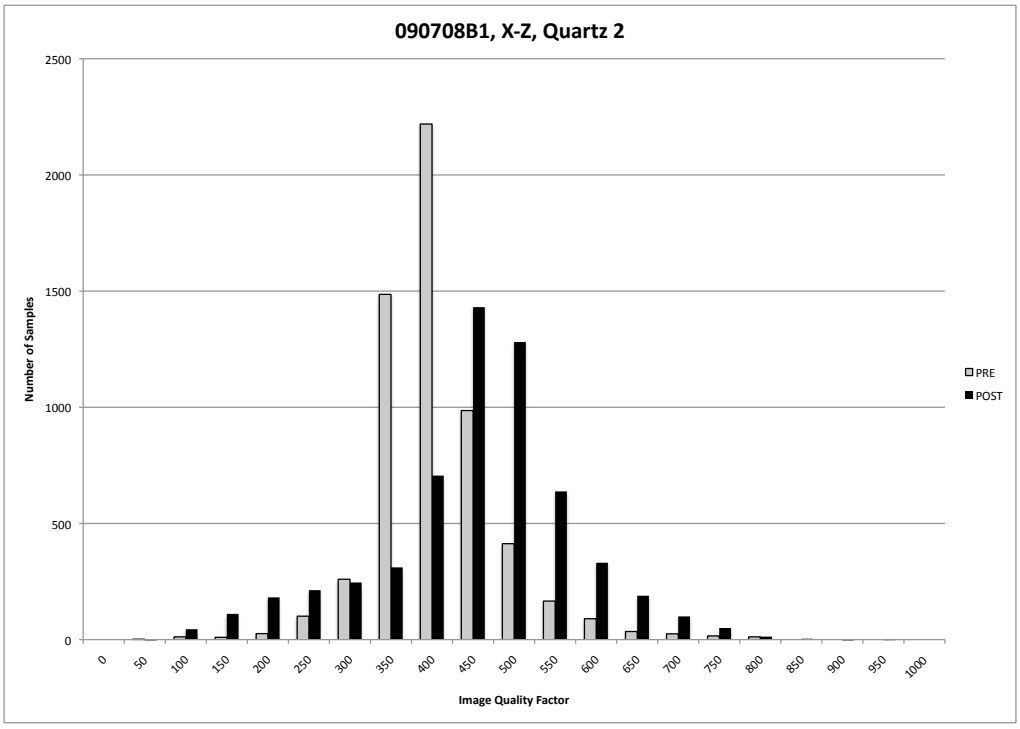

Figure A.27. Histogram of pre- and post-ion polish image quality data for Quartzite sample 090708B1, X-Z section, quartz grain 2 map area.

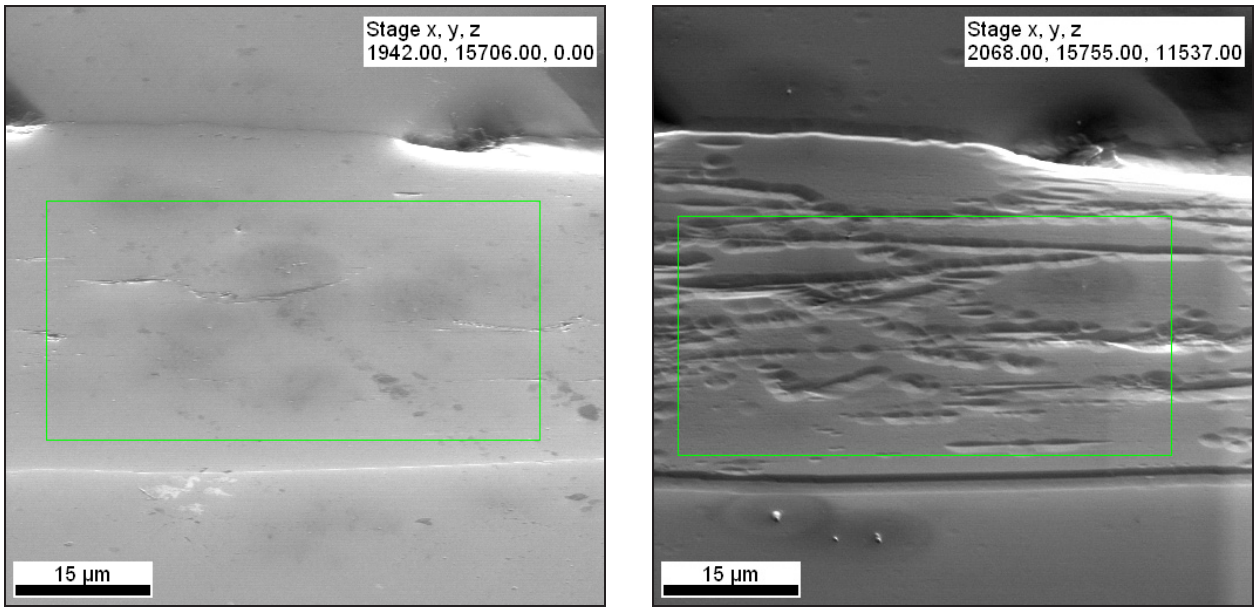

Figure A.28. Pre- (left) and post-ion polish (right) secondary electron images of Quartzite sample 090708B1, X-Z section, muscovite grain 1 map area.

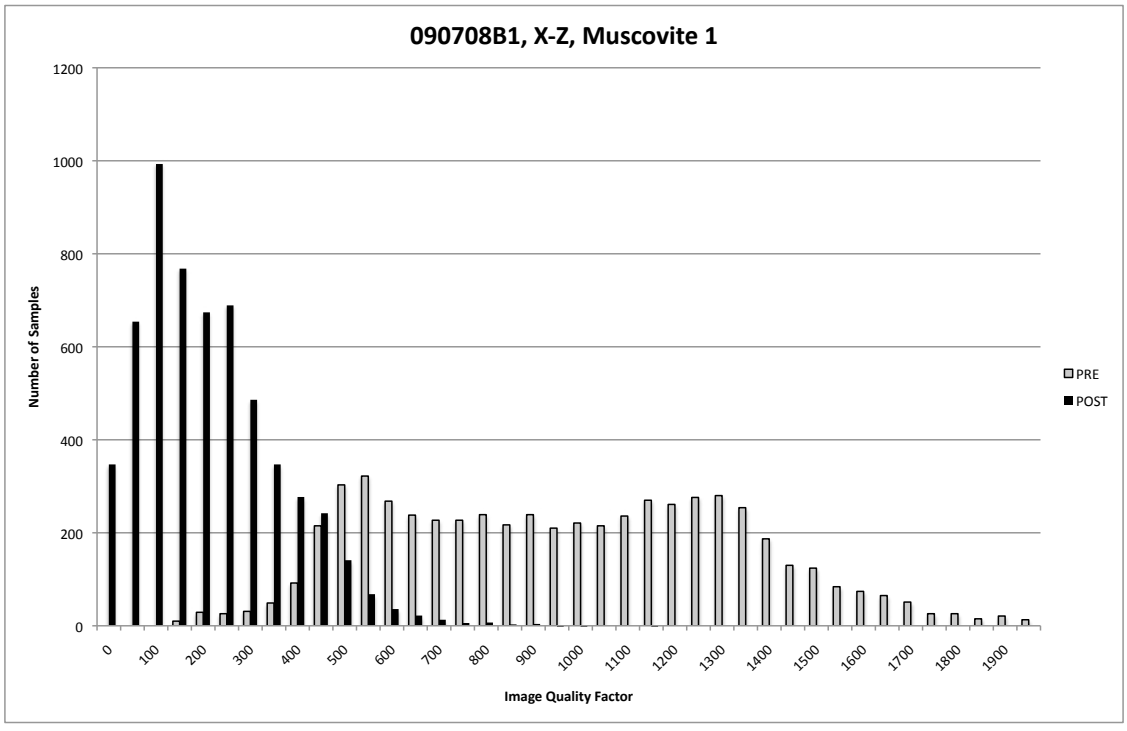

Figure A.29. Histogram of pre- and post-ion polish image quality data for Quartzite sample 090708B1, X-Z section, muscovite grain 1 map area.

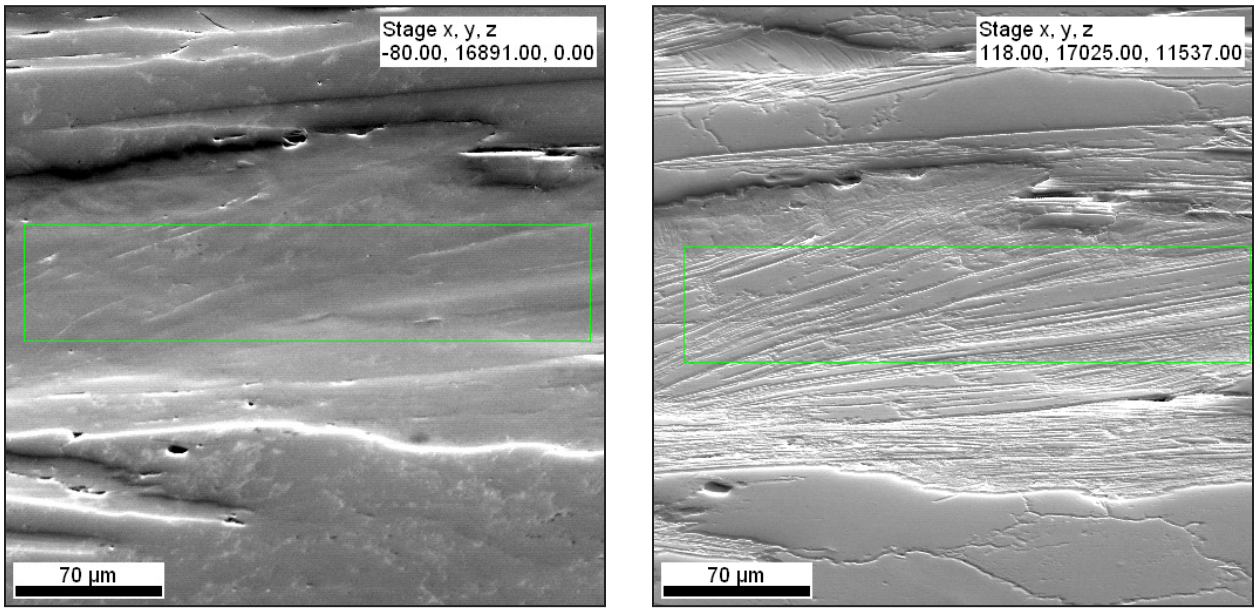

Figure A.30. Pre- (left) and post-ion polish (right) secondary electron images of Quartzite sample 090708B1, X-Z section, muscovite grain 2 map area.

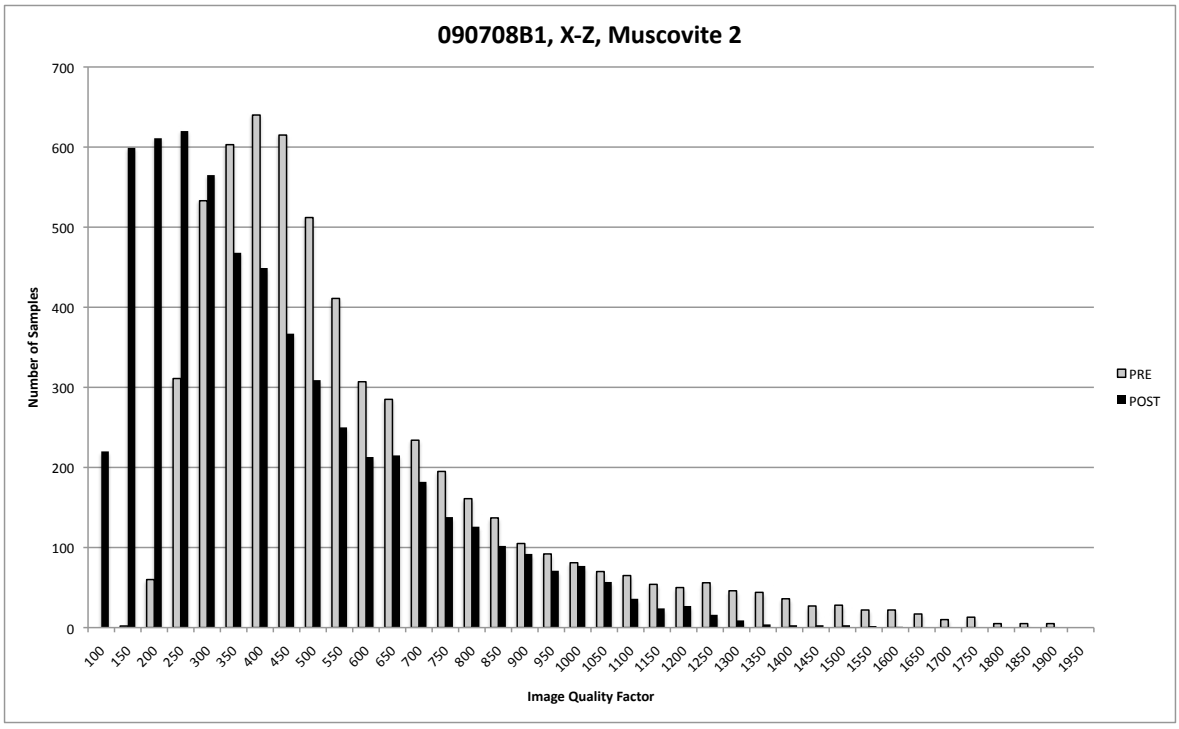

Figure A.31. Histogram of pre- and post-ion polish image quality data for Quartzite sample 090708B1, X-Z section, muscovite grain 2 map area.

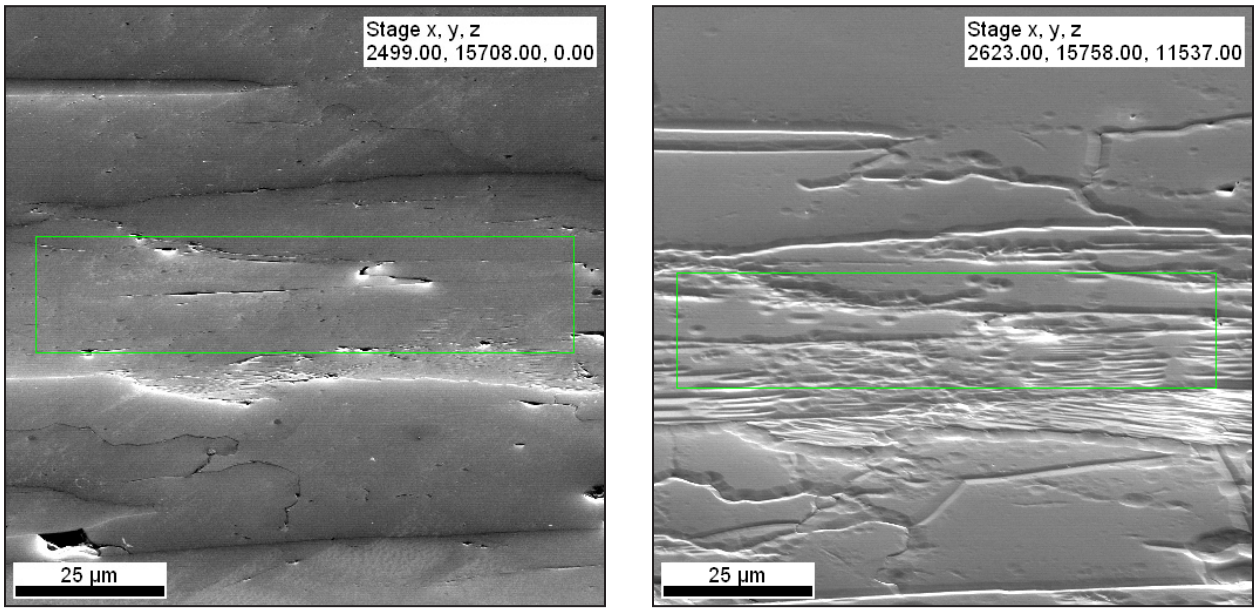

Figure A.32. Pre- (left) and post-ion polish (right) secondary electron images of Quartzite sample 090708B1, X-Z section, muscovite grain 3 map area.

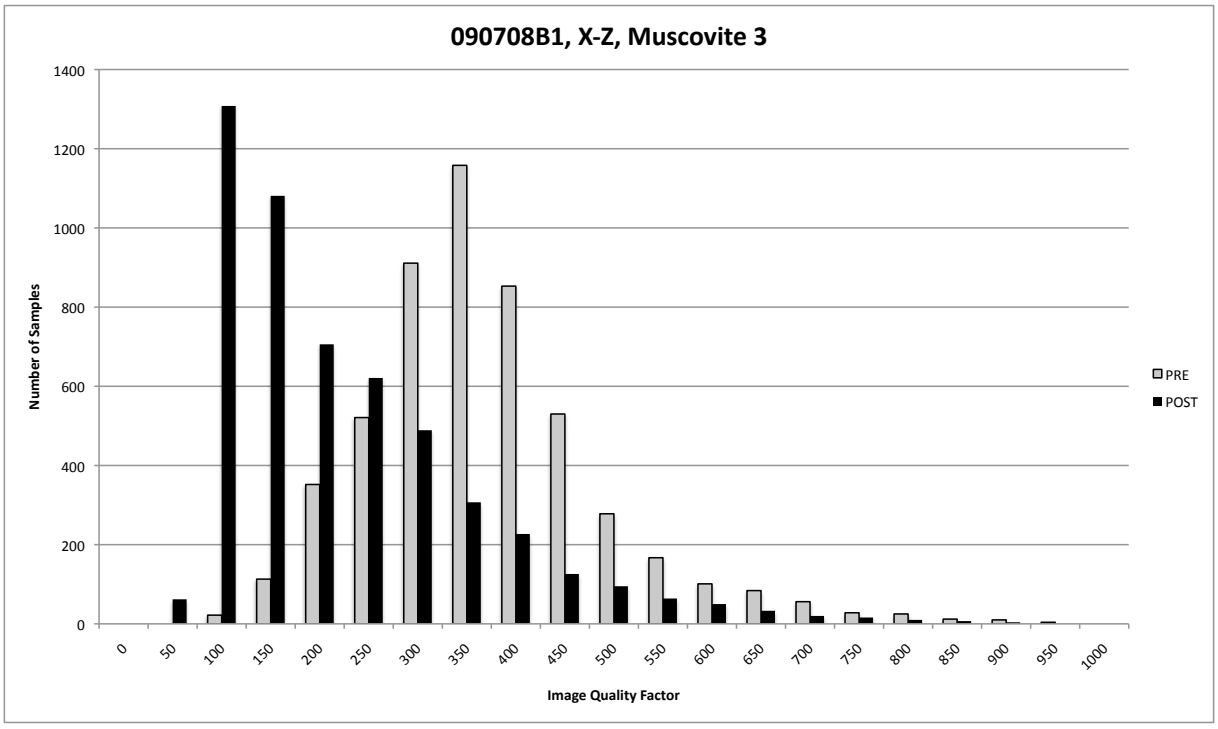

Figure A.33. Histogram of pre- and post-ion polish image quality data for Quartzite sample 090708B1, X-Z section, muscovite grain 3 map area.

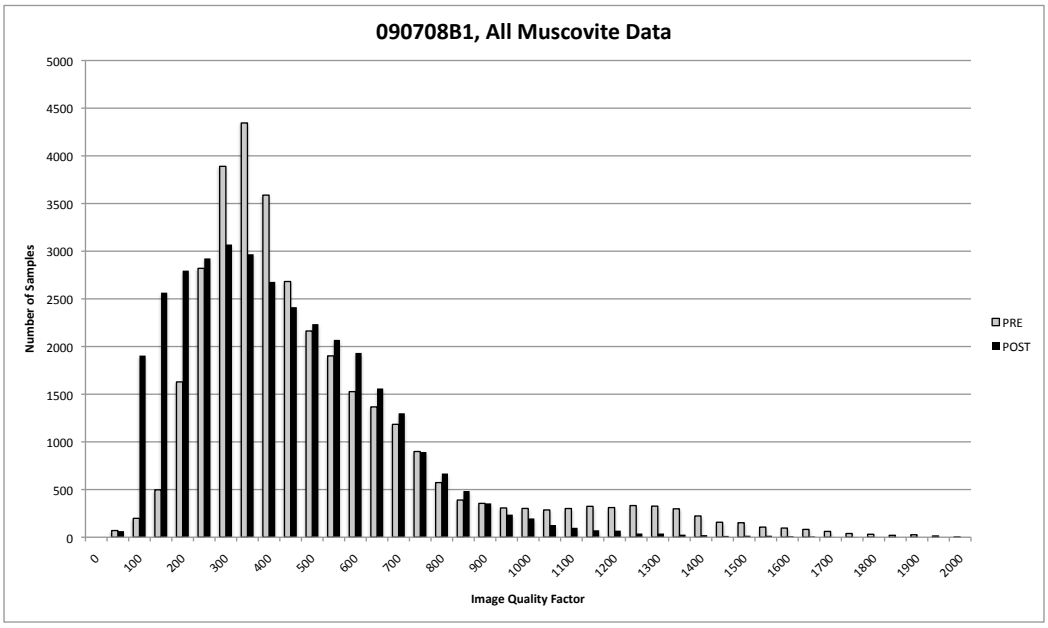

Figure A.34. Histogram of pre- and post-ion polish image quality data for quartzite sample 090708B1, all muscovite grain map area data

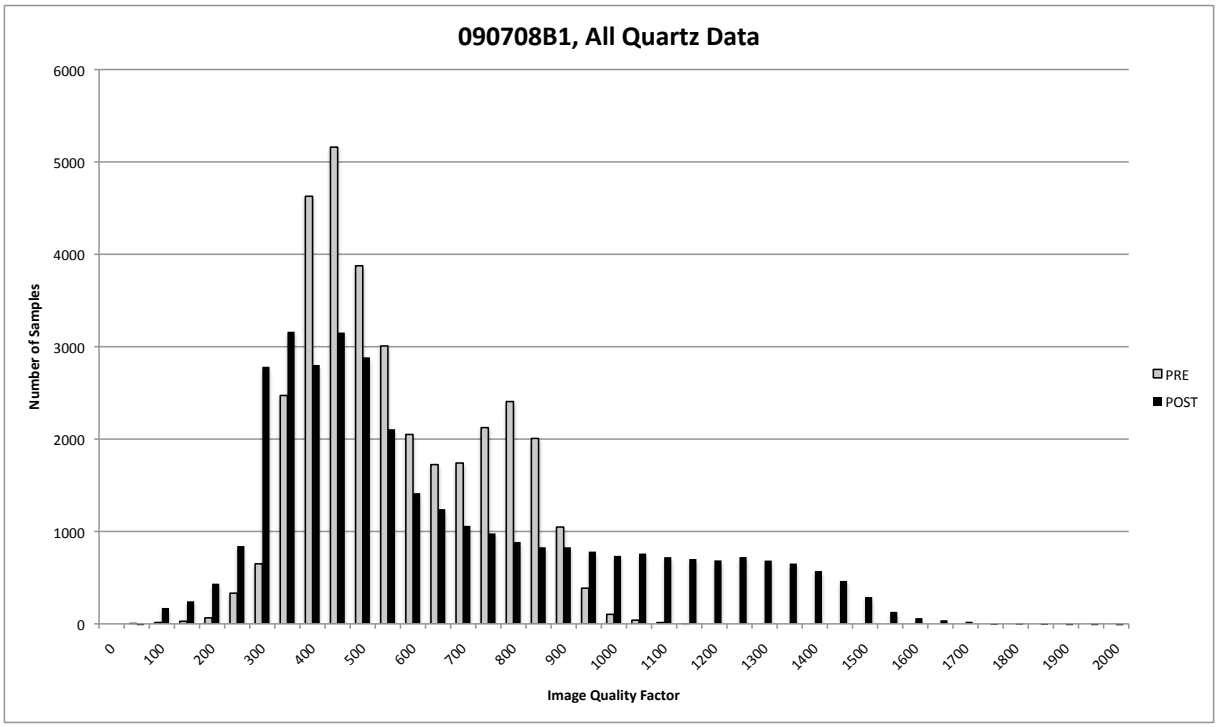

Figure A.35. Histogram of pre- and post-ion polish image quality data for quartzite sample 090708B1, all quartz grain map area data

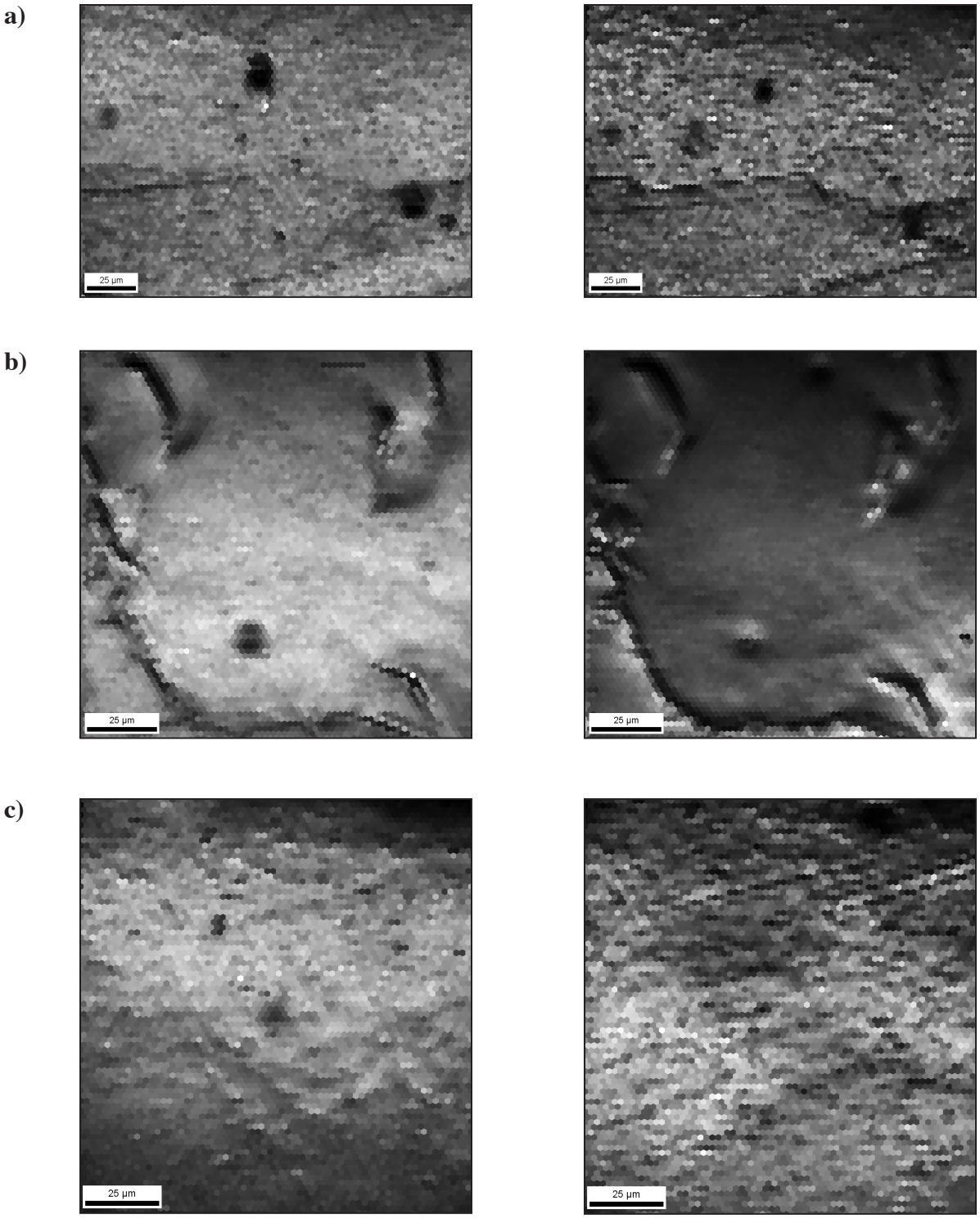

Figure A.36. Image quality maps from pre- (left column) and post-ion polishing (right column), sample 090708B1, xy section a) muscovite 1, b) muscovite 2, c) muscovite 3.

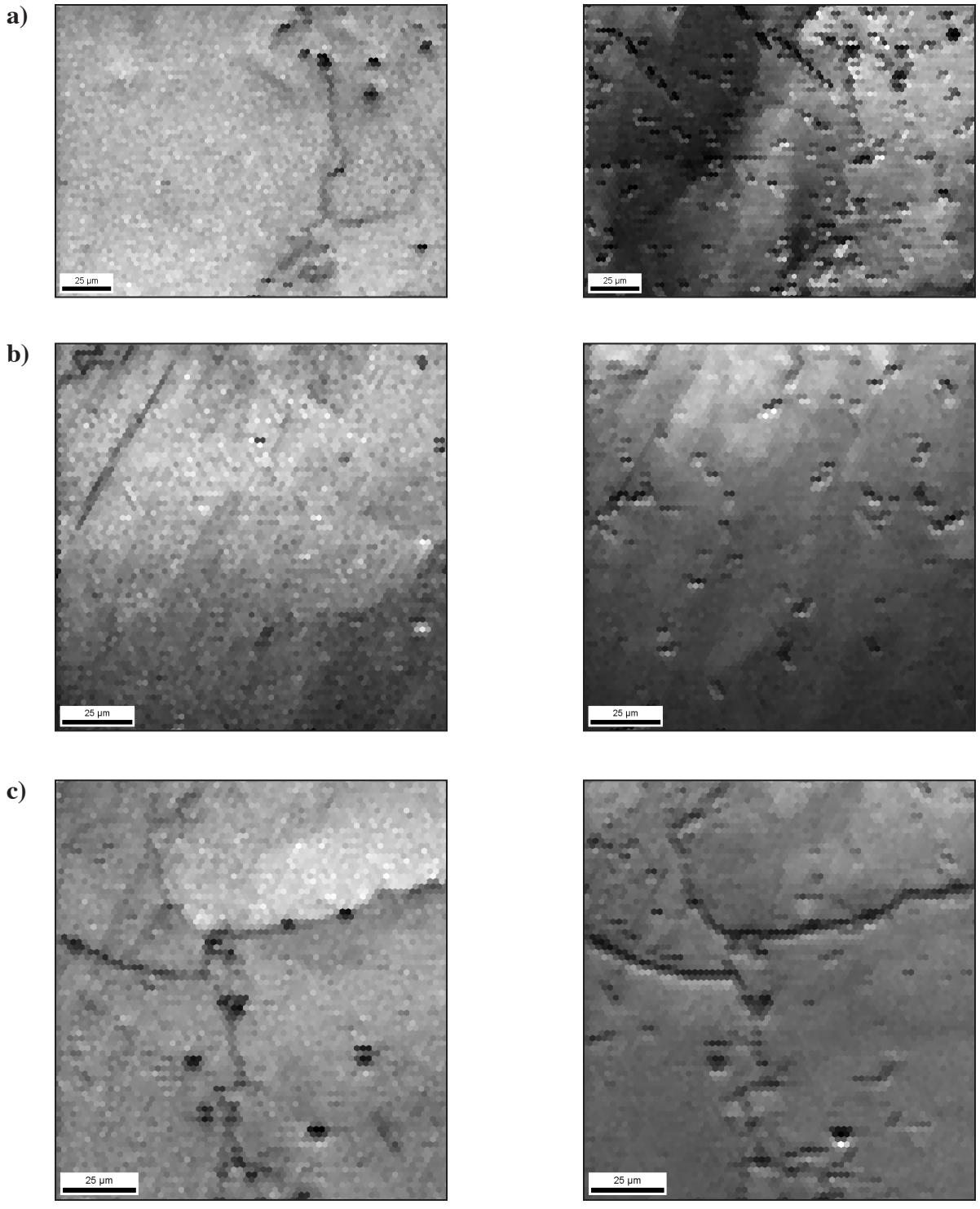

Figure A.37. Image quality maps from pre- (left column) and post-ion polishing (right column), sample 090708B1 xy section, a) quartz 1, b) quartz 2, c) quartz 3.

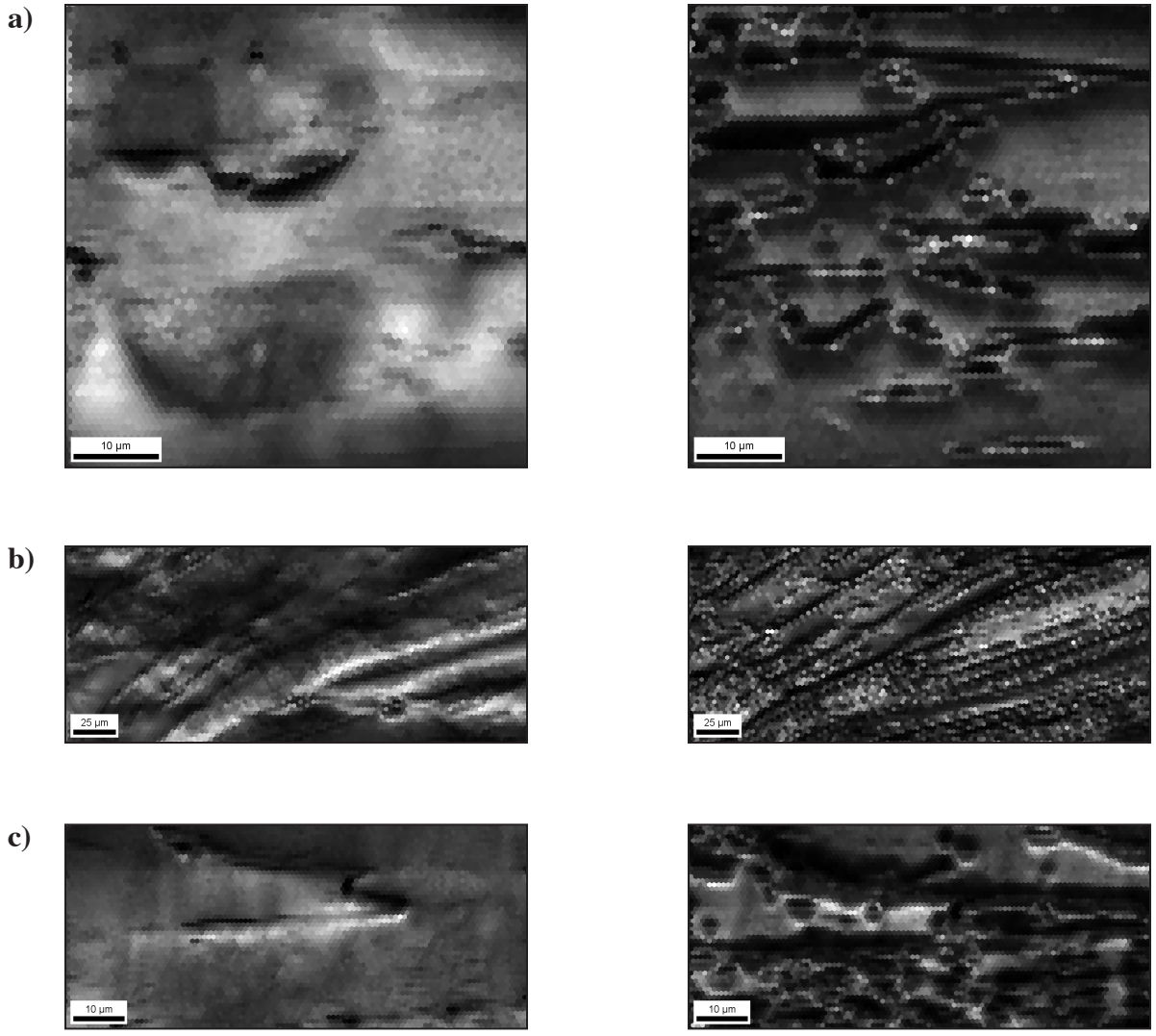

Figure A.38. Image quality maps from pre- (left column) and post-ion polishing (right column), sample 090708B1 xz section, a) muscovite 1, b) muscovite 2, c) muscovite 3.

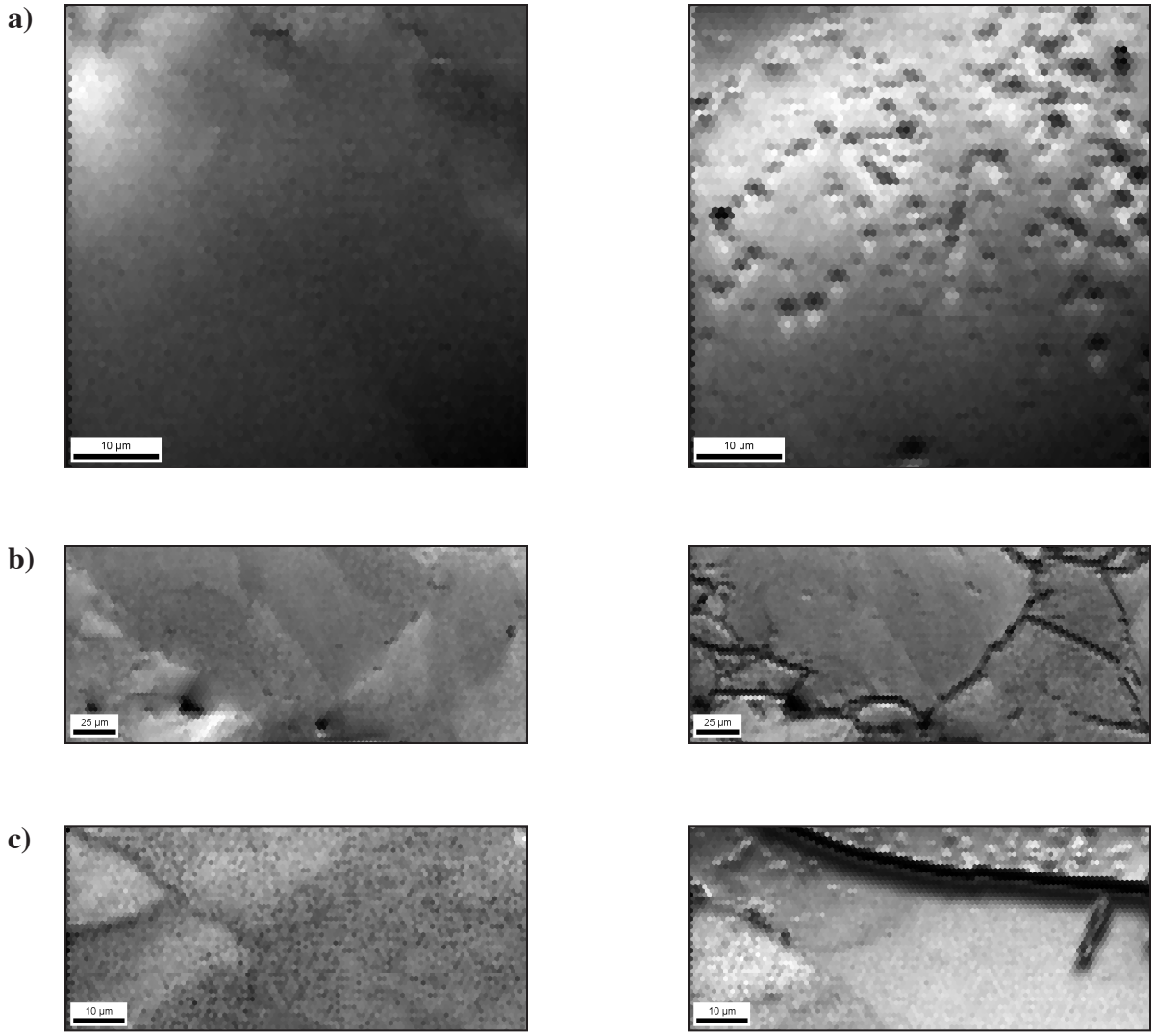

Figure A.39. Image quality maps from pre- (left column) and post-ion polishing (right column), sample 090708B1 xz section, a) quartz 1, b) quartz 2, c) quartz 3.

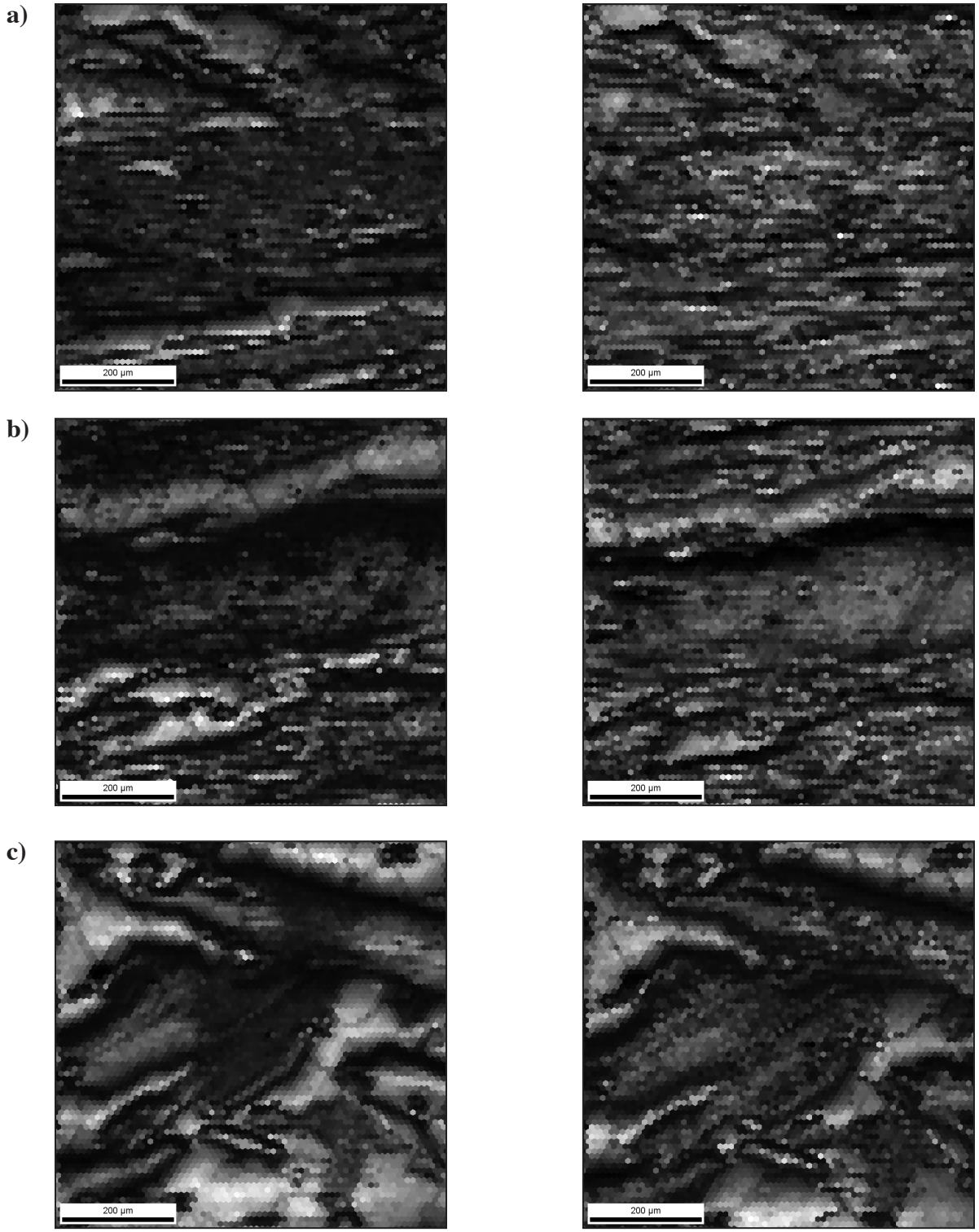

Figure A.40. Image quality maps from pre- (left column) and post-ion polishing (right column), sample MB07-08, a) oblicque section center, b) oblique section edge, c) xy section center.

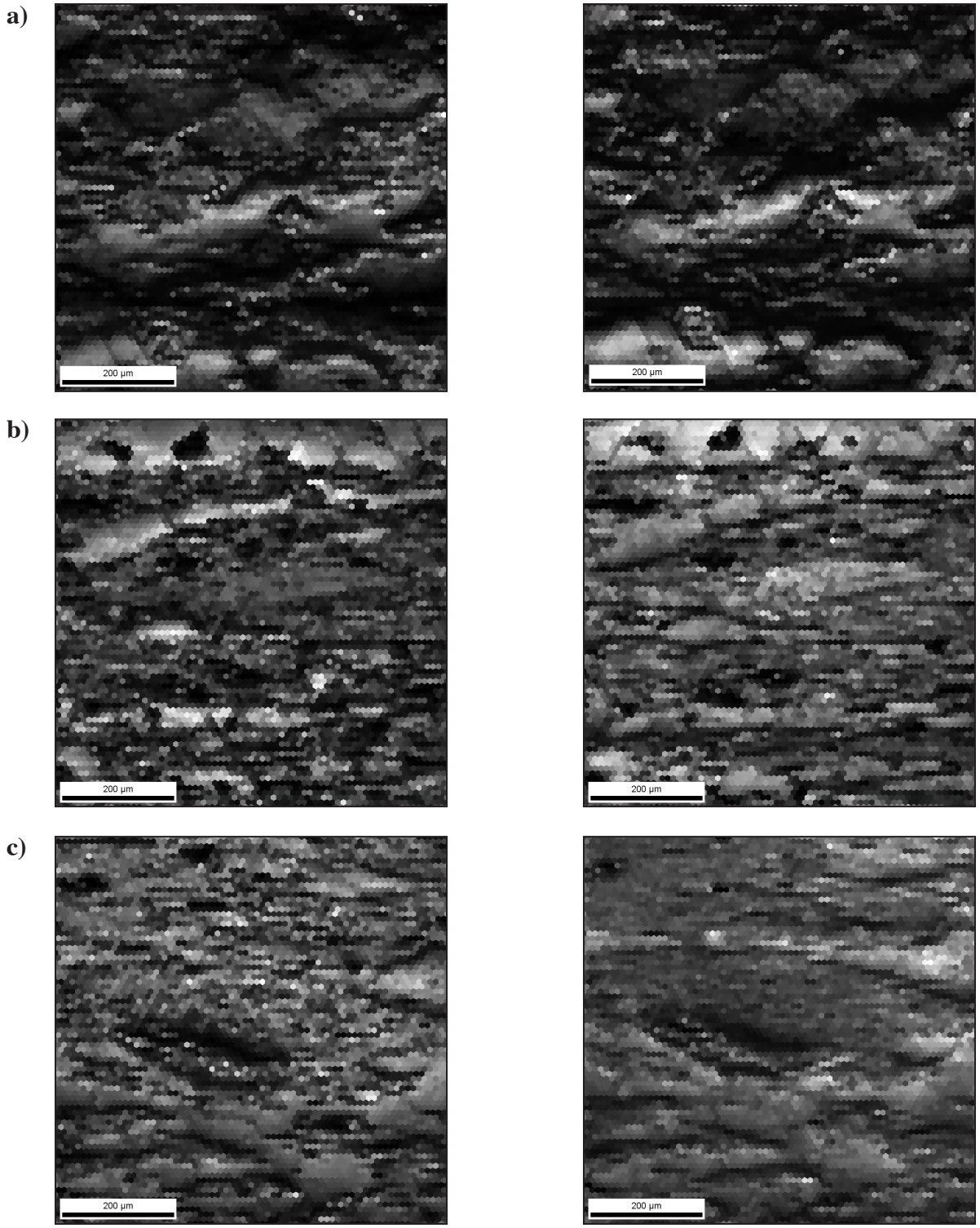

Figure A.41. Image quality maps from pre- (left column) and post-ion polishing (right column), sample MB07-08, a) xy section edge b) xz section center, c) xz section edge.

REFERENCES

Aleinikoff, J.N., Reed, J.C., and Dewitt, E., (1993). "The Mount Evans batholith in the Colorado Front Range - revision of its age and reinterpretation of its structure." Geological Society of America Bulletin: 105, 791-806.

Ball, T. T. and G. L. Farmer (1991). "Identification of 2.0 to 2.4 Ga Nd model age crustal material in the Cheyenne belt, southeastern Wyoming: Implications for Proterozoic accretionary tectonics at the southern margin of the Wyoming craton." Geology 19: 360-363.

Barna, A., (1987). "Topographic kinetics and the practice of low angle ion bean thinning." South Bay technologies Technical Library report number 146, Mat. Res. Soc. Symp. Proc. Vol. 254, p. 3-22.

Becker, T. W., Schulte-Pelkum, V., Blackman, D. K., Kellogg, J. B. and O'Connell, R. J., (2006). "Mantle flow under the western United States from shear wave splitting." Earth and Planetary Science Letters. no. 247, p. 235-251

Behn, M. D., Hirth, G., and Kelemen, P. B., (2007). "Trench-parallel anisotropy produced by foundering of arc lower crust." Science, v. 317, p. 108-111

Boness, N. L. and Zoback, M. D., (2006). "Mapping stress and structurally controlled crustal shear velocity anisotropy in California." Geology, v. 34, no 10, p. 825-828

Burlini, L., and D. M. Fountain., 1993. Seismic anisotropy of metapelites from the Ivrea-Verbano zone and Serie dei Laghi (northern Italy). Physics of the Earth and Planetary Science Letters. 247: 235-251

Chamberlain, K.R., Frost, C.D., and Frost, B.R. (2003). "Early Archean to Mesoproterozoic evolution of the Wyoming Province: Archean origins to modern lithospheric architecture." Canadian Journal of Earth Sciences, 40, 1357-1374.

Chamberlain, K. R. (1998). "Medicine Bow orogeny: Timing of deformation and model of crustal structure produced during continent-arc collision, ca. 1.78 Ga, southeastern Wyoming." Rocky Mountain Geology 33(2): 259-277.

Crampin, S., (1991) "Wave propogation through fluid-filled inclusions of various shapes: Interpretation of extensive dilatancy anisotropy." Geophysical Journal International v. 107, p. 611-623.

Duebendorfer, E.M. (1988). “Evidence for an inverted metamorphic gradient associated with a Precambrian suture, southeastern Wyoming, Journal of Metamorphic Geology, 6, 41-63.

Duebendorfer, E. M., K. R. Chamberlain, et al. (2006). “Filling the North American Proterozioc tectonic gap: 1.6-1.59-Ga deformation and orogenesis in southern Wyoming, USA.” The Journal of Geology 114: 19-42.

Duebendorfer, E. M. and R. S. Houston (1986). “Kinematic history of the Cheyenne belt, Medicine Bow Mountains, southeastern Wyoming.” Geology 14: 171-174.

Heaney, E. P., Vicenzi, E. P., Giannuzzi, L. A., and Livi, K. J. T., (2001). “Focused ion beam milling: A method of site-specific sample extraction for microanalysis of Earth and Planetary materials.” American Mineralogist, V. 86, p. 1094-1099.

Hirth, G. and J. Tullis (1992). “Dislocation creep regimes in quartz aggregates.” Journal of Structural Geology 14(2): 145-159.

Hoal, K. O., Appleby, S. K., Stammer, J. G., and Palmer, C., 2009, SEM-based quantitative mineralogical analysis of peridotite, kimberlite, and concentrate: Lithos, v. 112, no. S1, p. 41-46.

Houston, R.S., (1993). “Late Archean and Early Proterozoic geology of southeastern Wyoming” edited by A.W. Snoke, et al., pp.78-116, Geological Survey of Wyoming, Laramie.

Houston, R. S., E. M. Duebendorfer, et al. (1989). “A review of the geology and structure of the Cheyenne belt and Proterozoic rocks of southern Wyoming.” Geological Society of America Special Paper 235.

Houston, R. S., Karlstrom, K. E., (1992). “Geologic map of Precambrian metasedimentary rocks of the Medicine Bow Mountains, Albany and Carbon Counties, Wyoming.” USGS Miscellaneous Investigations Series, Map I-2280

Houston, R.S. and Parker, R.B. (1963) “Structural analysis of a folded quartzite, Medicine Bow Mountains, Wyoming.” Geological Society of America Bulletin, 74, 197-202.

Ji, S., Q. Wang and B. Xia (2002). “Handbook of Seismic Properties of Minerals, Rocks and Ores.” Polytechnic International Press, ISBN: -553-01032-X

Ji, S., Salisbury, M. and Hanmer, S., (1993) Petrofabric, P-wave anisotropy and seismic reflectivity of high-grade tectonites. Tectonophysics., 222: 195-226

Jones, D. S., Snoke, A. W., Chamberlain, K. R., and Premo, W. R., (In Press). "The geology and U-Pb geochronology of the Big Creek gneiss: Implications for Proterozoic orgenesis in the Cheyenne belt region, southeastern Wyoming and northern Colorado." Geological Society of America Bulletin.

Jones, D. S., Premo, W. R., Mahan, K., and Snoke, A. W., (2010). "Is the Cheyenne belt the Mazatzal deformation front?: Evidence for reactivation of the Cheyenne belt at ~1.65-1.63 Ga." Geological Society of America, Abstracts with Programs, v. 42, no. 3.

Karlstrom, K. E., A. J. Flurkey, et al. (1983). "Stratigraphy and depositional setting of the Proterozoic Snowy Pass Supergroup, southeastern Wyoming: Record of an early Proterozoic Atlantic-type cratonic margin." Geological Society of America Bulletin 94: 1257-1274.

Karlstrom, K. E. and M. T. Heizler (1979). "Stratigraphy of the Phantom Lake Metamorphic Suite and Deep Lake Group and a review of the Precambrian tectonic history of the Medicine Bow Mountains." Contributions to Geology 17(2): 111-133.

Karlstrom, K. E. and R. S. Houston (1984). "The Cheyenne Belt: Analysis of a Proterozoic suture in southern Wyoming." Precambrian Research 25: 415-446.

Karlstrom, K. E. and E. D. Humphreys (1998). "Persistent influence of Proterozoic accretionary boundaries in the tectonic evolution of southwestern North America: Interaction of cratonic grain and mantle modification events." Rocky Mountain Geology 33(2): 161-179.

Kern, H. and Wenk, H.R., (1990) "Fabric-related velocity anisotropy and shear wave splitting in rocks from the Santa Rosa Mylonite Zone, California. Journal of Geophysical Research, 108, B12014

Klein, C., Hurlbut, C.S., Dana, J.D., (2002). "The 22nd edition of the manual of mineral science." John Wiley & Sons, Inc., New York, 641 pp.

Kruhl, J.H. (1996). "Prism- ad basal-plane parallel subgrain boundaries in quartz: a microstructural geothermobarometer. Journal of Metamorphic Geology 14, 581-589.

Lister, G.S., (1977). "Discussion: Crossed girdle c-axis fabrics in quartzites plastically deformed by plane strain and progressive simple shear." Tectonophysics, 39, 51-54.

Lloyd, G. E., R. W. H. Butler, M. Casey, D. Mainprice (2009). "Mica, Deformation fabrics and the seismic properties of the continental crust." Earth and Planetary Science Letters 288, 320-328.

Lloyd, G. E. and J. M. Kendall (2005). "Petrofabric-derived seismic properties of a mylonitic quartz simple shear zone; implications for seismic reflection profiling." Geological Society Special Publications(240): 75-94.

Loucks, R. R., Premo, W. R., and Snyder, G. L., (1988). "Petrology, structure and age of the Mullen Creek layered mafic complex and age of arc accretion, Medicine Bow Mountains." Geological Society of America Abstracts with Programs, v. 20, no. 7, p. 73.

Mahan, K. (2006). "Retrograde mica in deep crustl granulites: implications for crustal seismic anisotropy." Geophysical Research Letters, v. 33, L24301, doi:10.1029/2006GL028130

Mainprice, D. (1990). "A Fortran program to calculate seismic anisotropy from the lattice preferred orientation of minerals." Computers & Geosciences 16: 385-393.

Mainprice, D. H. and A. Nicolas (1989). "Development of shape and lattice preferred orientations: application to the seismic anisotropy of the lower crust." Journal of Structural Geology 11(1/2): 175-189.

McCoy, A.M., Karlstrom, K.E., Shaw, C.A., and Williams, M.L. (2005). "The Proterozoic ancestry of the Colorado mineral belt: 1.4 Ga shear zone system in central Colorado." in The Rocky Mountain region: An evolving lithosphere, edited by Karlstrom, K.E., and Keller, G.R., pp. 71-90, American Geophysical Union monograph, Geophysical monograph 154

McDonough, D. and Fountain, F., (1993) "P-wave anisotropy of mylonitic and infrastructural rocks from a Cordilleran core complex." Physics of Earth and planetary Interiors. 78: 319-336

Meissner, R., Rabbel, W., and Kern, H. (2006). "Seismic lamination and anisotropy of the lower continental crust, Tectonophysics, 416, 81-99.

Mizuno, T., Yomogida, K., Ito, H. and Kuwahara, Y., (2001). "Spatial distribution of shear wave anisotropy in the crust of the southern Hyogo region by borehole observations." Geophysics Journal International. 147, p. 528-542

Morozova, E. A., Win, X., Chamberlain, K.R., Smithson, S.B., Morozov, I.B., Boyd, N.K., Johnson, R.A., Karlstrom, K.E., Tyson, A.R., and Foster, C.T. (2002). "Geometry of Proterozoic sutures in the central Rocky Mountains from seismic reflection data: Cheyenne belt and Farwell Mountain structures." Geophysical Research Letters v. 29, no. 13.

Moschetti, M. P. M. H. Ritzwoller, F. Lin and Y. Yang (2010). "Seismic evidence for widespread western-US deep-crustal deformation caused by extension." Nature 464 (8), 885-890

Mueller, M.C., (1991). "Prediction of lateral variability in fracture intensity using multicomponent shear-wave seismic as a precuror to horizontal drilling." Geophysical Journal International, v. 107, p. 409-415.

Prior, D. J., Boyle, A. P., Brenker, F. Cheadle, M. C., Day, A., Lopez, G. Peruzzo, L., Potts, G. J., Reddy, S., Spiess, R., Timms, N. E., Trimby, P., Wheeler, J., and Zetterstrom, L., (1999). "The application of electron backscatter diffraction and orientation contrast imaging in the SEM to textural problems in rocks." American Mineralogist, V. 84, p. 1741-1759.

Premo, W. R. and C. M. Fanning (2000). "SHRIMP U-Pb zircon ages for Big Creek gneiss, Wyoming and Boulder Creek batholith, Colorado: Implications for timing of Paleoproterozoic accretion of the northern Colorado province." Rocky Mountain Geology 35(1): 31-50.

Tatham, D. J., G. E. Lloyd, R. W. H. Butler, M. Casey (2007). "Amphibole and lower crustal seismic properties." Earth and Planetary Science Letters 267, 118-128

Passchier, C.A. and R.A.J. Trouw (1996). "Micro-tectonics" Springer, ISBN: 3-540-58713-6

Premo, W. R. and W. R. Van Schmus (1989). "Zircon geochronology of Precambrian rocks in southeastern Wyoming and northern Colorado." Geological Society of America Special Paper 235.

Prior et al., (1999) "The application of electron backscatter diffraction and orientation contrast imaging in the SEM to textural problems in rocks." American Mineralogist. V. 84: 1741-1759

Rey, P., Fountain, D., and Clement, W., (1994) "P wave velocity across a noncoaxial ductile shear zone and its associated strain gradient." Journal of Geophysical Research. V. 99, no B3: 4533-4548

Sayers, C.M., (1994). "The elastic anisotropy of shales." Journal of Geophysical Research, v. 99, p. 767-774.

Schmid, S. M., and Casey, M., (1986). "Complete fabric analysis of some commonly observed quartz c-axis patterns." American Geophysical Union, Geophysical Monograph 36, 263-286.

Shaw. C.A., Karlstrom, K.E., McCoy, A., Williams, M.L., Jercinovic, M.J., Dueker, K., (2002). "Proterozoic Shear Zones in the Colorado Rocky Mountains: From Continental Assembly to Intracontinental Reactivation." Field Guides, v. 3, p. 102-117.

Strickland, D., (2004). “Structural and geochronologic evidence for the ca. 1.6 Ga reactivation of the Cheyenne belt, southeastern Wyoming.” [M.S. thesis]: Laramie, University of Wyoming, 62 p.

Schulte-Pelkum, Monslave, G., Sheehan, A., Pandey, M. R., Sapkota, S., and Bilham, R., (2005), “Imaging the Indian subcontinent beneath the Himalaya.” Nature, v. 435, p. 1222-1225

Tweto, O., and Sims, P.K., (1963). “Precambrian ancestry of the Colorado mineral belt.” Geological Society of America Bulletin 74: 991-1014.

Tyson, A. R., E. A. Morozova, et al. (2002). “Proterozoic Farwell Mountain-Lester Mountain suture zone, northern Colorado: Subduction flip and progressive assembly of arcs.” Geology 30(10): 943-946.

Walck, S. D., Porter, J. R., Yang, H-W., and Dheda, S. S., (2009). “Low energy, low angle, large area ion polishing for improved EBSD indexing.” Microscopy Today, May 2009.

Wenk, H-R., Ed. (1976). “Electron Microscopy in Mineralogy.” Springer-Verlag, ISBN 30540-07371-X.

Wessel, Z. and Ridley, J. (2009). “Structural analysis of the Idaho Springs-Ralston shear zone; a new look at an ancient structure.” Geological Society of America Abstracts with programs, v. 41, no. 7.

Whitmeyer, S. J. and K. E. Karlstrom (2007). “Tectonic model for the Proterozoic growth of North America.” Geosphere 3(4): 220-259.

Zandt, G, H. Gilbert, T. J. Owens, M. Ducea, J. Saleeby and C. H. Jones (2004). “Active foundering of a continental arc root beneath the southern Sierra Nevada in California.” Nature 431, 41-46.